UC San Diego
UC San Diego Electronic Theses and Dissertations

Title
Microstructural Design for Stress Wave Energy Management /

Permalink
https://escholarship.org/uc/item/2ft9v4gn

Author
Tehranian, Aref

Publication Date
2013

Peer reviewed|Thesis/dissertation

eScholarship.org Powered by the California Digital Library
University of California

UNIVERSITY OF CALIFORNIA, SAN DIEGO

Microstructural Design for Stress Wave Energy Management

A Dissertation submitted in partial satisfaction of the requirements for the degree of

Doctor of Philosophy

in

Engineering Sciences (Applied Mechanics)

by

Aref Tehranian

Committee in charge:

Professor Sia Nemat-Nasser, Chair
Professor Francesco Lanza Di Scalea
Professor Hyonny Kim
Professor Hidenori Murakami
Professor Daniel Tartakovsky

2013

Copyright ©

Aref Tehranian, 2013

All rights reserved.

The Dissertation of Aref Tehranian is approved, and it is acceptable in quality and form for publication on microfilm and electronically:

Chair

University of California, San Diego

2013

Dedication

To my family: Ashraf, Massoud, Amir, and Armin

Table of Contents

List of Figures

List of Tables

Acknowledgements

I would like to express my appreciation to Professor Sia Nemat-Nasser for his support and inspiration. Without his astute advice and invaluable guidance this work would not have been possible. At the Center of Excellence for Advanced Materials (CEAM), I could not have achieved much if it was not for the efforts and advices of Dr. Alireza V. Amirkhizi.

Chapter 2 is a reprint of the material as it appears in Wave Motion 2010, 519-536, Amirkhizi A. V., Tehranian, A. and Nemat-Nasser, S., Elsevier, 2006. The authors would like to acknowledge the contributions of Mr. Jeffrey Irion for his great help in fabricating the samples, and Mr. Jon Isaacs for helping with the experimental setup of ultrasonic measurements. This work has been supported by ONR grant N00014-09-1-0547 and DARPA grant AFOSR FA9550-09-1-0709 to the University of California, San Diego.

Chapter 3 is prepared for publication by A. Tehranian, A. Amirkhizi, and S.Nemat-Nasser. This work has been supported by an ONR grant N00014-09-1-0547 to the University of California, San Diego. The dissertation author was the primary investigator of this paper.

Vita

2007	Bachelor of Science in Civil Engineering, Sharif University of Technology, Tehran, IRAN
2009	Master of Science in Engineering Sciences (Applied Mechanics), University of California, San Diego
2013	Doctor of Philosophy in Engineering Sciences (Applied Mechanics), University of California, San Diego

Publications

Archival journals

Amirkhizi, A.V., Tehranian A. and Nemat-Nasser, S., 2010. Stress-wave energy management through material anisotropy, Wave Motion 47, 519-536.

REVIEWED PROCEEDINGS

Tehranian, A., Amirkhizi, A.V., Irion, J., Isaacs, J. and Nemat-Nasser, S., 2009. Controlling acoustic-wave propagation through material anisotropy, *Proceedings of SPIE* 7295, 72950V1-4.

Tehranian, A., Amirkhizi, A.V. and Nemat-Nasser, S., 2010. Use of anisotropy to guide acoustic waves along desired trajectories, *Proceedings of SPIE* 7650, 76500B14.

Other proceedings

Tehranian, A., Amirkhizi, A.V. and Nemat-Nasser, S., 2009. Acoustic wave-energy management in composite materials, *Proceedings of the SEM Annual Conference*.

Tehranian, A., Amirkhizi, A.V. and Nemat-Nasser, S., 2010. Controlling wave propagation in solids using spatially variable elastic anisotropy, *Proceedings of the SEM Annual Conference*.

Abstract of the Dissertation

Microstructural Design for Stress Wave Energy Management

by

Aref Tehranian

Doctor of Philosophy in Engineering Sciences (Applied Mechanics)

University of California, San Diego, 2013

Professor Sia Nemat-Nasser, Chair

Stress-wave propagation in solids can be controlled through imposing a gradual change of anisotropy in the material elasticity tensor. In this study, a transversely isotropic material is incorporated with a smoothly varying axis of anisotropy. It is shown that if this axis initially coincides with the stress wave vector, then the energy of the plane waves would closely follow this gradually changing material direction. A fiber-reinforced composite is used to induce the required anisotropy, and to experimentally demonstrate the management of stress-wave energy in a desired trajectory.

The interface between two strongly anisotropic materials has a great influence on the stress wave scattering and can play a potential role in managing stress-waves in

anisotropic and heterogeneous composites. Wave reflection and transmission at the interface of two elastic media has been thoroughly studied in the literature. In this study, we apply the theory of wave propagation to the interface of transversely isotropic materials, where the group velocity and wave-energy flow are usually close to the preferred direction of maximum stiffness. It is established that the anisotropy orientation of two interfacing materials can be exploited to control and manage stress wave energy by design; for example, the energy of an incident pressure wave can be guided to a desirable direction; the scattered longitudinal wave can be evanescent (non-propagating); and finally the energy content of stress-waves can be transferred from pressure into shear wave energy, which is prone to dissipation.

Multilayered structures consisting of strongly anisotropic layers can be exploited to efficiently manage the stress wave propagation in solids by providing multiple interfaces that play key roles in transmission and reflection of pressure and shear waves. We have developed a computational platform to efficiently evaluate the transmitted and reflected stress-waves in pressure and shear modes based on the anisotropy orientation of layers and the incident wave vector direction. We demonstrate that a multilayered structure can be tailored to effectively transform the energy of incident pressure wave into shear wave energy. Furthermore, by integrating a layer of shear-dissipative material, the resulting shear-wave energy can be dissipated within the viscoelastic layer.

Chapter 1

Introduction

1.1. Stress-wave energy management

Wave propagation in continuum mechanics has been an interesting subject of research for decades. The subject of this dissertation is to study various techniques to take control of stress-wave propagation in solids. The energy carried by a plane-wave may constitute pressure wave energy and/or shear wave energy. The proposed techniques demonstrate that one can redirect and guide stress-wave energy, transfer pressure wave energy into shear wave energy, and dissipate the energy of shear waves; thus managing the propagation of stress-wave in solids. The methods are numerically established and experimentally verified.

The application of this technology consists of guiding the energy of the acoustic waves either away from or toward a region within the material, depending on whether one wishes to avoid or harvest the corresponding stress waves. Sensitive objects or facilities can be protected against undesirable acoustic disturbances and/or remained hidden from detection sonar.

1.2. Microstructural design

In order to achieve immense control on stress-wave propagation in solids, the material properties and the microstructure should be meticulously designed. It is established that wave speed and group velocity are strongly directional dependent in a highly anisotropic material such as composite materials. One can create heterogeneously anisotropic materials by controlling the fiber orientation within a fiber-reinforced composite material. Glass and Carbon fiber-reinforced composites are used in this work to induce the desired local anisotropy, and yet to create a material that is essentially homogeneous at the scale of the considered wavelengths. Also, designing a porous microstructure using a shear-dissipative matrix is proposed to further enhance the dissipation of stress-wave energy.

Microstructural designs proposed in this dissertation incorporates distinct phenomenon in wave-propagation. In the first design, the preferred axis of a transversely isotropic material varies smoothly with location, which imposes a gradual change of anisotropy in the material elasticity tensor. The detailed discussion in Chapter 2 exploits this design in order to guide the impinging pressure waves. The second design employs the significant role of interface discontinuity and elastic anisotropy in stress-wave energy management. The transmission and reflection of an incident wave are tailored in Chapter

3 to manage stress-waves at the interface of strongly directional carbon-fiber reinforced composites.

1.3. Organization of chapters

This manuscript is organized in the following manner. In chapter 2, we have shown numerically and experimentally that managing the energy of stress-waves is possible by designing the preferred axis of a transversely isotropic material to vary smoothly with location. In transversely isotropic materials, when the wave vector deviates only slightly from the axis of maximum stiffness, almost all the energy of longitudinal mode of plane wave will travel along this axis. We have designed a specimen in which the anisotropy direction changes smoothly in order to split and redirect stress waves around a target object and then re-combine them on the opposite side of the object (referred to as “acoustic cloaking” in the literature). It is numerically shown and experimentally demonstrated that the acoustic wave energy packet would follow a similar gradual change as the axis of anisotropy.

In chapter 3, the scattering of an incident plane wave at the interface of two transversely isotropic materials is studied. Plane wave propagation in anisotropic media is decomposed to three supported modes: quasi-longitudinal, quasi-shear, and pure shear. The direction of propagation, amplitudes, phase velocity, group velocity, and energy flux of reflected and transmitted waves are computed by formulating the theoretical approach in a MATLAB based computational platform. It is shown that the direction of propagation of the energy in solids can be easily controlled by designing the orientation of anisotropy of interfacing materials, which may be used to redirect and guide the energy of stress-waves either away or toward a region within the material, depending on whether one wishes to avoid or harvest the corresponding stress waves. Also we show that the interface of anisotropic materials can be tailored in order to efficiently transfer the energy of pressure waves into shear wave energy, which is susceptible to dissipation.

In chapter 4, we show that multilayered structures consisting of strongly anisotropic layers can be exploited to efficiently manage the stress wave propagation by providing multiple interfaces that play key roles in transmission and reflection of pressure and shear waves. Anisotropic layers introduce various design parameters which can be optimized to control the impinging stress waves as desired. We have developed a computational platform to efficiently evaluate the transmitted and reflected stress-waves in pressure and shear mode based on the anisotropy orientation of layers and the incident wave vector direction. We demonstrate that a multilayered structure can be tailored to effectively transform the energy of incident pressure wave into shear wave energy. Furthermore, by integrating a layer of shear-dissipative material, the resulting shear-wave energy can be dissipated within the viscoelastic layer.

Finally, in chapter 5, we have studied the chemistry, synthesis, and characterization of polyurea based foam. We modified the chemistry reactions incorporated to synthesize pure polyurea, in order to create a porous structure with 100-250μm voids. The broken water droplets in the emulsion of water and Versalink react with isocyanate molecules to form CO_2 that acts as a blowing agent to create foam. The developed synthesis procedure has an inherent issue that leads to non-uniform distribution of voids, and therefore non-uniform mass density in the whole sample. The samples were characterized for the developed microstructure as well as mechanical properties in macro scale. The porous microstructure was studied to find the void size due to each stoichiometry implemented in the material synthesis. Stress-strain behavior under uniaxial compression was studied for loading and unloading cycles. Storage and loss moduli were measured using DMA; and compared to the numerical predictions using micromechanics model for periodic distribution of voids.

Chapter 2

Stress-wave Energy Management through Material Anisotropy

Stress-wave propagation in solids can be controlled through imposing a gradual change of anisotropy in the material elasticity tensor. In this study, a transversely isotropic material is incorporated with a smoothly varying axis of anisotropy. It is shown that if this axis initially coincides with the stress wave vector, then the energy of the plane waves would closely follow this gradually changing material direction. A fiber-reinforced composite is used to induce the required anisotropy, and to experimentally demonstrate the management of stress-wave energy in a desired trajectory. The material has isotropic mass density and is considered homogeneous at the scale of the considered wave-lengths, even though microscopically it is highly heterogeneous.

2.1. Introduction

In recent years, there have been significant efforts to develop techniques to “cloak” an object, making it invisible to electromagnetic waves at a certain wave length.

These cloaks are generally based on using heterogeneous composites with gradually changing electromagnetic properties [1-4]. Schurig et al. [5] experimentally demonstrated EM cloaking at microwave frequencies. Milton et al. [6] studied the properties of conventional elastodynamics equations under curvilinear coordinate-transformation and found that in general, equations of motion are not form invariant and therefore the EM cloaking techniques, based on coordinate transformations, are not applicable to elastic stress waves. Cummer and Schurig [7] suggested an acoustic cloaking scheme by noting the equivalence of acoustic and electromagnetic equations in two-dimensional (2D) geometry, using anisotropic mass density. Chen and Chan [8] suggested a design of 3D acoustic cloak by mapping acoustic equation to DC conductivity equation, again using anisotropic mass density. Torrent and Sanchez-Dehesa [9] proposed a multilayered composite made of sonic crystals which satisfies anisotropic density requirements suggested by Cummer.

Recently, Norris [10] has shown that if the mechanical stiffness of the material is isotropic, then the inertial density must be infinite at the inner surface of the cloak. In fact the inertial anisotropy schemes suggested in the literature are of this kind [7-9]. Cloaking is suggested by numerical modeling in those cases, but fabricating a metamaterial with infinite mass density is challenging, if not impossible. Norris then shows that perfect cloaking is possible with finite mass through stiffness anisotropy. Pentamode materials (PM) are needed to satisfy the required stiffness anisotropy [6, 10]. It can also be used in line with inertial anisotropy (but not infinite mass density) [10]. Yet, fabrication of such metamaterials is rather challenging. Five of the six eigenvalues of the elasticity tensor vanish in PM and therefore it can be strained in 5 independent modes without producing any stress which causes instability in the material [6, 10]. Tehranian et al. [11] found that it is possible to design the microstructure of a material to attain an elasticity tensor which varies smoothly with position; and can be used to guide the energy of stress waves.

Acoustic cloaking can be achieved when stress waves are guided around an object and then re-gathered on the far side of the cloaked region to continue traveling in the same direction so as to make the object seem invisible or protected from the impinging stress waves. A less strict approach may be to seek to minimize the elastodynamic scattering cross section of any object within a bounded volume by adjusting the local material properties of its surrounding region. The term material properties in this description refers to the effective mass-density and elasticity (or viscoelasticity) tensors that depend on the microstructure at a length-scale that is at least an order of magnitude smaller than the considered window of acoustic wavelengths.

In the present study, we seek to develop a realistic approach to control stress-wave propagation in elastic solids of uniform mass-density but anisotropic elasticity, and demonstrate its feasibility through numerical simulations and experiments at ultrasonic acoustic frequency range. An ideal cloak guides the stress-waves around an obstacle at any angle of incidence and at any frequency. The design suggested in this paper limits the angle of incidence to a direction normal to the boundary surface on which the wave impinges. But, it does that successfully in a relatively wide frequency band. In general, a micro-structurally designed cloak cannot operate over the entire frequency spectrum, not only because of theoretical limitations, but also more simply due to the diffraction limit of heterogeneous media. Basic elastodynamic analysis of anisotropic media shows that the longitudinal and shear waves may travel in different directions with different velocities that depend on the angle between the wave vector and the material's principal anisotropy directions [12-14]. However, if the wave vector makes a very small angle with the material's preferred axis of maximum stiffness, then the resulting longitudinal and shear-wave group velocities will make even smaller angles to this direction. In other words, the maximum stiffness direction is also a preferred direction for group velocity and wave-energy flow. Now, if the material direction changes smoothly (with respect to the wavelength) throughout a body, the stress waves will follow the anisotropy direction of the material. Thus, we can control stress waves and redirect them to travel along a pre-designed trajectory.

Musgrave [14] has performed an extensive study on wave propagation in elastic anisotropic media and the corresponding slowness surfaces for different modes. Norris [15] developed a general theory for the propagation and scattering of compact Gaussian shaped envelopes in piecewise homogeneous anisotropic solids. Abrahams and Wickham [16] used an asymptotic method to solve the problem of refraction and propagation of SH waves with relatively large wave-number in a locally transversely isotropic material whose direction of the preferred axis varies as a continuously differentiable function of a single spatial coordinate. Their work is motivated by failure of ray tracing methods in non-destructive testing of austenitic steel welds, which can be modeled as transversely isotropic material with smoothly varying axis of symmetry. Their method can produce a geometrical characterization of the refracted wave. Mazzucato and Rachele [17] studied intersection of slowness surfaces of different modes using microlocal analysis on transversely isotropic materials where the fiber direction may vary smoothly from point to point. Norris and Wickham [18] studied the structure and properties of the ray equation for transversely isotropic materials with moduli which are uniform up to a rotation of the underlying crystallographic base vectors about a common axis. They suggested an algorithm for SH waves that can be used to generate a uniform approximation to the point source field in a smoothly varying medium.

In the present work, we are concerned with longitudinal waves, which, in general, may involve all three displacement components. Given the complexity of the geometry of the problem, we chose to use numerical computation using finite element method. The moduli of each element are specified based on its spatial location. In section 2.2, we seek to provide a basic understanding of the physics of the phenomena using the classical fundamentals of wave propagation in transversely isotropic materials.

Fiber-reinforced composites are used in this work to induce the desired local anisotropy, and yet to create a material that is essentially homogeneous at the scale of the considered wavelengths. One can then change the preferred material axis by controlling the fiber orientation within a sample. In a composite material with a spatially uniform preferred direction, longitudinal waves and shear waves travel in certain directions depending on the angle between the wave vector and the preferred axis (fiber orientation in this case). However, if continuous fibers are oriented in smoothly curved shapes, both longitudinal and shear waves will travel on paths that approximately follow the fibers.

The acoustic waves tend to travel close to the direction of the highest stiffness and wave speed. It must be emphasized that unlike wave-guides which exploit geometric surfaces with material discontinuities, the wave redirection considered here is achieved in the absence of discontinuous boundaries. The present three-dimensional solid sample is essentially a homogeneous but highly anisotropic at the scale of the considered wavelengths. Note that the sample is fabricated such that its (varying) elastic modulus tensor at any point is obtained by a pre-designed rotation of its principal directions. It is important to realize that the macroscopic anisotropy of the material guides the acoustic waves, not the microscopic heterogeneity in the composite material. In fact, the scale of the material heterogeneity is what limits the wavelength at which the stress-wave energy can be managed. Fortunately, this range is extremely wide for a fiberglass/epoxy composite material, covering stress waves of up to about 5MHz frequency. In principle, smaller fibers will allow one to surpass this limit. Applications of acoustic cloaking may include hiding under-water objects such as submarines, protecting a particularly sensitive section of a structure against blast or shock waves, acoustic noise reduction by creating sound-shielding materials, and seismic isolation of civil infrastructure.

2.2. Elastic waves in anisotropic materials

In anisotropic materials with spatially uniform density, elastic wave propagation is strongly affected by the local principal directions of the material anisotropy. This fact can be used to redirect and manage the elastic stress-wave energy within a material, essentially as is desired. Here, we illustrate this phenomenon using an elastic material which is locally transversely isotropic, but whose local principal plane of isotropy spatially varies from point to point.

With respect to a rectangular Cartesian coordinate system, x_j, j = 1, 2, 3, the equations of motion are,

$$\frac{\partial \sigma_{ij}}{\partial x_j} = \rho \frac{\partial^2 u_i}{\partial t^2}, \tag{2-1}$$

where σ_{ij}, u_i, $i, j = 1, 2, 3,$ and ρ respectively denote the Cartesian components of the stress tensor, displacement vector, and mass-density [14, 19]. The generalized Hooke's Law is $\sigma_{ij} = C_{ijkl} u_{k,l}$, where comma followed by an index denotes partial differentiation with respect to the corresponding coordinate. Since the elasticity tensor, C_{ijkl}, is spatially variable, $\frac{\partial \sigma_{ij}}{\partial x_j} = \rho \frac{\partial^2 u_i}{\partial t^2}$,

(2-1) becomes

$$\frac{\partial}{\partial x_j}\left(C_{ijkl} \frac{\partial u_k}{\partial x_l} \right) = \rho \frac{\partial^2 u_i}{\partial t^2}. \tag{2-2}$$

For numerical finite-element simulations, it is convenient to consider a typical finite element, x_j, j = 1, 2, 3, denote the local rectangular Cartesian coordinate system, and examine plane wave propagation within this element which is now assumed to be uniform. Then integrate the results into the large-scale finite-element code, LS-DYNA, to solve the corresponding elastic waves propagating through an elastic solid whose principal axes of elasticity tensor may vary from element to element.

We now focus on a transversely isotropic material. Plane wave solution to the equation of motion is in the following form:

$$u_i = g_i\left(n_j x_j - Vt\right), \tag{2-3}$$

where n_j are components of the unit vector normal to the wave-plane, moving with speed V, and repeated indices are summed [12]. Substituting this solution into the equation of motion, and noting that the elasticity tensor in the considered element is constant, we obtain,

$$(C_{ijkl}\, n_l\, n_j - \rho V^2 \delta_{ik})\, g_k'' = 0\,. \tag{2-4}$$

For nontrivial solutions, we must have,

$$\det(C_{ijkl}\, n_l\, n_j - \rho V^2 \delta_{ik}) = 0\,. \tag{2-5}$$

For an element with transversely isotropic elasticity, we chose the x_3-axis normal to the plane of isotropy. The elastic modulus matrix $[C_{ab}]$ is

$$C_{1111} = C_{11} = D\left\{\frac{1}{EE_3} - \frac{\nu_3{}^2}{E_3{}^2}\right\}, \qquad C_{1122} = C_{12} = D\left\{\frac{\nu}{EE_3} + \frac{\nu_3{}^2}{E_3{}^2}\right\},$$

$$C_{1133} = C_{13} = D\frac{(1+\nu)\nu_3}{EE_3}, \qquad C_{3333} = C_{33} = D\frac{1-\nu^2}{E^2}, \tag{2-6}$$

$$C_{2323} = C_{44} = \mu_3, \qquad D \equiv \frac{E^2E_3{}^2}{(1+\nu)\left\{(1-\nu)E_3 - 2\nu_3{}^2E\right\}}.$$

These equations involve 5 independent elastic constants. These are: Young moduli E in the x_1 and x_2 , and E_3 in the x_3 directions; Poisson ratios, ν the x_1 and x_2 , and ν_3 in the x_3 directions, respectively, and shear modulus, μ_3 , in the x_1,x_3 and x_2,x_3 planes, the shear modulus in the plane of isotropy being $\mu = E/2(1+\nu) = (C_{11}-C_{12})/2$.

Taking $\boldsymbol{n} = (\sin\theta, 0, \cos\theta)$ for a plane-wave which makes an angle θ with the x_3 axis in the x_1x_3-plane, we obtain the characteristic equation,

$$\left[C_{44}\cos^2\theta + \tfrac{1}{2}(C_{11}-C_{12})\sin^2\theta - \rho V^2\right]\left[C_{44}C_{33}\cos^4\theta + \left\{C_{44}{}^2 + C_{11}C_{33} - (C_{13}+C_{44})^2\right\}\sin^2\theta\cos^2\theta \right.$$
$$\left. + C_{44}C_{11}\sin^4\theta - \rho V^2(C_{33}+C_{44})\cos^2\theta - \rho V^2(C_{11}+C_{44})\sin^2\theta + (\rho V^2)^2\right] = 0. \tag{2-7}$$

The roots of this equation now yield the inverse (i.e., the *slowness*) of the velocities of three different plane waves that can travel in a transversely isotropic material, as follows [13]:

1- Quasi-shear mode:

$$\frac{1}{V_1}=\left(\frac{k}{\omega}\right)_1=(2\rho)^{1/2}\Big[C_{11}\sin^2\theta+C_{33}\cos^2\theta+C_{44}$$
$$-\sqrt{[(C_{11}-C_{44})\sin^2\theta+(C_{44}-C_{33})\cos^2\theta]^2+(C_{13}+C_{44})^2\sin^2 2\theta}\,\Big]^{-1/2} \tag{2-8}$$

2- Pure Shear mode:

$$\frac{1}{V_2}=\left(\frac{k}{\omega}\right)_2=\left(\frac{\rho}{\frac{(C_{11}-C_{12})}{2}\sin^2\theta+C_{44}\cos^2\theta}\right)^{1/2}, \tag{2-9}$$

3- Quasi-longitudinal mode:

$$\frac{1}{V_3}=\left(\frac{k}{\omega}\right)_3=(2\rho)^{1/2}\Big[C_{11}\sin^2\theta+C_{33}\cos^2\theta+C_{44}$$
$$+\sqrt{[(C_{11}-C_{44})\sin^2\theta+(C_{44}-C_{33})\cos^2\theta]^2+(C_{13}+C_{44})^2\sin^2 2\theta}\,\Big]^{-1/2}. \tag{2-10}$$

As an illustration, Figure 2.1 shows the variation of these three quantities for various values of the angle θ. These curves are drawn for the following elastic constants: E = 15.37GPa, E_3 = 48.46GPa, ν = 0.34, ν_3 = 0.24, μ_3 = 5.47GPa. These values are obtained by characterizing a transversely isotropic composite material, as discussed in Section 2.4. Also, these values are used to produce results discussed in the rest of this section, as well as for all other experimental results that are reported in this paper.

For anisotropic media, the wave vector $\boldsymbol{k} = k\boldsymbol{n}$ (where k is its magnitude) and the group velocity $\boldsymbol{V}_g$ with magnitude V_g do not always have a common direction, where

$V_g = \dfrac{\partial \omega}{\partial k}$ [13, 20]. Since δ***k*** must always lie in the slowness surface, the group velocity is normal to the slowness surface, as shown in Figure 2.1. It can be seen that the direction of the group velocity is different for different modes corresponding to the same angle, θ. A more detailed discussion of creating such slowness curve is provided in [12], Auld [13] and Mazzucato and Rachele [17] ; see however Payton [12] who focuses on transversely isotropic media.

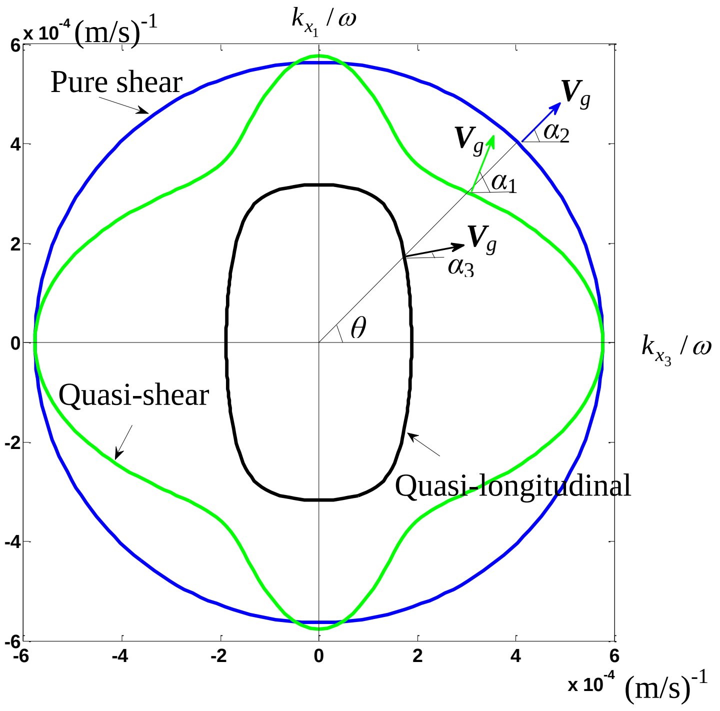

Figure 2.1: Slowness curves for a transversely isotropic material

As a simple example, consider a transversely isotropic sample shown in Figure 2.2, with the x_3-axis making an angle θ = 45° with the wave vector ***k***. In this case, θ is uniform throughout the sample. The wave packet travels with a group velocity that makes an angle α with the x_3-direction, as displayed in Figure 2.1 for the three waves mentioned above.

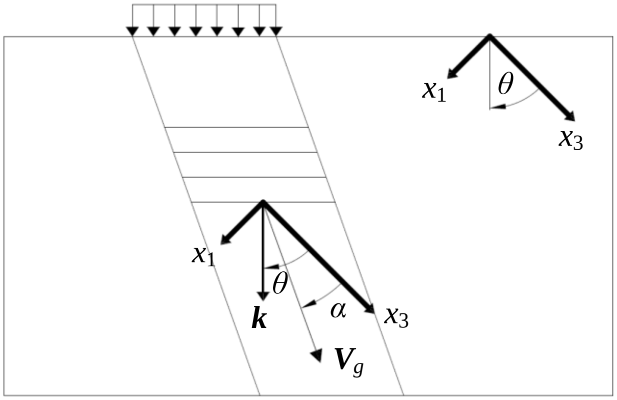

Figure 2.2: Deflected acoustic wave trajectory in anisotropic material

Pure shear waves travel almost in the ***k***-direction at a velocity of V_2 = 1755m/s. Quasi-longitudinal waves travel at V_3 = 4070m/s, making an angle α_3 = 11°, and the quasi-shear waves at V_1 = 2344m/s making an angle of about α_1 = 65° relative to the x_3-direction, as shown in Figure 2.1. In this case, plane strain is assumed and the displacement in the y-direction (vertical direction in Figure 2.2) is prescribed over a 20 mm strip as a harmonic sinusoidal wave with 1MHz frequency. The rest of the boundary is stress-free.

The simulations give V_3 = 4300m/s, and V_1 = 2322m/s, with the corresponding angles α_3 = 13°, and α_1 = 67°. None of the waves travel in the anisotropy (x_3-direction) of the material, as the wave vector does not coincide with the x_3-direction. These are plotted in Figure 2.3, which shows the effective stress (von Mises) at a specific time after the excitation begins. Red fringes show higher effective stresses (von Mises) while blue shows zero effective stress. The maximum effective stress experienced at each element on the bottom side of the sample is found and plotted (blue dots) below the sample in Figure 2.3. Points *B* and *C* (marked on the sample) correspond to two local maxima. Line *AB* shows the direction of propagation of quasi-longitudinal waves and line *AC* that of quasi-shear waves. Also, the time it takes for waves to travel from point *A* to *B* and *C* is computed based on the 5th sine wave peak. Pure shear waves are traveling slower than the other modes and cannot be seen in Figure 2.3, as effective stress in the model is dominated by quasi-longitudinal waves. However, theoretical values show that these waves make an angle $\alpha_2 = 45°$.with x_3.

In numerical simulation, wave speeds and deflection angles are calculated based on the von Mises stress which represents distortional energy. This may be one reason for the slight difference between numerical results and the analytical values which are calculated based on slowness curves. Displacement of the nodes can be decomposed in three discussed modes to obtain angles and speeds of the waves.

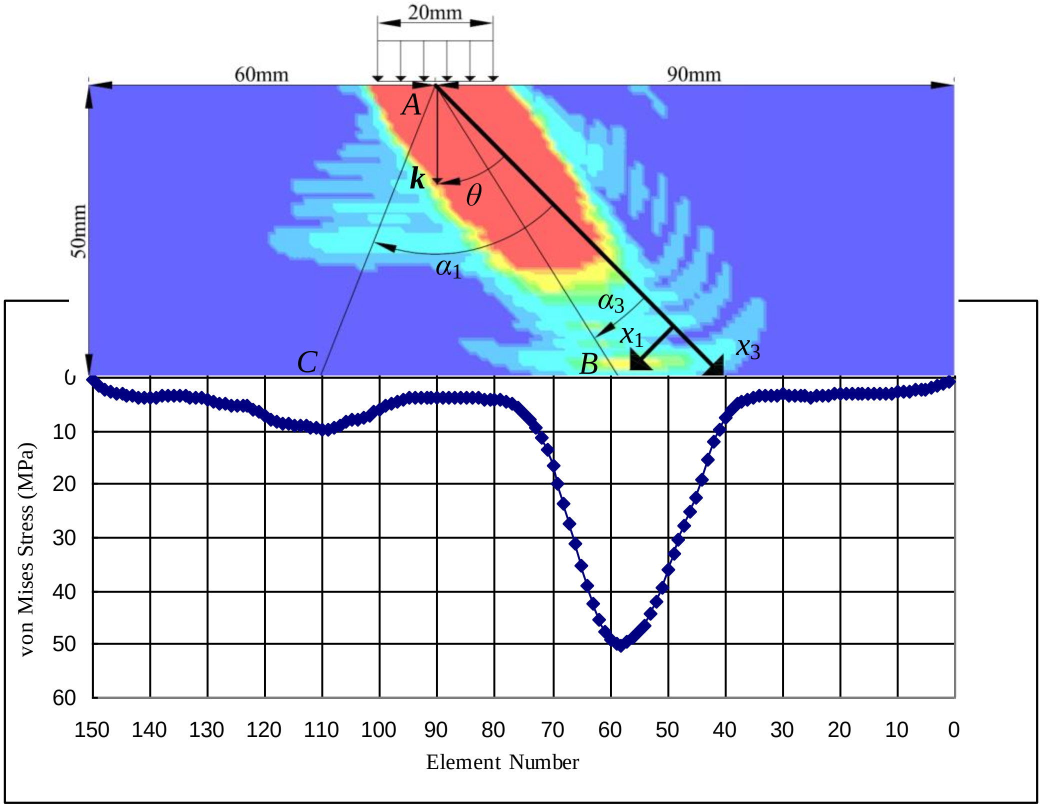

Figure 2.3: Numerical simulation of wave propagation in a transversely isotropic material

When the wave vector deviates only slightly from the material's principal x_3-direction, as shown in Figure 2.4, then pure shear, quasi-longitudinal, and quasi-shear waves all travel more or less in the x_3-direction. Now, if the material anisotropy direction changes slightly, the group velocity will follow the same and changes accordingly. If initially the wave vector coincides with the material's principal direction and undergoes smooth changes, then the acoustic wave energy packet would follow a similar path. Thus, it is possible to control the elastic energy path by the judicious design of material anisotropy. This is illustrated, both experimentally and numerically, in the next two sections.

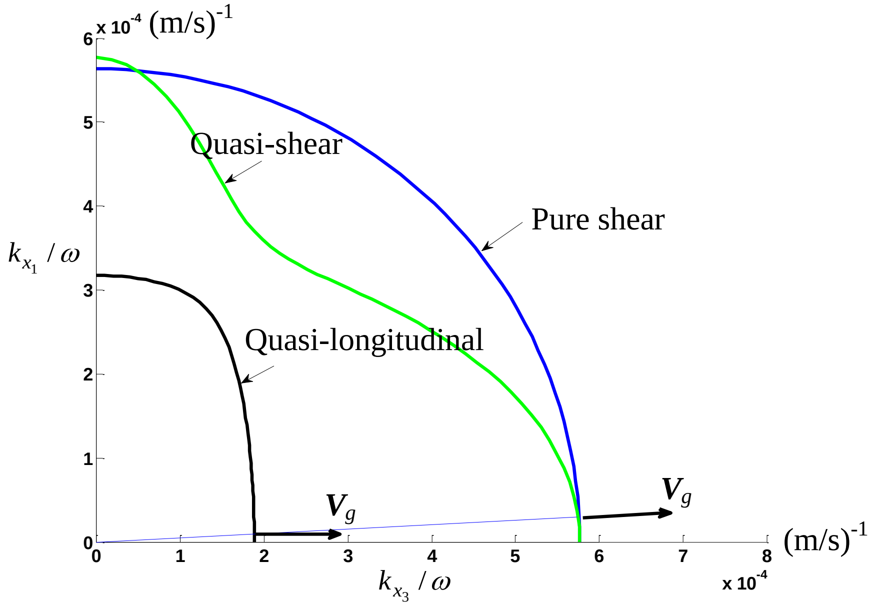

Figure 2.4: Slowness curves analysis where ***k*** is applied close to x_3-axis

2.3. Numerical computation

The objective of this section is to design and numerically simulate a possible specimen, which can split, when necessary, and redirect acoustic stress waves around a target object and then re-combine them on the opposite side of the object to produce waves that have their original spatial distribution, although they may be partially attenuated. We want to ensure that the interior object would be minimally excited by incident waves and thus remain protected and hidden to ultrasonic excitations. We use anisotropic materials to achieve this goal. We focus on transversely isotropic materials and consider cases where the anisotropy direction (referred to as the axis of anisotropy) smoothly and gradually changes within the solid and hence redirects the waves as desired. Except for the direction of the elastic anisotropy, the material appears homogeneous at the scale of the considered wave lengths. In the following subsections we first present a simple model and then analyze a sample which we have fabricated for experimental verification, as discussed in section 2.4.

2.3.1. Circularly varying axis of anisotropy

A simple model is presented in this section to illustrate acoustic energy management in a transversely isotropic cube, shown in Figure 2.5. In this model, the axis of elastic anisotropy at each point is tangent to a circle of a common center. The LS-DYNA finite-element model is a cube with 10cm long sides as shown in Figure 2.5. The local material x_3-axis, which coincides with the direction of maximum stiffness, is changing throughout the model. At each element, the x_3-axis would be normal to the radial line connecting that element to the specimen's axis of radial symmetry [21]. A load-free boundary condition is prescribed at all surface nodes; except for those on a 2cm × 2cm area centered at *T*. These nodes are oscillated with a single 100kHz sinusoidal pulse (from t = 1μsec to t = 11μsec) along the global ***Y***-direction with 10μm amplitude, followed by zero ***Y***-displacement throughout the rest of the simulation. We are going to look at the effective stress on the mid-plane made by *TRGL* in Figure 2.5.

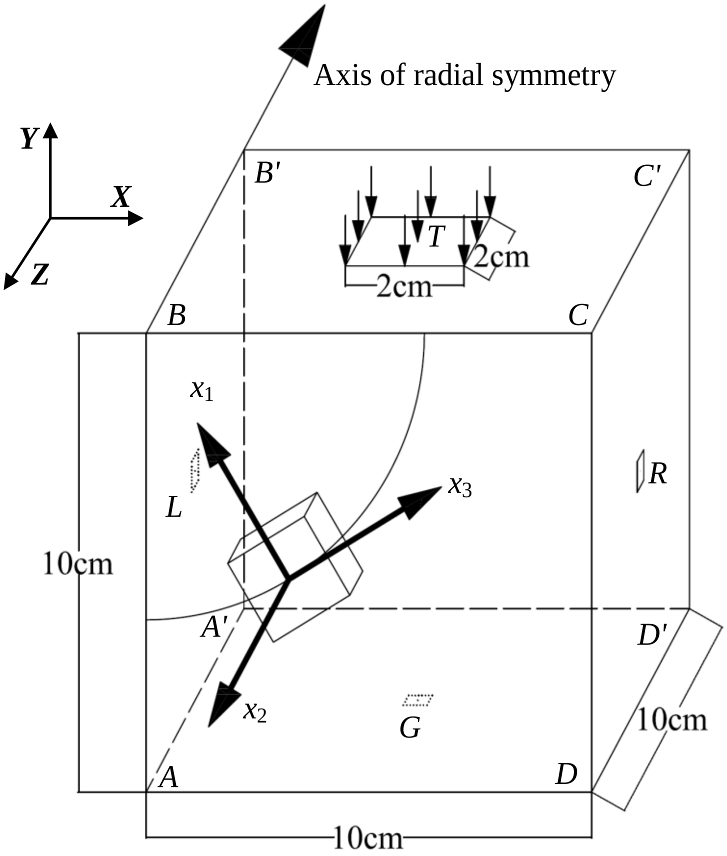

Figure 2.5: Cubic sample with circular anisotropy. At each point in a plane normal to the x_2-axis, the axis of anisotropy, x_3, is normal to the radial line connecting that point to the corresponding point on the edge *BB'*.

The maximum stiffness direction, x_3, changes smoothly as the wave is propagating in the model. It can be seen from Figure 2.6 that acoustic-wave energy is directed along the x_3-direction. Initially, both the wave vector $\boldsymbol{k}$ and the x_3-direction are in the ***Y***-direction, but the group velocity of acoustic waves gradually changes its direction and follows the local material's axis of anisotropy, x_3. The normal displacement of the nodes at the center of cube's faces, i.e., points *T*, *R*, *G*, *L*, are plotted in Figure 2.7; i.e., the ***X***-displacement for *R* and *L*, and the ***Y***-displacement for *T* and *G*. The displacement of node *L* is much larger than that of the others, as the acoustic wave is redirected towards *L*.

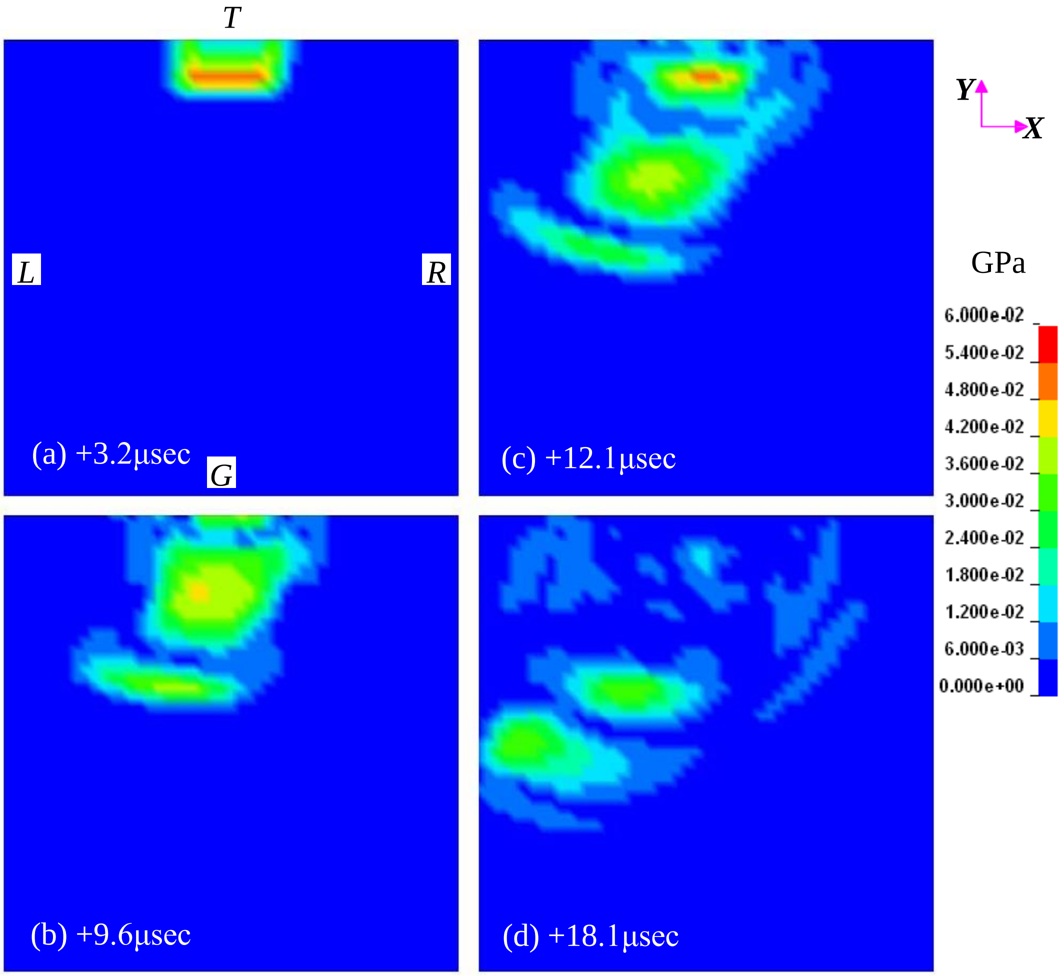

Figure 2.6: The von Mises stress in mid-plane, *TRLG*, of the model shown in Figure 2.5.

2.3.2. Stress-wave redirection

In this section, we consider a sample with an interior cavity and examine two transversely isotropic cases to illustrate and contrast the effect of variation of the axis of anisotropy (maximum stiffness direction, the x_3-axis) on the acoustic wave path. The general geometry of the sample is shown in Figure 2.8a; see also Figure 2.14 for an actual fabricated sample. One sample, (model A), has its x_3-axis parallel to the $\boldsymbol{X}$-direction at each point within the sample, Figure 2.8a, while in the other sample, (model B), the direction of the x_3-axis follows a smoothly curving path around the central cavity, Figure 2.8b. The density and degree of anisotropy (E_3/E_1) are constant throughout both models. That is, any two elements taken from different parts of each model have identical density and elasticity tensors in their corresponding local principal anisotropy coordinate system. Only the axes x_1 and x_3 change with respect to the global coordinate system for model B, but not for model A, while their x_2-direction remains uniform in both cases.

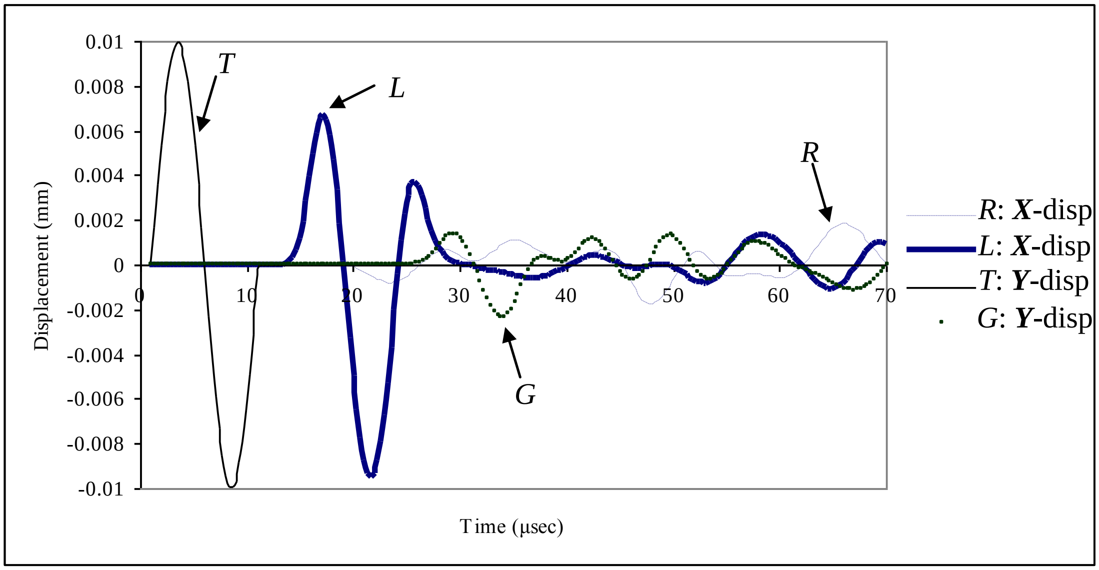

Figure 2.7: Normal displacement at the center of four faces of the cube, as identified in Figure 2.5

Model A, (the sample with a unidirectional transverse isotropy, Figure 2.8a), is simulated as a baseline to contrast the results with the stress-wave path in model B of Figure 2.8b. The local elastic constants at each point are the same as those in Section 2.4.1, Figure 2.5. Both models are 11cm long in the ***X***-direction, and 5cm wide in the ***Y***-direction.

Model B has the same geometry, same homogeneous mass density, and same elastic moduli in local material coordinates as model A, but with different local material axes x_1 and x_3; while x_2 remains constant throughout the model (Figure 2.8b). Solid lines in Figure 2.8b show how the x_3-axis varies in the model in order to conform to the geometry of central cavity. The x_1-axis is chosen such as to render the 123 coordinate system right-handed and orthogonal.

Each of the models is subjected to a single 1MHz sinusoidal pulse of 100N force in the ***X***-direction over each node on a 1cm strip centered at point M, of one face of the sample (left face in Figure 2.8a and b). The sinusoidal load is applied from t = 2μsec to t = 3μsec, and after that all nodes are load-free. The rest of the boundary, including the central cavity is stress-free in both cases. In order to solve the problem in plain strain, out-of-plane degrees of freedom (the ***Z***-displacement) are constrained for all the solid elements.

Finite-element calculation is performed using LS-DYNA. The effective stress (von Mises) is computed in each element at each time-increment. The von Mises stress represents distortional energy and can be used to study the acoustic energy trajectory in the medium. The results are discussed below, starting with model A.

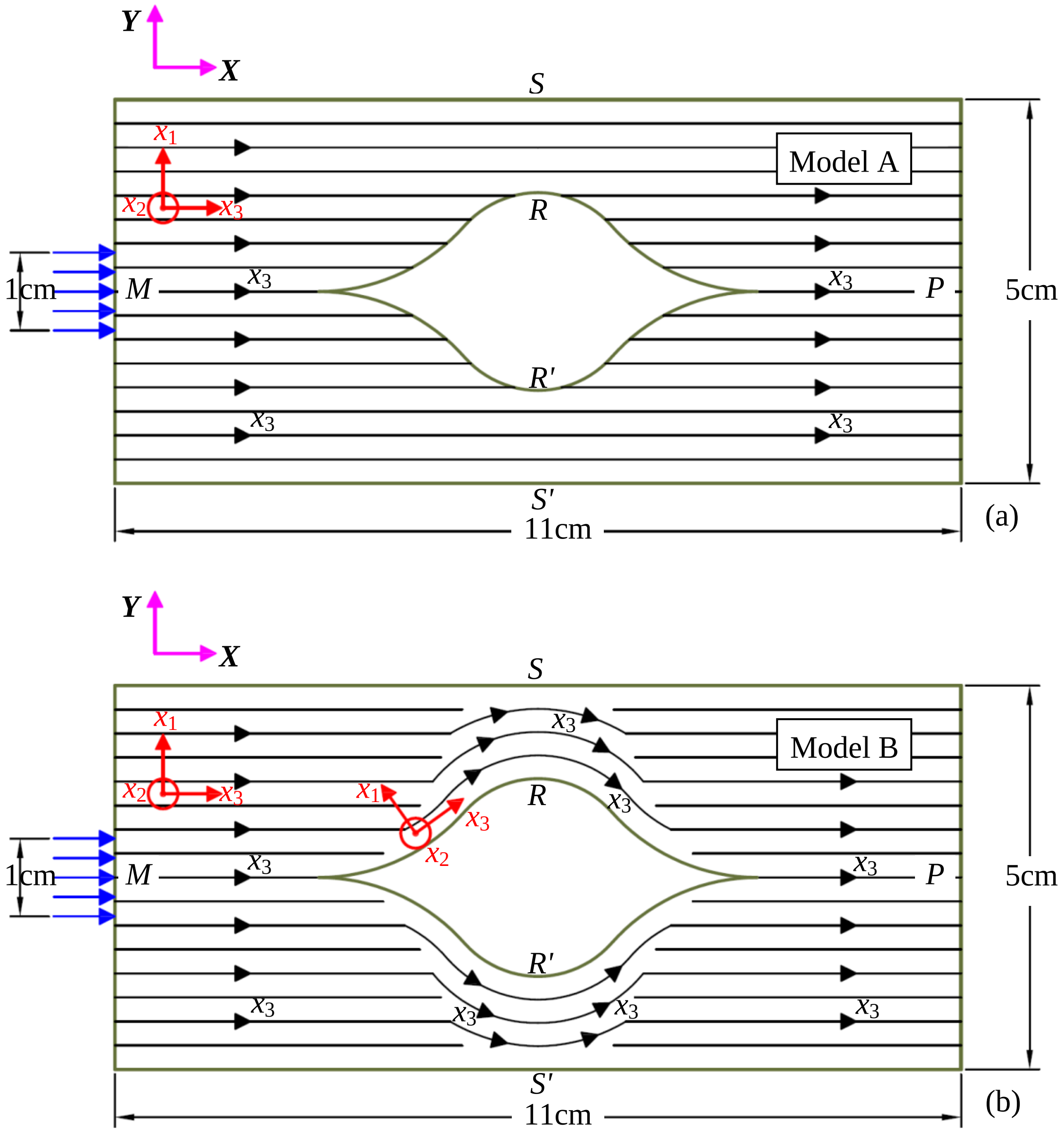

Figure 2.8: Orientation of the elastic anisotropy axis, the x_3-axis, in: (a) the baseline model with uniformly straight anisotropy axis, and (b) with an anisotropy axis that follow the indicated curved path around the central cavity.

Model A: The results for this baseline case are illustrated in Figure 2.9a. Red fringes show higher effective stresses while blue shows zero effective stress. The considered loading induces plane waves propagating in the direction of elastic anisotropy, i. e., at each point, the wave vector, $\boldsymbol{k}$, coincides with the corresponding x_3-axis. Slowness curves in Section 2.2 with $\theta = 0$ can be used to predict the direction of the group velocity. All three modes of the plane wave travel in the x_3-direction, as confirmed by Figure 2.9a. As the plane wave encounters the stress-free surface of the central cavity, it is reflected off that surface, scattering throughout the model as can be seen in Figure 2.9a(1-6).

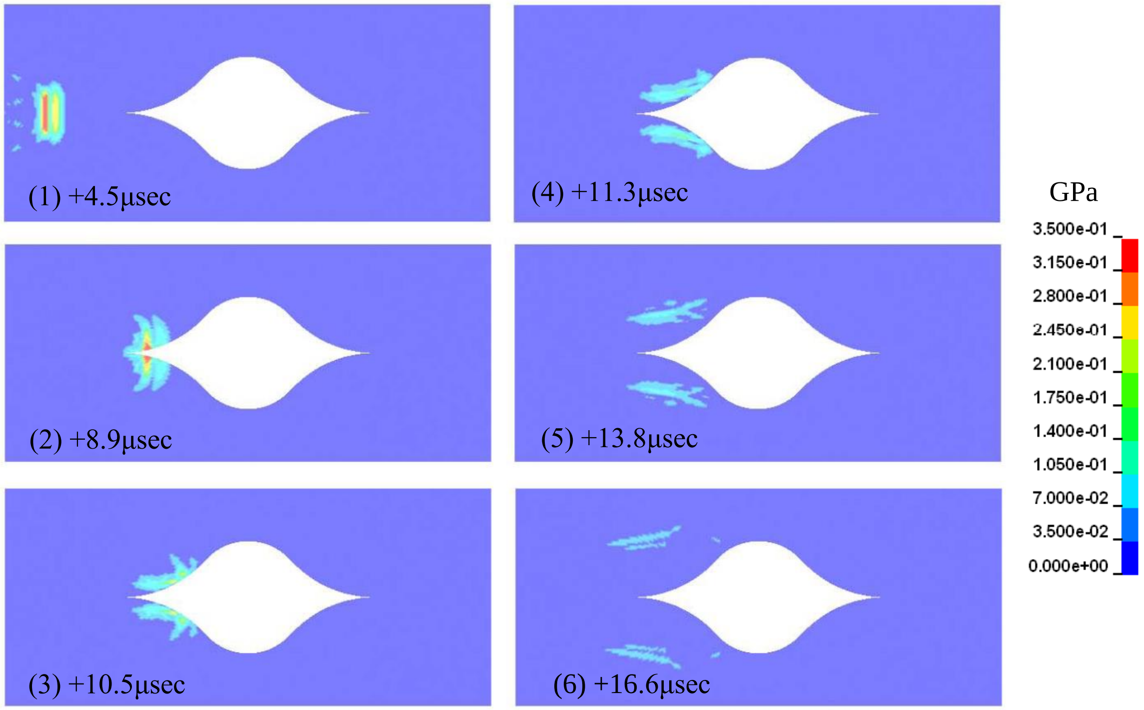

Figure 2.9a: The von Mises stress contours from numerical simulation of model A, plotted for a selected time sequence.

Model B: Here again, the wave vector is initially in the ***X***-direction that coincides with the local material x_3-axis. As the acoustic wave propagates in model B, it follows the direction of the x_3-axis that is changing, travels around the cavity, and finally returns to its initial direction. As suggested by the discussion on slowness curves in Section 2.2, the acoustic wave packet should follow the x_3-direction. Figure 2.9b shows selected snapshots of the von Mises stress-contour plots for model B. Figure 2.9b(1, 2) are essentially the same as those for the baseline model A; see Figure 2.9a(1, 2), since the anisotropy of the path traveled by the waves is similar. Since for model B the x_3-axis conforms to the geometry of the boundary of the central cavity, the wave path similarly changes and is redirected around the cavity. There is a small sudden change in x_3-direction at the transition from linear to curvilinear anisotropy along the sample. Figure 2.9b(3-5) show how most of the energy of the acoustic wave has followed the x_3-axis of the model. There are small reflections off the cavity surface that may be the result of small sudden changes in x_3-direction. However, the energy of the reflected waves is small compared to the bulk of the energy that travels around the cavity. Figure 2.9b(6, 7) show how each of the two wave packets has traveled, one above and the other below the central cavity, finally join to form a single packet of the plane wave that then travels along the x_3- or $\boldsymbol{k}$-direction, with most of the energy being concentrated at its center. Also, the sharp peaks in Figure 2.10c show that most of the energy of the acoustic waves has traveled very close to the opening surface. (Figure 2.9b(4) is the corresponding state.)

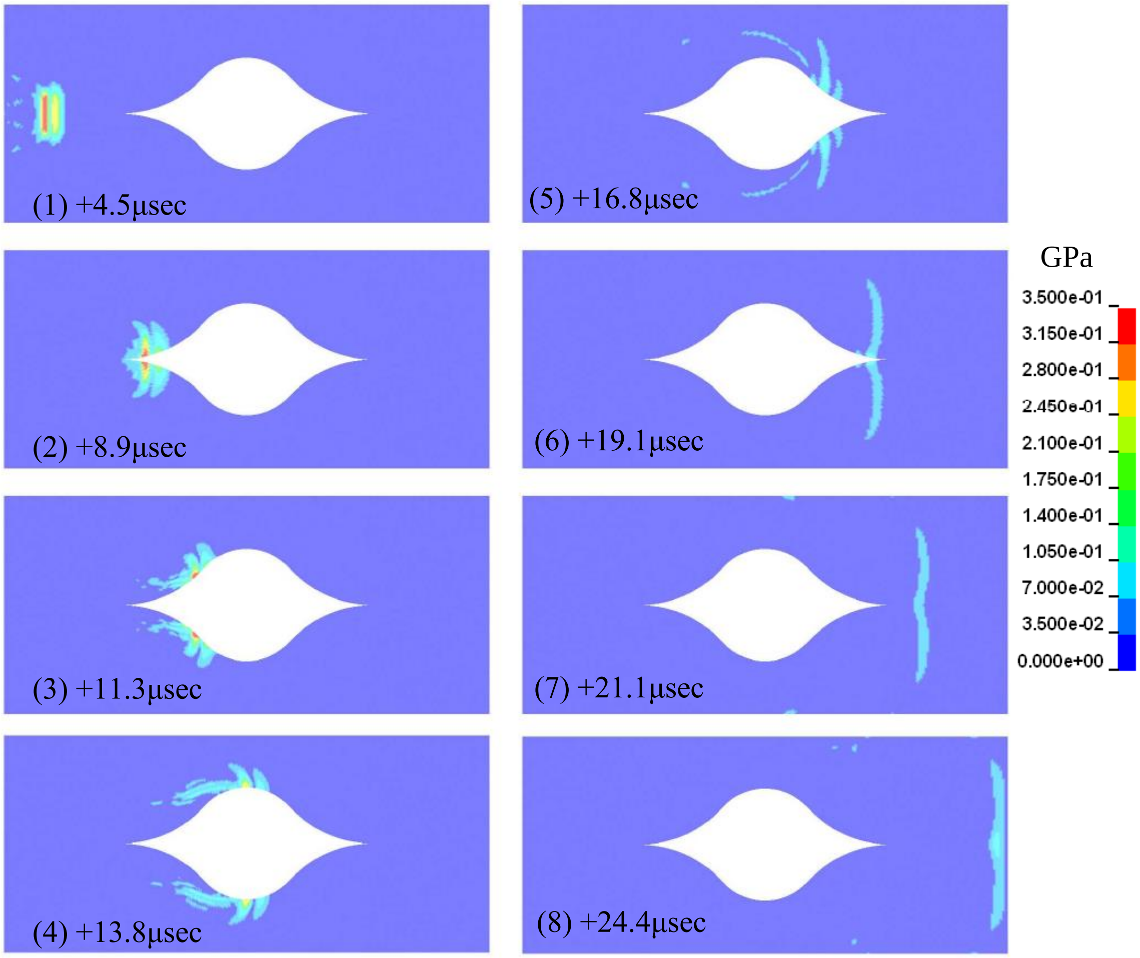

Figure 2.9b: The von Mises stress contours from numerical simulation of model B, plotted for a selected time sequence.

In Figure 2.10 we have plotted the maximum values of the ε_{XX}–strain attained over the considered time interval, at the end section of model (Figure 2.10a), in Figure 2.10b, and for section *A*-*A* (mid-section of the model), in Figure 2.10c. As can be seen in Figure 2.9a, most of the energy of the acoustic waves is scattered in the left half of the sample in model A. The light solid lines in Figure 2.10b and c represent the numerical results for the baseline model A.

The heavy solid lines represent the simulation results for model B. In comparison with similar graphs for model A, the wave redirection and re-formation is clearly demonstrated. Furthermore, we have normalized the signal measured experimentally using ultrasonic transducers (see Section 2.4 for details), in such a way that the peak of the experimental and the numerical profiles are equal. The experimental signals are shown by solid squares in the Figure 2.10b and c. After peak calibration, the experimental and numerical profiles are in good agreement.

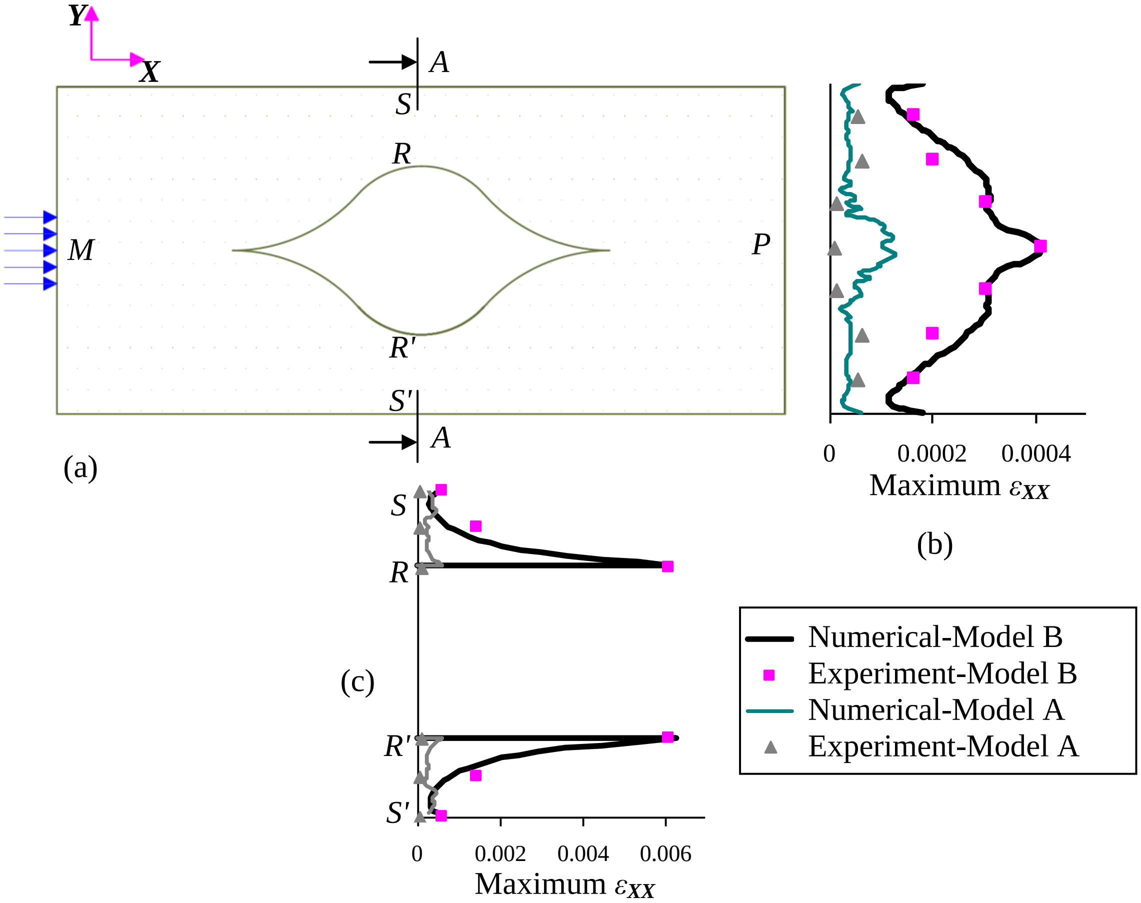

Figure 2.10: Numerical results in central excitation and comparison with experimental data. The light and heavy solids lines are the time maximum of the axial strain as calculated in numerical simulation for models A and B. The solid squares and triangles are experimentally measured voltage signals by ultrasonic transducers (see section 2.4). In b the numerical simulation results and experimental data are taken at the end surface of the sample, while c shows these quantities at cross section *A*-*A*. In each of the two graphs, only the peak experimental and numerical values for sample B are normalized to have the same geometric magnitude. The normalization factors for graphs (b) and (c) are different. The experimental and numerical profiles for model B are in close agreement, but they are substantially different than those in model A.

Figure 2.10b and c show that the strain peak for model B is about 10 times greater than for model A at the *A*-*A*-cross section; and more than three times greater on the surface of the model. Furthermore, comparing Figure 2.9a and b it is seen that, in model

B, the amount of energy transferred from the left-half of the model to the right-half is considerably greater than that of the baseline model. In fact, the small disturbance observed on the surface of the baseline model might be the result of surface waves and strongly depends on the boundary conditions, whereas in model B, the acoustic wave is guided in the designed direction and therefore most of its energy is concentrated in its trajectory. Thus, the transfer of the ultrasonic stress-waves is managed in this example by controlling the material anisotropy only and not the mass-density.

2.3.3. Off-center excitation

It is of interest to examine a case where the excitation in model B is applied off-center on its left face. Figure 2.11a shows the position of the nodes on which the sinusoidal excitation is imposed. The center of the excitation is 6.3mm off center of the model's left face. The maximum values of the ε_{XX}-strain over the considered time interval are plotted in Figure 2.11b and c at the end surface and mid-section of the model, respectively. The peak in maximum axial strain occurs at about 6.4mm off center, on the right face of the sample, very close to the eccentricity of the incident input pulse. The solid squares in Figure 2.11 correspond to the normalized measured data discussed in Section 2.4. Figure 2.12 shows how the effective stress is distributed in the model at a selected time sequence. Essentially, the same phenomenon that occurred in the centrally excited case is observed in the present case. The ultrasonic wave packet is guided around the central cavity of model B, and is delivered on the right-face over almost the same exact location as the corresponding location of the incident pulse.

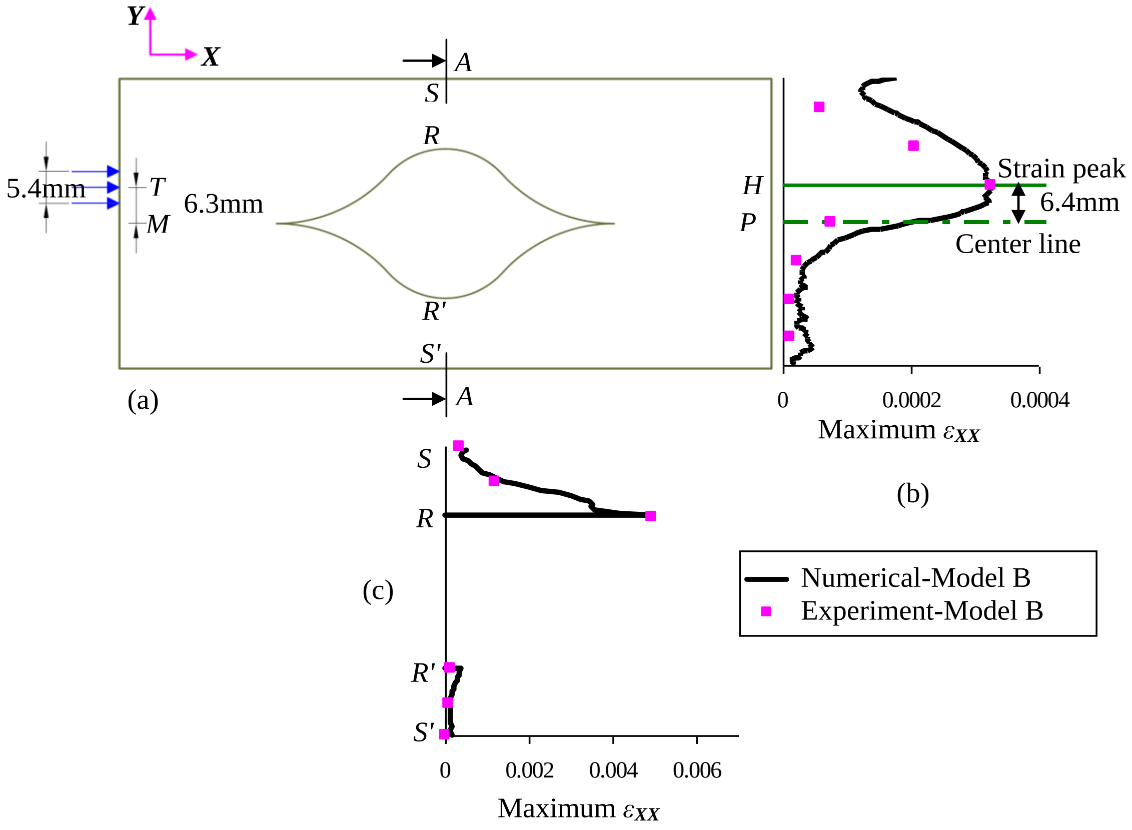

Figure 2.11: Numerical results in off-center excitation. In b and c, the solid lines are the results of numerical simulations; while the solid squares are experimentally measured signals (see Section 2.4). In each of the two graphs, only the peak experimental and numerical values are normalized to have the same geometric magnitude. The normalization factors are different in graphs (b) and (c).

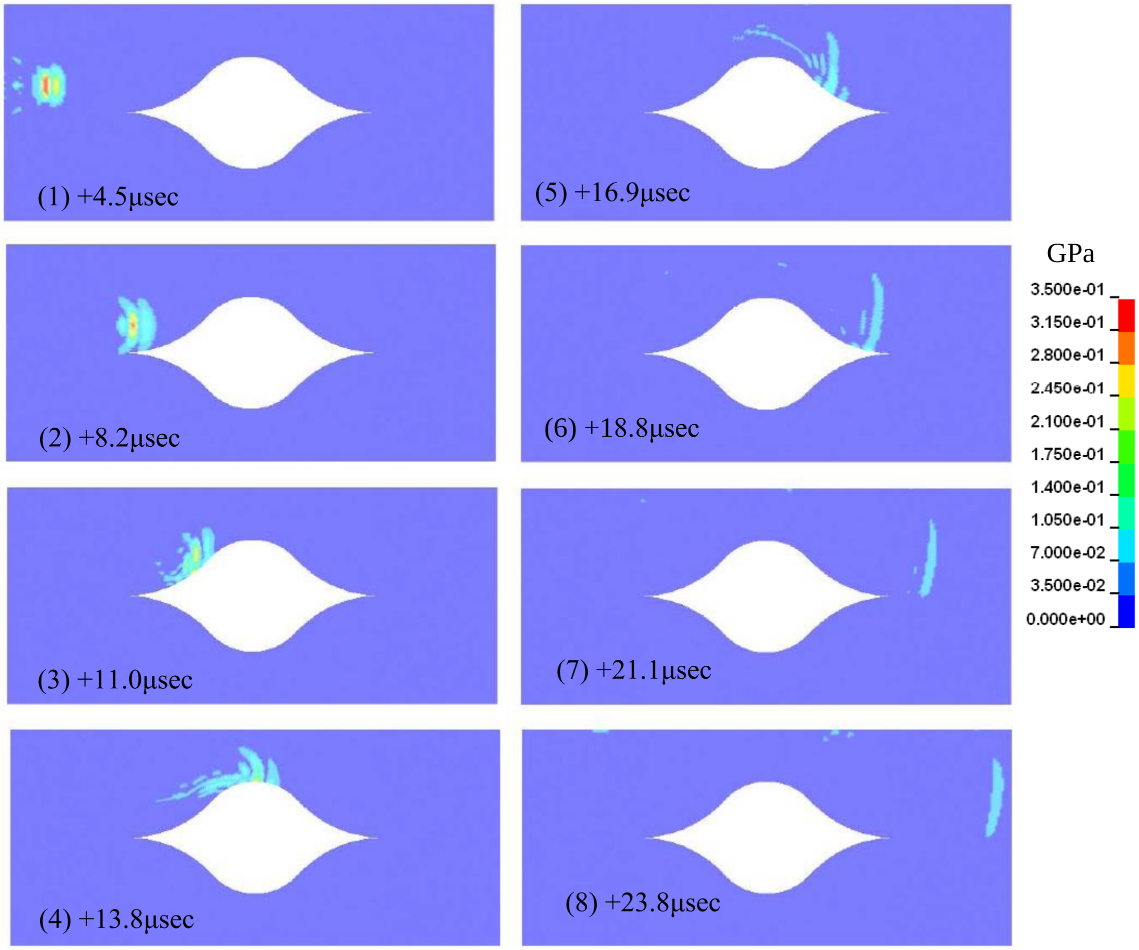

Figure 2.12: The von Mises stress contours from off-center numerical simulation of model B, plotted for a selected time sequence.

2.4. Acoustic Waves in Anisotropic Composites

We have fabricated transversely isotropic fiber-reinforced composites, using fiberglass-epoxy prepregs, to produce a macroscopically homogeneous solid with desired direction of the principal axis of anisotropy. This direction, which corresponds to the fiber orientation, is associated with the direction of the highest overall stiffness, and can be controlled by adjusting the orientation of the prepreg layups. In this manner we have designed and fabricated samples that clearly show how the overall anisotropy can be used to guide stress waves within a material that, at the scale of the wave length, is essentially homogeneous; even though microscopically (i.e., at smaller length-scales) it is highly heterogeneous. The main objective of this paper is to show this phenomenon experimentally, and qualitatively confirm the results by numerical simulations.

Figure 2.13 shows the micrograph of our fiberglass-epoxy composite. As is seen, the diameter of the glass fibers is less than 20μm, having less than 10μm spacing. The ultrasonic waves that we have used are in the low MHz frequency range. The minimum measured longitudinal and shear wave speeds in this composite are around 3000 and 1500m/s respectively. With these speeds, the corresponding wavelengths are about 3 and 1.5mm for 1MHz ultrasonic waves. Thus, for this kind of ultrasonic waves, the material is effectively homogeneous, yet highly anisotropic. In fact, in a fiberglass-epoxy composite, acoustic-wave redirection is possible for stress waves up to about 5MHz frequency.

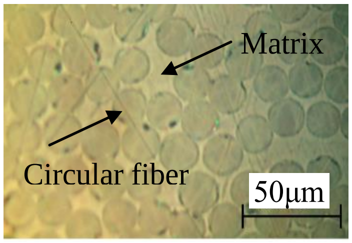

Figure 2.13: Optical micrograph of fiberglass-epoxy composite, cut normal to the unidirectional fibers; the fiber diameter is less than 20μm and the fiber spacing less than 10μm, hence to waves with 1 or more millimeter wave lengths, the material appears effectively homogeneous, yet anisotropic.

Based on available data, we have assumed Poisson ratios of $\nu_3 = 0.24$ and $\nu = 0.34$ for the fiberglass-epoxy composite, and calculated the other elastic moduli from the measured wave velocities: two longitudinal velocities, one in the x_3- and the other normal to this direction ($V_1 = 5310$ and $V_2 = 3150$m/s respectively); and one shear velocity in the x_1,x_3-plane with the x_1-polarization ($V_3 = 1735$m/s). Samples of different lengths were used for velocity measurements. These measurements verified that this composite behaves essentially as a transversely isotropic material with Young's moduli, $E_3 = 48.46$GPa and $E = 15.37$GPa, and the shear modulus, $\mu_3 = 5.47$GPa. The basic equations used to obtain these constants, are,

$$C_{33} = \rho V_1^2, \qquad C_{11} = \rho V_2^2, \qquad C_{44} = \rho V_3^2, \tag{2-11}$$

where density ρ is measured to be 1820kg/m^3, and C_{11}, C_{33}, and C_{44} are given in terms of the elastic moduli in Equation (6).

2.4.1. Sample Fabrication

Unidirectional composite plates of various thicknesses but a common glass volume fraction (49%) were fabricated and used to characterize the overall properties of the material. To experimentally verify wave redirection through elastic anisotropy that is suggested by the numerical simulations, we designed and fabricated a locally unidirectional fiber-reinforced composite sample of the geometry used for simulations; see Section 2.3, Figure 2.8b. An aluminum mold of the desired geometry was first fabricated (Figure 2.14a). Then unidirectional glass/epoxy prepreg sheets of suitable lengths were stacked on the mold in a pre-calculated sequence to ensure that the fiber content of the resulting composite sample would be essentially uniform throughout the sample; thus the fiberglass areal density would be uniform on any cross section taken normal to the fibers (i.e., normal to the sample's long axis).   Since the smallest thickness of the sample is half its greatest thickness, every other pregreg sheet was continuous while every other one consisted of two equal-length sheets, cut to a size to ensure the uniform glass-fiber density. Table 2.1 gives the length of 127 prepreg sheets in the layup. We used prepreg layers consisting of thin sheets of S-2 glass fibers impregnated with uniformly distributed epoxy matrix and then partially cured. They were then cut, placed in the mold, and processed as its final stage of curing. Before placement of the prepreg layers, the mold was covered with Teflon sheets. The mold with prepreg layers is then vacuum-bagged and pumped down to 10mmHg pressure. The layup was then placed in a 125ton Wabash laminating hot press, and subjected to a pressure of 0.35MPa while curing. The composite panels were processed in accordance with the manufacturer's recommendations. The curing was done using a 3°C/min heating rate up to a final temperature of 121°C. Then the sample was kept at this temperature for 1.5 hours. The setup remained in the hot press under pressure and cooled to room temperature [22]. The cured composite was taken out of the mold and the surfaces were machined to achieve smooth faces. The panel was then cut into top and bottom pieces which were then glued together with AeroMarine 300/21 Cylcoaliphatic epoxy. The fiber volume fraction of the composite material was measured to be %49, by ignition loss testing, in accordance with ASTM D 2584-02.

Figure 2.14a shows the mold, and Figure 2.14b the resulting composite after it has been hot-pressed, cooled, trimmed, and its surfaces machined. Then the composite was sectioned into three parts, two of these were glued together with epoxy to obtain sample B in Figure 2.14c, and the third part was cut and glued to obtain sample C of Figure 2.14d. The final sample B consists of two end segments with uniform preferred x_3-direction and middle sections with a gradually changing elastic anisotropy axis (the x_3-axis). This sample was used to investigate acoustic wave trajectories. In addition, sample C was used to measure the acoustic waves as they cross a plane normal to the fibers, half-way through the length of the sample. In this study, the geometry of the sample is particularly selected to illustrate the phenomenon of guiding elastic waves (with an angle of incidence normal to the sample boundary) around a region within an anisotropic (yet homogeneous) solid. The geometry of the curved molds is calculated and the molds are designed to provide a smooth change in the orientation of the anisotropy directions of the resulting samples, in order to accomplish this. As demonstrated in Figure 2.15, the mold surfaces consist of circular arcs and straight-line segments. This design can be machined with high precession, and is suitable for the hand lay-up composite fabrication. In general, it is possible to vary the shape of the internal (cloaked) region to a great extent, as long as the composite volume can be filled with a stack of properly cut prepreg layers without creating voids. The current design is chosen for geometric simplicity of alternating cut and uncut prepreg stacks. External surfaces of the molds are flat for ease of use with the hot press processing technique.

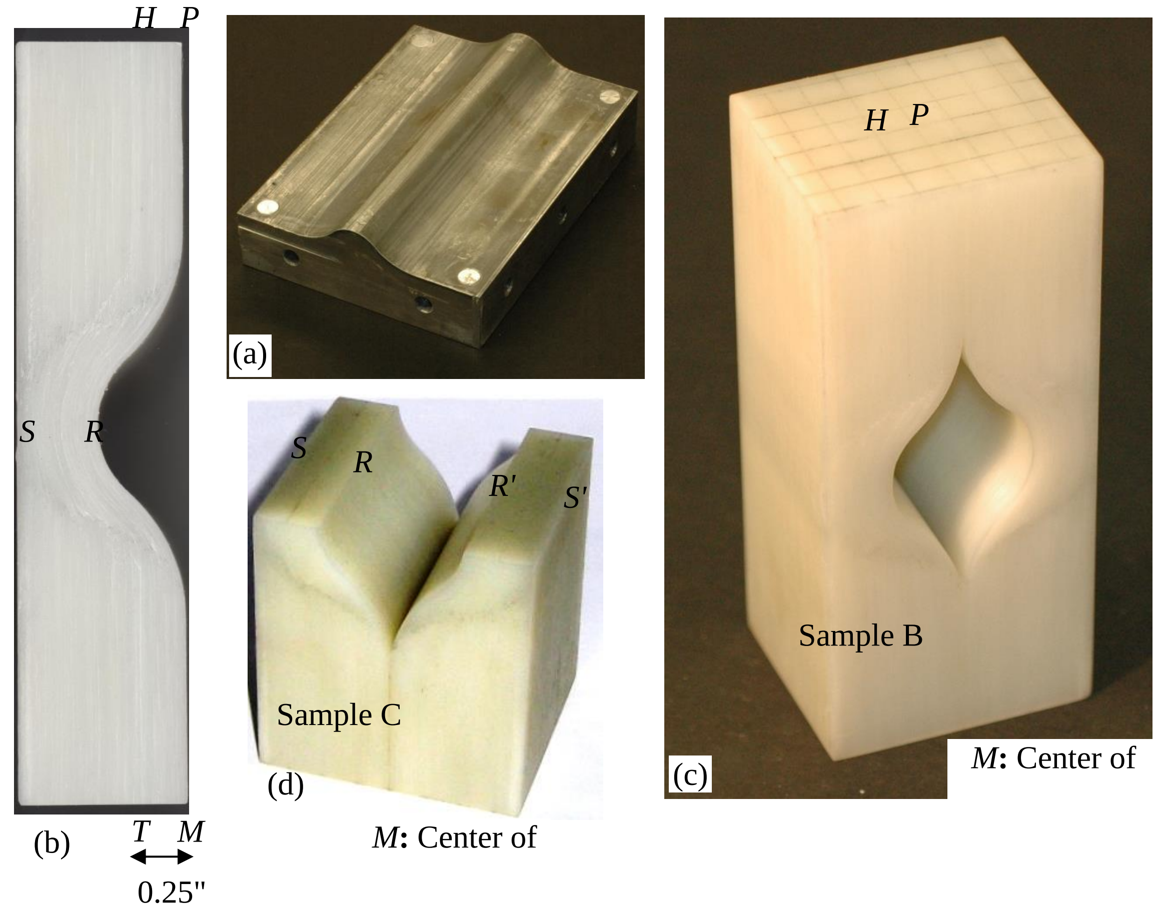

Figure 2.14: Sample fabrication (a) aluminum mold, (b) resulting composite after being hot-pressed, cooled, trimmed, and its surface machined, (c) sample B, (d) sample C.

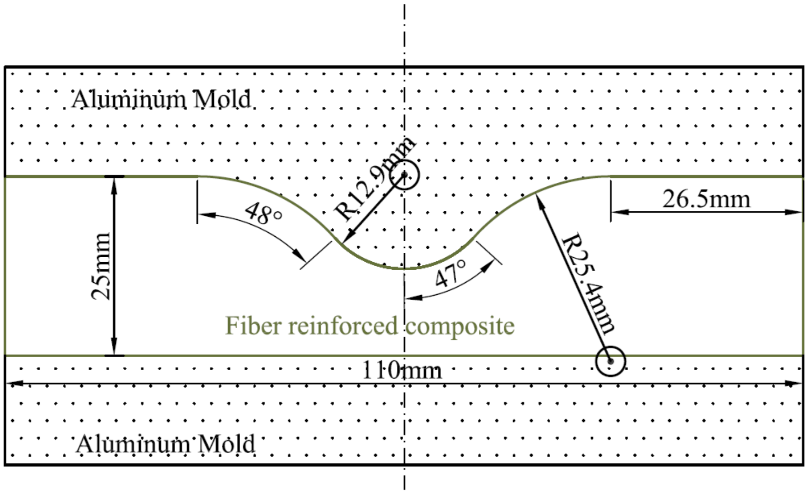

Figure 2.15: Geometry of the molds surrounding the composite material

Table 2.1: Length of prepreg sheets in layups in centimeters.

#	L	#	L	#	L	#	L	#	L	#	L	#	L
1	12.10	21	12.12	41	12.00	61	11.82	81	11.68	101	11.57	121	11.48
2	3.97	22	3.90	42	4.18	62	4.33	82	4.42	102	4.65	122	5.18
3	12.09	23	12.11	43	11.98	63	11.81	83	11.67	103	11.56	123	11.48
4	4.00	24	3.93	44	4.20	64	4.33	84	4.44	104	4.68	124	5.29
5	12.08	25	12.10	45	11.97	65	11.79	85	11.66	105	11.55	125	11.48
6	4.03	26	3.97	46	4.21	66	4.34	86	4.46	106	4.72	126	5.43
7	12.06	27	12.09	47	11.95	67	11.78	87	11.64	107	11.54	127	11.47
8	4.06	28	4.00	48	4.23	68	4.35	88	4.47	108	4.76		
9	12.05	29	12.08	49	11.93	69	11.76	89	11.63	109	11.53		
10	4.09	30	4.03	50	4.24	70	4.35	90	4.49	110	4.80		
11	12.04	31	12.06	51	11.91	71	11.75	91	11.62	111	11.52		
12	4.11	32	4.06	52	4.26	72	4.36	92	4.52	112	4.85		
13	12.03	33	12.05	53	11.90	73	11.74	93	11.61	113	11.51		
14	4.13	34	4.09	54	4.27	74	4.37	94	4.54	114	4.90		
15	12.01	35	12.04	55	11.88	75	11.72	95	11.60	115	11.50		
16	4.16	36	4.11	56	4.28	76	4.38	96	4.56	116	4.96		
17	12.00	37	12.03	57	11.86	77	11.71	97	11.59	117	11.50		
18	4.18	38	4.13	58	4.29	78	4.40	98	4.59	118	5.02		
19	11.98	39	12.01	59	11.84	79	11.70	99	11.58	119	11.49		
20	4.20	40	4.16	60	4.32	80	4.41	100	4.62	120	5.10		

2.4.2. Experiment

Olympus Panametrics-NDT ultrasonic transducers were used to send and receive the ultrasound-frequency stress waves through the samples. These transducers are based on piezoelectric or ferroelectric materials that can convert electrical signals to mechanical signals and vice versa. The transducers create a normal or tangential surface displacement, producing mostly longitudinal or polarized shear waves in the sample. The input signal is produced using a Matec TB1000 tone-burst generator card. The tone can be adjusted with 100Hz frequency resolution. The line is split and one line modulates the input transducer, while the other is reduced and sent to a digitizer for measurement. The output transducer signal is also sent to the digitizer. Olympus V103 transducers are optimized to modulate pulses around 1MHz frequency content. Low viscosity oil was applied to the interfaces of the transducers and the sample to facilitate the transmission of acoustic waves. The received signals were measured on a square reference-grid with 0.25" spacing to establish the propagation path of the stress waves within the composite; see Figure 2.14c, d. The receiving transducer was placed on the grid points and affixed to the sample. The incidence transducer was placed at a number of fixed points as described below. The amplitude of the received electrical signals was measured and compared to other measurements for the same placement of the incidence transducer. The electrical voltage pulse created in the transducer due to the mechanical oscillation at the interface was measured. Since the system is fully linear, the maximum voltage is proportional to the maximum particle velocity and maximum displacement. Comparison of the amplitude of the received signals demonstrates how the energy of the stress wave is transmitted to the opposite surface of the sample. The graphs shown in what follows are therefore drawn with arbitrary units.

2.4.2.1 Central excitation

In the first set of experiments, the actuating transducer is placed at point *M* (Figure 2.14c, d) on sample B or C. In each test, the receiver is placed at one of the grid points shown in Figure 2.14c, d, and the received signal is recorded. For each received electrical signal, the maximum instantaneous amplitude is found and normalized with respect to the amplitude of the incident pulse. The results are summarized in Figure 2.16.

Experimental results in Figure 2.16a demonstrate that the measured transmitted signal is maximum at the center of the opposite sample-face, in a small neighborhood of point *P*, although a straight line from this point to the actuating transducer passes through the central cavity of the sample. To better understand the wave propagation trajectory in the sample that produced the peak signal at *P*, we measured the transmitted signal on the opposite faces of sample C.

As Figure 2.16b shows, the maximum acoustic energy is measured in sample C around points denoted by *R* and *R′*, very close to the surface of the central cavity. Therefore, the stress wave travels essentially along a path defined by the axis of elastic anisotropy (maximum stiffness), in this transversely isotropic material. At the beginning of the path, the ultrasonic pulse travels along the fibers (which define the x_3-direction) in the locally unidirectional composite material. As the fiber orientation (and hence the x_3-direction) gradually changes, the stress pulse is redirected to travel along the material's preferred x_3-direction. The wave energy splits into two parts near the central cavity and travels along the surface of the cavity that coincides with the curved direction of highest stiffness (the x_3-direction). Traveling acoustic waves on the two sides of the opening then join together and finally follow the constant direction of anisotropy at the end, giving rise to a single peak at point P of sample B in Figure 2.16a, and two peaks in Figure 2.16b (at points denoted by R and R') in sample C.

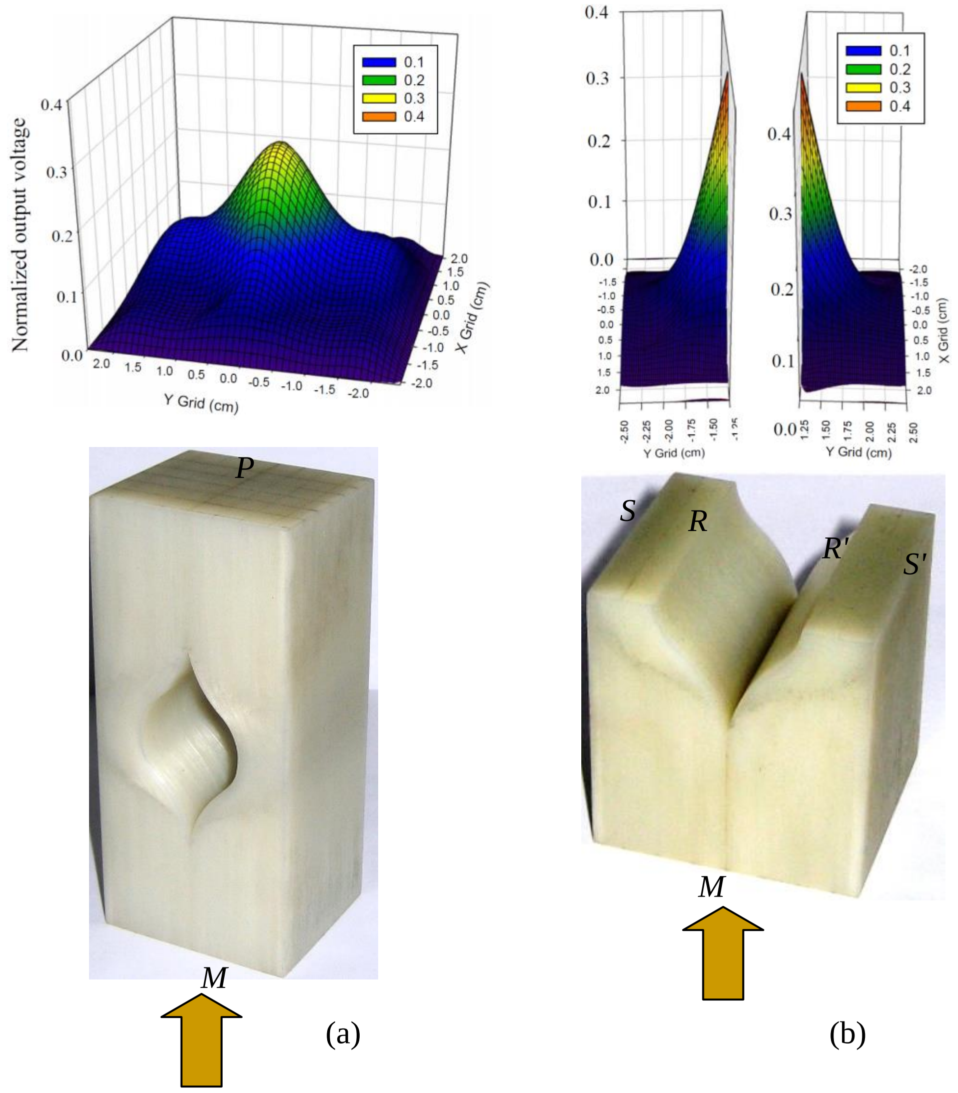

(a) (b)

Figure 2.16: Central excitation: maximum instantaneous amplitude of the received electrical signal, normalized with respect to the amplitude of the incident pulse in (a) sample B, and (b) sample C. The plots are drawn by interpolating the experimental data measured on a square reference-grid with 6.3mm spacing.

2.4.2.2 Off-center excitation

In the second set of experiments, the actuating transducer was shifted 0.25 inch from the center of the surface away from the hollow part (point *T*); see Figure 2.17. The maximum amplitudes of the received waves are normalized similar to the previous tests.

The result can be seen in Figure 2.17. The peak response is measured at 0.25 inch from the middle, exactly at the same point as excitation happens but on the opposite face (Point *H*), demonstrating that the acoustic wave trajectory in the material falls in the direction of highest stiffness.

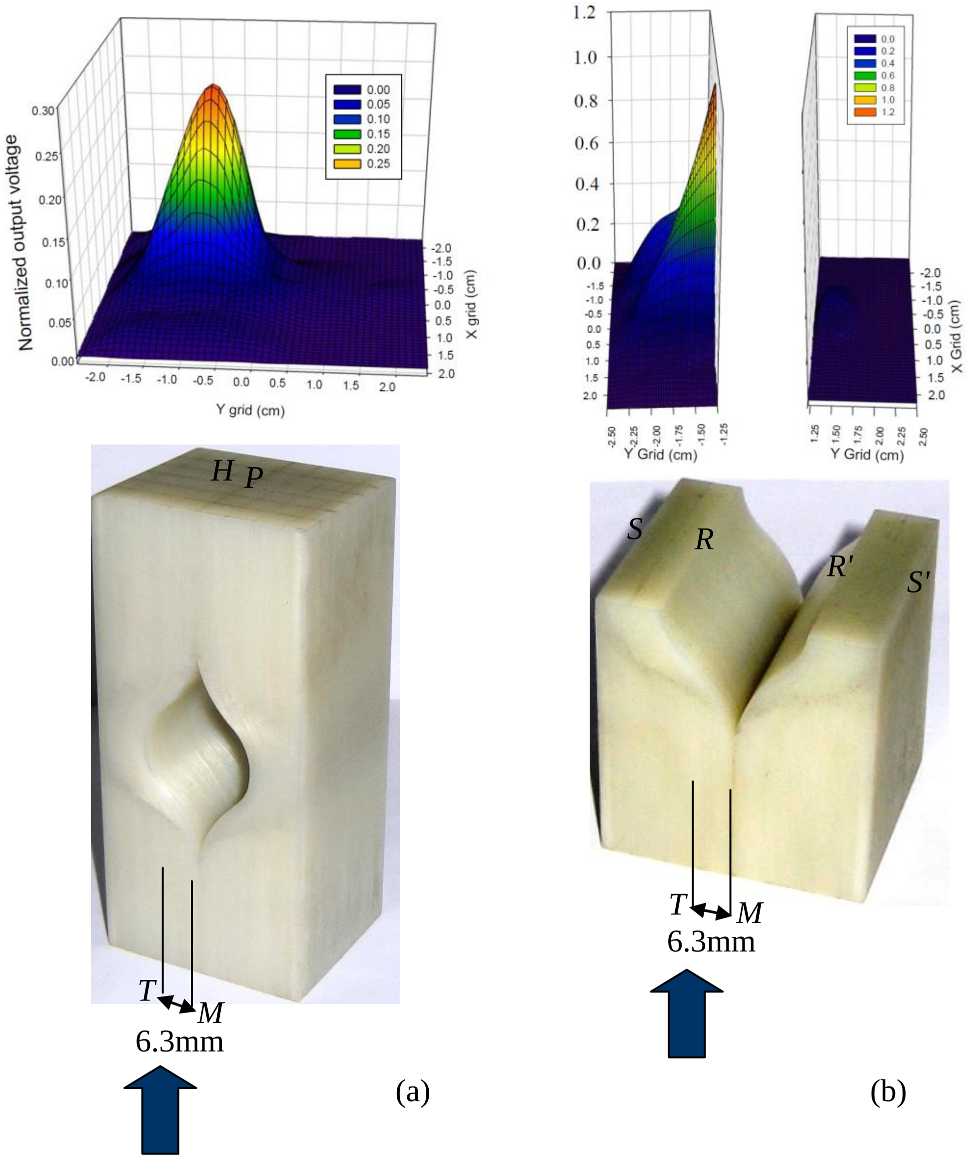

(a) (b)

Figure 2.17: Off-center excitation: maximum instantaneous amplitude of the received electrical signal, normalized with respect to the amplitude of the incident pulse in (a) sample B, and (b) sample C. The plots are drawn by interpolating the experimental data measured on a square reference-grid with 6.3mm spacing. Point *T* is 6.3mm away from the center of the lower face *M*. Note that different scales are used for the left- and right-plot.

The results of central and off-center excitation experiments shown here suggest that wherever on one face, normal to the axis of greatest stiffness of sample B, an acoustic wave is modulated, it will be mainly received at the same position on its opposing face. In other words, the curved free surface of the central cavity only minimally scatters the acoustic stress waves. The anisotropy of the composite redirects the incoming acoustic stress waves around the cavity and directs them towards the opposite face. Thus, controlling anisotropy of the material allows for management of acoustic stress-wave energy.

2.4.3. Fabrication and experiment on baseline model

Two baseline samples were fabricated by mimicking the geometry and anisotropy configuration of baseline model A proposed in section 2.3.2 (Figure 2.8a). Unidirectional composite sample is made by hot-pressing a prepreg layup in flat molds. The cured product is carved with a CNC mill to attain the same internal geometry of the cavity in model B as shown Figure 2.14a, and then cut into top and bottom pieces which were glued together to reproduce the same geometry as samples in Figure 2.14b, c. Theses samples make it possible to observe the geometrical effect of cavity on wave propagation in a unidirectional anisotropic material. The ultrasonic experiments are performed on these samples and the results are shown with solid triangles in Figure 2.10b, c. These data may be compared with experimental results on section 2.4.2.1 (solid squares in Figure 2.10b, c). It is seen that in the baseline model, the inside cavity scatters the incident stress-waves and only small disturbance is measured on the end faces; while the experiments on the sample with designed anisotropy shows that the incident stress-wave is guided around the cavity, and relatively large axial strains are measured on the faces.

2.5. Summary

In this work we have shown numerically and experimentally that managing the energy of stress-waves is possible by designing the preferred axis of a transversely isotropic material to vary smoothly with location. This controlled anisotropy is induced by a heterogeneous microstructure, however, when the wavelength of stress waves is long enough, the overall response is an effective homogeneous one. In transversely isotropic materials, when the wave vector deviates only slightly from the axis of maximum stiffness, almost all the energy of different modes of plane wave will travel along this axis. We have designed a specimen in which the anisotropy direction changes smoothly in order to split and redirect stress waves around a target object and then re-combine them on the opposite side of the object (referred to as “acoustic cloaking” in the literature). It is numerically shown and experimentally demonstrated that the acoustic wave energy packet would follow a similar gradual change as the axis of anisotropy.

A fiber-reinforced composite is fabricated to produce a macroscopically homogeneous solid, with fiber orientation creating the axis of maximum stiffness in the locally transversely isotropic material. We can design the heterogeneous microstructure of the specimen by adjusting the orientation of the prepreg layups. The purpose of the design is to redirect all the stress-waves with a given wave-vector direction around a cavity inside the specimen and deliver it on the opposite side of the cavity. It is shown that the cavity which may be filled with any desired material remains hidden to ultrasonic measurement tools and scatters stress waves minimally. The immediate application of such technology is to protect sensitive objects or facilities against undesirable acoustic disturbances.

2.6. Acknowledgments

Chapter 2 is a reprint of the material as it appears in Wave Motion 2010, 519-536, Amirkhizi A. V., Tehranian, A. and Nemat-Nasser, S., Elsevier, 2006. The authors would like to acknowledge the contributions of Mr. Jeffrey Irion for his great help in fabricating the samples, and Mr. Jon Isaacs for helping with the experimental setup of ultrasonic measurements. This work has been supported by ONR grant N00014-09-1-0547 and DARPA grant AFOSR FA9550-09-1-0709 to the University of California, San Diego.

2.7. References

[1] A. Greenleaf, M. Lassas, G. Uhlman, Anisotropic conductivities that cannot be detected by EIT, Physiol. Meas. 24 (2003) 413.

[2] A. Greenleaf, M. Lassas, G. Uhlman, On nonuniqueness for Calderon's inverse problem, Math. Res. Lett. 10 (2003) 685.

[3] J.B. Pendry, D. Schurig, D.R. Smith, Controlling electromagnetic fields, Science 312 (2006) 1780.

[4] U. Leonhardt, Optical conformal mapping, Science 312 (2006) 1777.

[5] D. Schurig, J.J.Mock, B.J. Justice, S.A. Cummer, J. Pendry, A. Starr,D.R. Smith,Metamaterial electromagnetic cloak atmicrowave frequencies, Science 314 (2006) 977.

[6] G.W. Milton, M. Briane, J.R. Willis, On cloaking for elasticity and physical equations with a transformation invariant form, New J. Phys. 8 (2006) 248.

[7] S.A. Cummer, D. Schurig, One path to acoustic cloaking, New J. Phys. 9 (2007) 45.

[8] H. Chen, C.T. Chan, Acoustic cloaking in three dimensions using acoustic metamaterials, Appl. Phys. Lett. 91 (2007) 183518.

[9] D. Torrent, J. Sanchez-Dehesa, Acoustic cloaking in two dimensions: a feasible approach, New J. Phys. 10 (2008) 063015.

[10] A.N. Norris, Acoustic cloaking theory, Proc. R. Soc. A 464 (2008) 2411–2434.

[11] A. Tehranian, A.V. Amirkhizi, J. Irion, J. Isaacs, S. Nemat-Nasser, Controlling acoustic-wave propagation through material anisotropy, Proceedings of SPIE, vol. 7295, SPIE, 2009 San Diego, CA, doi:10.1117/12.816053.

[12] R. Payton, Elastic Wave Propagation in Transversely Isotropic Media, Martinus Nijhoff publishers, The Netherlands, 1983.

[13] B.A. Auld, Acoustic Fields and Waves in Solids, John Wiley & Sons, New York, 1973.

[14] M.J.P. Musgrave, Crystal Acoustics, Holden-Day, San Francisco, CA, 1970.

[15] A.N. Norris, A theory of pulse propagation in anisotropic elastic solids, Wave Motion 9 (1987) 509–532.

[16] I.D. Abrahams, G.R. Wickham, Proc. R. Soc. Lond. A 436 (1992) 449–478.

[17] A.L. Mazzucato, L.V. Rachele, On transversely isotropic elastic media with ellipsoidal slowness surface, Math. Mech. Solids 13 (2008) 611–638.

[18] A.N. Norris, G.R. Wickham, Elastic waves in inhomogeneously oriented anisotropic materials, Wave Motion 33 (2001) 97–107.

[19] S. Nemat-Nasser, M. Hori, Micromechanics: Overall Properties of Heterogeneous Materials, Elsevier, The Netherlands, 1999.

[20] H. Kolsky, Stress Waves in Solids, Dover Publications, New York, 1963.

[21] LS-DYNA Keyword User's Manual, LSTC, Livermore, CA, 2007.

[22] Schaaf, K.L. (2008). Composite materials with integrated embedded sensing networks, Ph.D. dissertation, University of California San Diego, United States.

Chapter 3

Stress Wave Management at the Interface of Anisotropic Materials

The interface between two strongly anisotropic materials has a great influence on the stress wave scattering and can play a potential role in managing stress-waves in anisotropic and heterogeneous composites. Wave reflection and transmission at the interface of two elastic media has been thoroughly studied in the literature. In this study, we apply the theory of wave propagation to the interface of transversely isotropic materials, where the group velocity and wave-energy flow are usually close to the preferred direction of maximum stiffness. It is established that the anisotropy orientation of two interfacing materials can be exploited to control and manage stress wave energy by design; for example, the energy of an incident pressure wave can be guided to a desirable direction; the scattered longitudinal wave can be evanescent (non-propagating); and finally the energy content of stress-waves can be transferred from pressure into shear wave energy, which is prone to dissipation. It is important to note that wave scattering at the interface of *isotropic* materials is dictated by the density and elastic moduli of interfacing materials while strongly *anisotropic* materials provide several design parameters to achieve desirable stress wave control, including the anisotropy ratio and the direction of maximum or minimum stiffness.

3.1. Introduction

In recent years, there have been efforts to effectively control stress-wave propagation in solids by tailoring elastic anisotropy [1, 2]. Amirkhizi et al. [1] established the possibility of guiding the direction of stress-wave propagation through imposing gradually changing anisotropy direction in an essentially otherwise homogeneous material. The purpose of this study is to incorporate scattering of stress waves at the interface of anisotropic materials for guiding the direction of energy travel in the media, and also transferring pressure wave energy into shear wave energy.

Wave propagation in layered media is extensively studied in the literature. The early works by Ewing et al. [3] and Berkhovskikh [4] have significant contribution to this field. Layered media consisting of isotropic layers have been extensively studied by researchers. For example, the works by Thomson [5], Haskell [6], and Gilbert and Backus [7] develop transfer matrix method to solve the problem of wave propagation in arbitrary number of isotropic layers. Yamada and Nemat-Nasser[8] studied periodic layered orthotropic media, where the wave-vector direction makes an arbitrary angle with respect to the layers, by solving a twelfth order characteristic determinant. In their work, one axis of anisotropic material is restricted to be normal to the plane of the layers. This may be used to study wave propagation in earth's crust layers or in a conventional laminated composite structure where axes of anisotropy for each ply are rotated around the vector normal to the layers. Nayfeh [9, 10] studied the general multilayered anisotropic media, which provides the theoretical formulation necessary for the present work.

In the present paper, we will study the case where the preferred axes of the two transversely isotropic media and the normal to the interface are coplanar. Each axis may make an arbitrary specified angle with the normal to the interface. A few representative examples are then shown to demonstrate the potential of stress-wave energy management through scattering of impinging waves at the interface of properly designed anisotropic layers. It is established that the direction of energy travel in the media can be controlled by simply designing the orientation of anisotropy of interfacing media. Furthermore, as the scattered waves have different modes (pressure or shear) from that of incident wave, partial transfer of the energy from pressure mode into shear mode may be optimized. This can be integrated with a viscoelastic material which dissipates the energy of shear waves; thus enabling us to dissipate a significant portion of an incident stress-wave energy as a future application of the present study.

3.2. Theory and formulation

We consider two semi-infinite elastic media bonded together with a rigid interface, where the displacement and the traction are continuous. As shown in Figure 3.1, each media is transversely isotropic, where the axes of isotropy makes a specified angle (γ or β) with the vector normal to the interface plane (x_3) (the three axes are assumed coplanar). Incident plane wave propagating in originating medium (**A**) travels toward the interface with continuing medium (**B**), with the wave-vector making an angle θ with x_3. In order to satisfy the displacement and stress continuity at the interface, there will be plane waves reflected to the medium **A** and plane waves transmitted to the medium **B**. In this paper we present the solutions for amplitude and direction of propagation of these scattered waves, based on the established work by Nayfeh [10].

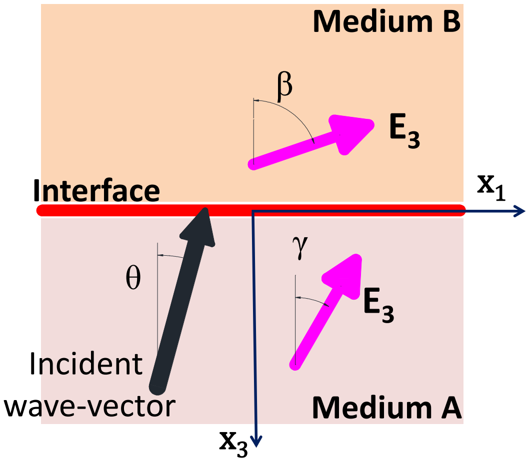

Figure 3.1: An incident plane wave propagating in originating medium **A** travels toward the interface of two transversely isotropic materials with specified axis of isotropies. The scattering at the interface results in reflected waves in medium **A** and transmitted waves in continuing medium **B**.

Nayfeh has formulated the stress wave propagation in general anisotropic materials and applied it to solve for the amplitude and direction of propagation of scattered waves at the interface of semi-infinite anisotropic media. Here, we consider transversely isotropic media (only 5 independent elastic moduli), and show how to effectively manage stress waves by designing the orientation of anisotropy of. The flux of the energy transmitted or reflected away from the interface is then calculated for longitudinal and shear waves. A computational platform using MATLAB is constructed to numerically solve the wave scattering at the interface based on the elastic moduli of interfacing medium and their orientation of anisotropies.

3.2.1. Wave propagation in a transversely isotropic material

The constitutive equation for a transversely isotropic material with axis of anisotropy along x_3 is given by equation (3-1) in terms of 5 independent elastic moduli.

$$\begin{bmatrix} \varepsilon_{11} \\ \varepsilon_{22} \\ \varepsilon_{33} \\ \gamma_{23} \\ \gamma_{13} \\ \gamma_{12} \end{bmatrix} = \begin{bmatrix} 1/E & -\nu_{21}/E & -\nu_{31}/E_3 & 0 & 0 & 0 \\ -\nu_{21}/E & 1/E & -\nu_{31}/E_3 & 0 & 0 & 0 \\ -\nu_{31}/E_3 & -\nu_{31}/E_3 & 1/E_3 & 0 & 0 & 0 \\ 0 & 0 & 0 & 1/\mu_{13} & 0 & 0 \\ 0 & 0 & 0 & 0 & 1/\mu_{13} & 0 \\ 0 & 0 & 0 & 0 & 0 & 2(1+\nu_{21})/E \end{bmatrix} \begin{bmatrix} \sigma_{11} \\ \sigma_{22} \\ \sigma_{33} \\ \sigma_{23} \\ \sigma_{13} \\ \sigma_{12} \end{bmatrix} \quad (3\text{-}1)$$

For a transversely isotropic material whose preferred axis (normal to the isotropic plane) makes an angle γ with x_3 axis as shown in Figure 3.1, the constitutive relationship can be written by rotating the material coordinate system around x_2:

$$\begin{bmatrix} \sigma_{11} \\ \sigma_{22} \\ \sigma_{33} \\ \sigma_{23} \\ \sigma_{13} \\ \sigma_{12} \end{bmatrix} = \begin{bmatrix} C_{11} & C_{12} & C_{13} & 0 & C_{15} & 0 \\ C_{12} & C_{22} & C_{23} & 0 & C_{25} & 0 \\ C_{13} & C_{23} & C_{33} & 0 & C_{35} & 0 \\ 0 & 0 & 0 & C_{44} & 0 & C_{46} \\ C_{15} & C_{25} & C_{35} & 0 & C_{55} & 0 \\ 0 & 0 & 0 & C_{46} & 0 & C_{66} \end{bmatrix} \begin{bmatrix} \varepsilon_{11} \\ \varepsilon_{22} \\ \varepsilon_{33} \\ \gamma_{23} \\ \gamma_{13} \\ \gamma_{12} \end{bmatrix} \quad (3\text{-}2)$$

where the specific form of each entry may be found easily [11, 12]. Now we consider a plane wave propagating in the x_1-x_3 plane where the motion is independent of x_2:

$u_j = U_j e^{i\xi(x_1 + \alpha x_3 - ct)}$ for $j = 1, 2, 3$. The components of the wave-vector in the x_1 and x_3 directions are ξ and αξ respectively; and c is the common phase velocity along the interface of the incident and associated scattered waves. The frequency and wavelength can be written as $\omega = \xi c$ and $\lambda = \frac{2\pi}{\xi\sqrt{1+\alpha^2}}$ respectively. The variables α and c, together, determine the direction of propagation and speed of each mode. This displacement formulation simplifies the analysis of reflection and transmission at the interface of two media by satisfying the pointwise compatibility at the interface plane $x_3 = 0$ regardless of the specific wave vector (α). Combining the equation of motion: $\frac{\partial \sigma_{ij}}{\partial x_j} = \rho \frac{\partial^2 u_i}{\partial t^2}$, constitutive equation, strain-displacement relation, and the displacement of a plane wave, we arrive at a simple matrix equation: $K_{ij}(\alpha)U_j = 0$, $(i, j = 1, 2, 3)$,where K is a 3x3 matrix whose elements depend only on the elastic moduli and α, and we have used the summation convention over repeated indices. The polarizations of the propagating waves in such medium, U_i, are the non-trivial solutions of this equation, which exist only when the determinant of the matrix K is zero. The matrix has a special simple form:

$$K = \begin{bmatrix} K_{11} & 0 & K_{13} \\ 0 & K_{22} & 0 \\ K_{13} & 0 & K_{33} \end{bmatrix} \tag{3-3}$$

Solving $K_{22} = 0$ gives two roots α_5 and α_6, which correspond to *pure anti-plane shear* mode. A positive α_q defines a plane wave with phase velocity in the $+x_3$ direction and a negative α_q defines a wave moving in the $-x_3$ direction. In a similar manner, solving $\left(K_{11}.K_{33}\text{-}K_{13}{}^{2}\right)=0$ gives four other roots α_q for q=1-4. Eigenvectors $\left(P_{1q}, P_{2q}, P_{3q}\right)$ for *quasi-longitudinal* and *quasi-shear* modes (in addition to the much simpler anti-plane shear, $P_{1q} = P_{3q} = 0$) can then be computed from this equation. We can rewrite the displacement and stress as the following superposition of the plane wave modes:

$$(u_1,u_2,u_3)=\sum_{q=1}^{6}\left(P_{1q}, P_{2q}, P_{3q}\right)U_q e^{i\xi\left(x_1+\alpha_q x_3\text{-}ct\right)}$$

$$(\sigma_{33}, \sigma_{13}, \sigma_{23})=\sum_{q=1}^{6} i\xi\left(D_{1q},\ D_{2q}, D_{3q}\right)U_q e^{i\xi(x_1+\alpha x_3\text{-}ct)} \tag{3-4}$$

Figure 3.2 demonstrates the solution to the eigenvalue problem for a given transversely isotropic material whose axis of anisotropy makes $\gamma=30^{\circ}$ angle clockwise with vertical axis x_3. The horizontal and vertical axes in Figure 3.2 show the inverse of phase velocity (i.e. slowness) along x_1 and x_3 axis respectively [13]. It can be seen that for a given c $(=\frac{\omega}{k_1})$, the ratios $\alpha_i=\frac{k_3}{k_1}$ are calculated. There are three modes of plane wave: quasi-longitudinal (α_1 and α_2), quasi-shear (α_3 and α_4) and pure shear (α_5 and α_6). It is important to note that if c becomes smaller than a critical value, there will not be a real solution for quasi-longitudinal mode. In other words α_1 and α_2 will be imaginary and the quasi-longitudinal mode will be non-propagating or evanescent, while there are still propagating solutions (real α) for quasi-shear and pure shear modes.

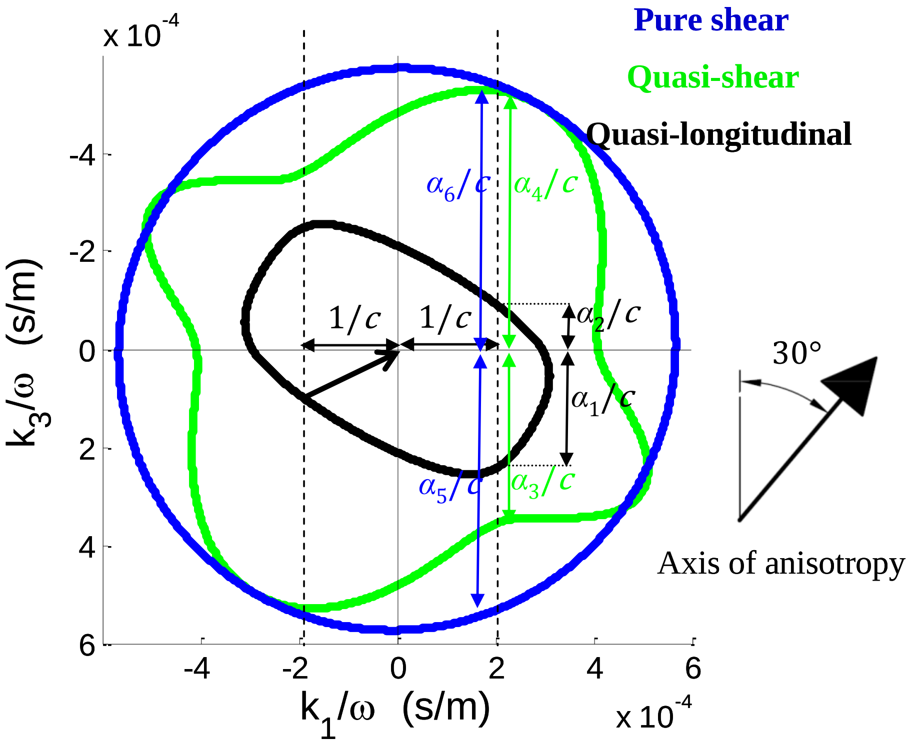

Figure 3.2: Slowness curves for a transversely isotropic material: E=15.37GPa, E_a=48.46GPa, ν=0.34, ν_a=0.24, μ_a=5.47GPa with an axis of isotropy making 30° angle with vertical axis x_3.

3.2.2. Scattering at the interface

Now consider an incident plane wave (I) travelling in an originating medium toward the interface with a continuing medium (Figure 3.1). Reflected (R) and transmitted plane waves (T) are produced in order to satisfy the boundary conditions at the interface:

Displacement continuity at the interface: $u_i^{(I)}+u_i^{(R)}=u_i^{(T)}$ for i=1, 2, 3 (3-5)

Traction continuity at the interface: $\sigma_{i3}^{(I)}+\sigma_{i3}^{(R)}=\sigma_{i3}^{(T)}$ for i=1, 2, 3 (3-6)

In order for scattered waves to satisfy boundary conditions, they should have the same phase velocity along the interface as the incident wave (Generalized Snell's law). The wave equations as defined in section 3.2.1 automatically satisfy this condition at $x_3=0$ and both the projected wave number (ξ) and phase velocity (c) along the boundary are the same for all scattered waves and the incident wave. This can be used to find the direction of propagation of each mode (α_q) as graphically shown in Figure 3.2. Since the slowness curves provide the relationship between the wave number and direction of propagation of a given mode, we draw a vertical dashed line in Figure 3.2 representing constant wave number along the interface, whose intersection with the curves for each corresponding mode gives α_q.

Now we write the displacement equations for incident, reflected, and transmitted waves:

Incident wave (I): $$(u_1,u_2,u_3)^I=\sum_{q=2,4,6}(P_{1q}{}^I,P_{2q}{}^I,P_{3q}{}^I)U_q{}^I e^{i\xi\alpha_q x_3}e^{i\xi(x_1-ct)} \tag{3-7}$$

Reflected wave (R): $$(u_1,u_2,u_3)^R=\sum_{q=1,3,5}(P_{1q}{}^R,P_{2q}{}^R,P_{3q}{}^R)U_q{}^R e^{i\xi\alpha_q x_3}e^{i\xi(x_1-ct)} \tag{3-8}$$

Transmitted wave (T): $$(u_1,u_2,u_3)^T=\sum_{q=2,4,6}(\overline{P}_{1q}{}^T,\overline{P}_{2q}{}^T,\overline{P}_{3q}{}^T)\overline{U}_q{}^T e^{i\xi\overline{\alpha}_q x_3}e^{i\xi(x_1-ct)} \tag{3-9}$$

Note that the over bars denote quantities in the continuing medium **B**. We have incorporated odd indices for α_q to refer to the incident wave and transmitted wave, which travel toward $-x_3$, and even indices to refer to the reflected waves, which travels along $+x_3$ coordinates. Rewriting 3 displacement and 3 stress continuity conditions in matrix form for the general case of incident wave, we have:

$$\begin{bmatrix} P_{11}{}^{R} & P_{13}{}^{R} & P_{15}{}^{R} & -\overline{P}_{12}{}^{T} & -\overline{P}_{14}{}^{T} & -\overline{P}_{16}{}^{T} \\ P_{21}{}^{R} & P_{23}{}^{R} & P_{25}{}^{R} & -\overline{P}_{22}{}^{T} & -\overline{P}_{24}{}^{T} & -\overline{P}_{26}{}^{T} \\ P_{31}{}^{R} & P_{33}{}^{R} & P_{35}{}^{R} & -\overline{P}_{32}{}^{T} & -\overline{P}_{34}{}^{T} & -\overline{P}_{36}{}^{T} \\ D_{11}{}^{R} & D_{13}{}^{R} & D_{15}{}^{R} & -\overline{D}_{12}{}^{T} & -\overline{D}_{14}{}^{T} & -\overline{D}_{16}{}^{T} \\ D_{21}{}^{R} & D_{23}{}^{R} & D_{25}{}^{R} & -\overline{D}_{22}{}^{T} & -\overline{D}_{24}{}^{T} & -\overline{D}_{26}{}^{T} \\ D_{31}{}^{R} & D_{33}{}^{R} & D_{35}{}^{R} & -\overline{D}_{32}{}^{T} & -\overline{D}_{34}{}^{T} & -\overline{D}_{36}{}^{T} \end{bmatrix} \begin{pmatrix} U_1{}^{R} \\ U_3{}^{R} \\ U_5{}^{R} \\ \overline{U}_2{}^{T} \\ \overline{U}_4{}^{T} \\ \overline{U}_6{}^{T} \end{pmatrix} = \begin{bmatrix} -P_{12}{}^{I} & -P_{14}{}^{I} & -P_{16}{}^{I} \\ -P_{22}{}^{I} & -P_{24}{}^{I} & -P_{26}{}^{I} \\ -P_{32}{}^{I} & -P_{34}{}^{I} & -P_{36}{}^{I} \\ -D_{12}{}^{I} & -D_{14}{}^{I} & -D_{16}{}^{I} \\ -D_{22}{}^{I} & -D_{24}{}^{I} & -D_{26}{}^{I} \\ -D_{32}{}^{I} & -D_{34}{}^{I} & -D_{36}{}^{I} \end{bmatrix} \begin{pmatrix} U_2{}^{I} \\ U_4{}^{I} \\ U_6{}^{I} \end{pmatrix} \tag{3-10}$$

The specific expressions for D (stress) components are long and may be found in [10]. We may consider special cases such as incident quasi-longitudinal wave: $U_4{}^{I}=U_6{}^{I}=0$; incident quasi-shear wave: $U_2{}^{I}=U_6{}^{I}=0$; or incident pure shear wave: $U_2{}^{I}=U_4{}^{I}=0$.

Solving the system of linear equation may result in propagating or evanescent (non-propagating) scattered waves. For evanescent modes, $u_{np}=U_{np}e^{i\xi(\alpha_{np}x_3+x_1-ct)}$, the parameter $\alpha_{np}=g\mathbf{i}$ becomes purely imaginary, whereas in the propagating modes $\alpha_p=f+0\mathbf{i}$ is real. The amplitudes $U_{np}=ae^{ib}$ and $U_p=me^{in}$ are both complex in general. Here f, g, a, b, m and n are real numbers.

The displacement field in a non-propagating mode $u_{np}=ae^{-\xi g x_3}e^{i\xi(x_1-ct)+ib}$ implies a surface wave which propagates along the interface (x_1) and its amplitude decays exponentially as it gets deeper in the medium (in either positive or negative x_3 direction).The displacement in the propagating scattered modes, $u_p=me^{i\xi(x_1+fx_3-ct)+in}$ demonstrates a finite shift in the phase angle.

3.2.3. Energy flux at the interface of anisotropic layers

In this section, we calculate the energy transferred or reflected away from the boundary of two anisotropic materials corresponding to each plane wave mode discussed above. Consider traction vector $\vec{t}$ at the interface of layers ($x_3=0$) and the vector $\vec{n}$ normal to the interface (Figure 3.3).

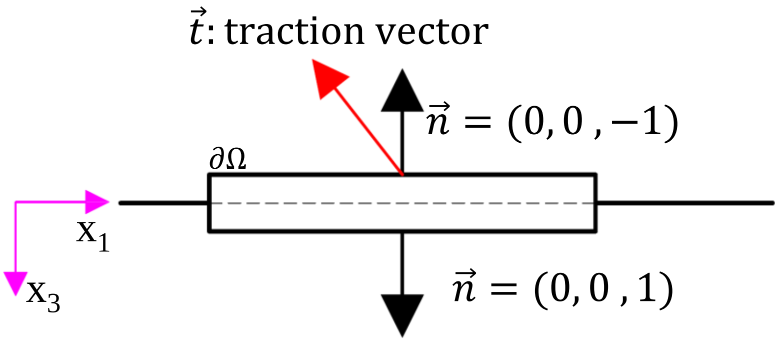

Figure 3.3: Traction vector acting at the interface of two anisotropic layers

The displacement, velocity and stress components may be written for a given mode q in the form of equation (3-4). The components of traction vector may then be derived: $t_j=n_i\sigma_{ij}$; and the energy flux per unit time is calculated for a given period T as

$$\text{Energy flux in a period T}=\int_0^T \int_{\partial\Omega} \mathrm{Re}(\vec{t})\mathrm{Re}(\vec{v})\, dA\ dt \qquad (3\text{-}11)$$

Therefore, the average energy flux per unit time (for incident or reflected wave) would be:

$$\text{Total flux} = \frac{-1}{2}\xi^2 c\left|U_q\right|^2 \text{Re}(D_{2q}\overline{P_{1q}}+D_{3q}\overline{P_{2q}}+D_{1q}\overline{P_{3q}})\ T \tag{3-12}$$

However, it is important to note that for evanescent mode (imaginary α_q), there will not be any energy transfer to the semi-infinite layer, and the energy flux for a non-propagating mode diminishes.

3.3. Numerical computation

A computational platform using MATLAB is developed to solve the system of linear equations (3-10) in order to find the amplitude and direction of wave energy flow of the transmitted and reflected waves in longitudinal and shear modes. The input parameters include material properties for the two media (density, and elastic constants), orientation of the preferred axis (Figure 3.1) corresponding to the two media (angles β and γ), and the incident wave vector direction (angle θ). The flux of the energy of transmitted and reflected stress-waves away from the interface is also calculated. The program is exploited to establish the significant role of interface discontinuity and elastic anisotropy in stress-wave management; i.e. redirecting stress-waves, transferring the energy of pressure wave into shear components, and trapping the energy of scattered longitudinal waves.

3.3.1. Redirecting the energy of stress-waves

In this section, we demonstrate redirection of an incident quasi-longitudinal plane wave at the interface of transversely isotropic materials, which have the same density and elastic moduli, but oriented differently with respect to each other. The concept is theoretically established and confirmed through finite element analysis using LS-DYNA.

Consider wave scattering at the interface of two transversely isotropic materials (Figure 3.1) with $\gamma=\theta=0°$ and variable β, where the incident quasi-longitudinal plane wave travels normal to the interface. The slowness curves for a glass fiber reinforced composite in Figure 3.4 show the inverse of phase velocity in a given direction of wave propagation with a wave vector in x_1-x_3 plane. Group velocity is defined as $V_g=\frac{\partial\omega}{\partial k}$ and indicates the direction of energy propagation, which is normal to the slowness curves [12, 13]. The dashed lines show the slowness curves for originating medium **A**, while the solid lines show the slowness curves for continuing medium **B**. Figure 3.5 shows the variation of the deflection angle of the energy of transmitted quasi-longitudinal waves (δ) as a function of anisotropy direction of the continuing medium (β). It is observed that the energy of stress-waves can be easily redirected and managed at the interface of anisotropic materials, since for most angles, the flux vector is essentially parallel to the preferred axis (of maximum stiffness) in the second medium. We have exploited this phenomenon in previous work for continuous redirection of stress waves [1].

Numerical simulation has been performed using LS-DYNA to investigate and confirm the wave propagation and scattering at the interface of anisotropic materials. As an example, a snapshot of pressure contours at a selected time after the start of simulation is shown in Figure 3.5b. Finite element calculations showed that the deflection of group velocity δ=23.4° for the case β=30° which is in very close agreement with the values found by the slowness curves method discussed above (Figure 3.5a).

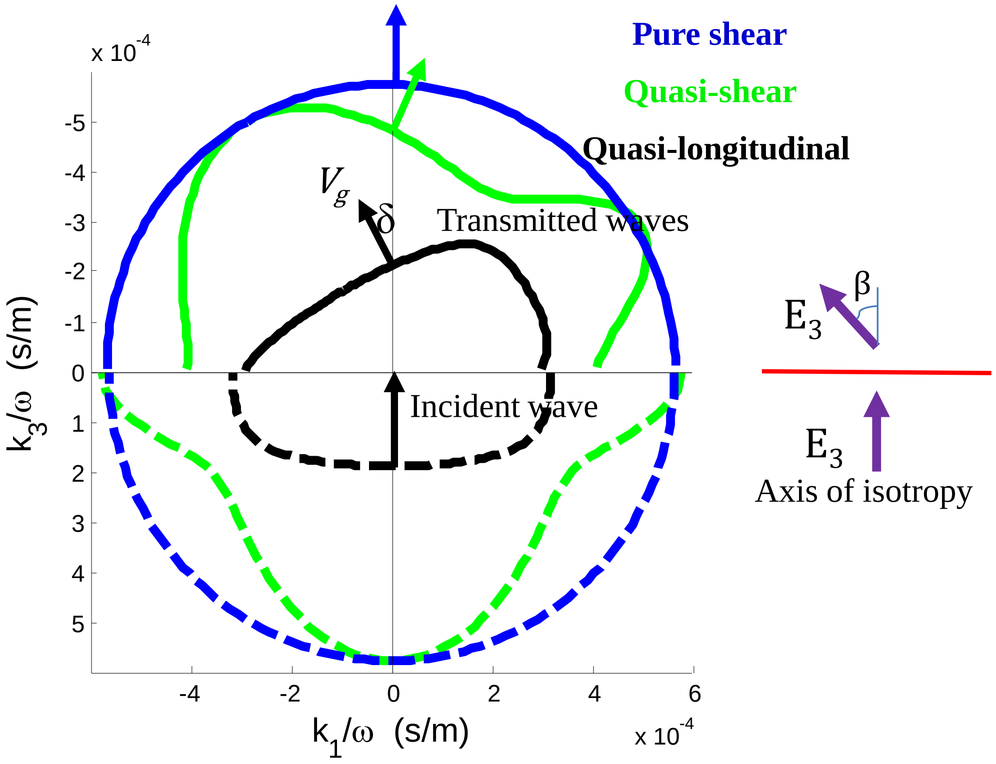

Figure 3.4: Computing the deflection of group velocity direction corresponding to a quasi-longitudinal plane wave (δ) at the interface of two transversely isotropic media with the same elastic moduli whose axes of highest stiffness make an angle β, and one of the material axes in one medium is normal to the interface.

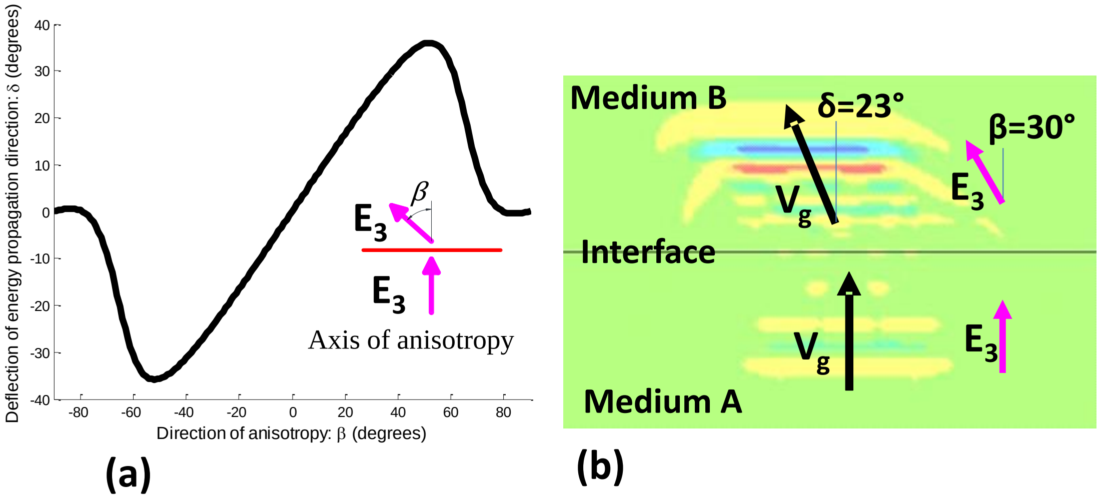

Figure 3.5: (a) Managing the direction of stress-waves energy propagation (δ) by changing anisotropy direction of the continuing medium (β). The plot is derived theoretically using the slowness curves shown in Figure 3.4; (b) Numerical computation using LS-DYNA confirms the theoretical result. As an example, a snapshot of pressure contours for β=30° is shown.

3.3.2. Transferring the energy of pressure waves into shear waves

The energy content of stress-waves can be transferred from pressure into shear at the interface of anisotropic materials. This transfer is desired since shear wave energy can be dissipated using viscoelastic materials.

Figure 3.6 shows an example of wave scattering at the interface of identical transversely isotropic materials with the specified orientation of local material axes. The formulation discussed in section 3.2 is implemented in a MATLAB program in order to find the flux of the energy of transmitted and reflected waves at the interface of identical transversely isotropic materials, for which the elastic moduli of a glass fiber reinforced composite were used. It is noted that a smart choice of anisotropy orientation results in transferring almost half of the pressure wave energy into shear wave energy. While the transfer of the energy in isotropic solids is dictated by the density and elastic modulus of the interfacing materials, directional materials provide a very versatile design parameter in order to control stress-wave scattering.

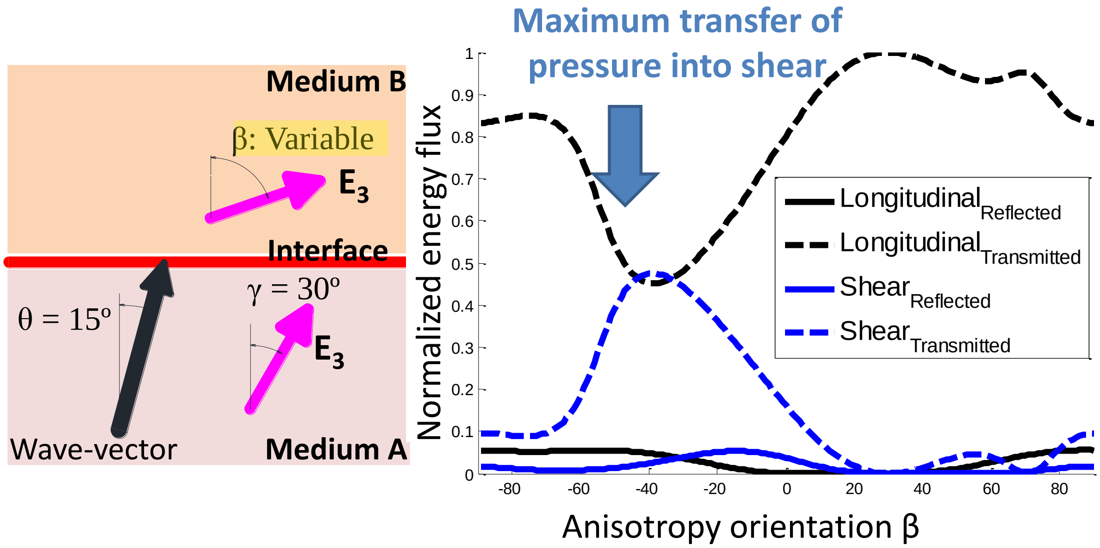

Figure 3.6: An incident pressure wave is propagating with an angle of θ = 15° with respect to the normal to the interface of two transversely isotropic materials with highest axis of anisotropy of γ = 30° in the incident medium and variable β in the continuing one. The energy fluxes of scattered wave (transmitted and reflected) in pressure and shear modes are plotted as functions of β of the second semi-infinite medium. It is observed that a significant portion of energy of impinging pressure wave is transferred into shear wave energy (up to 50%). The elastic moduli correspond to a glass fiber reinforced composite sample.

3.3.3. Evanescent mode of pressure wave and energy transfer into shear mode

It is well established in the literature [14] that dilatational waves may become evanescent (non-propagating) at the free boundary of isotropic materials or at the interface of isotropic materials, if the angle of incidence of impinging plane waves become greater than a critical angle. The critical angle is dictated by the dilatational and distortional wave speeds in the two interfacing isotropic materials. In this section, we exploit the expansion of this phenomenon to anisotropic media in order to control the stress-waves by trapping the energy of impinging pressure waves and transferring energy of impinging pressure waves into the reflected and refracted shear wave energy.

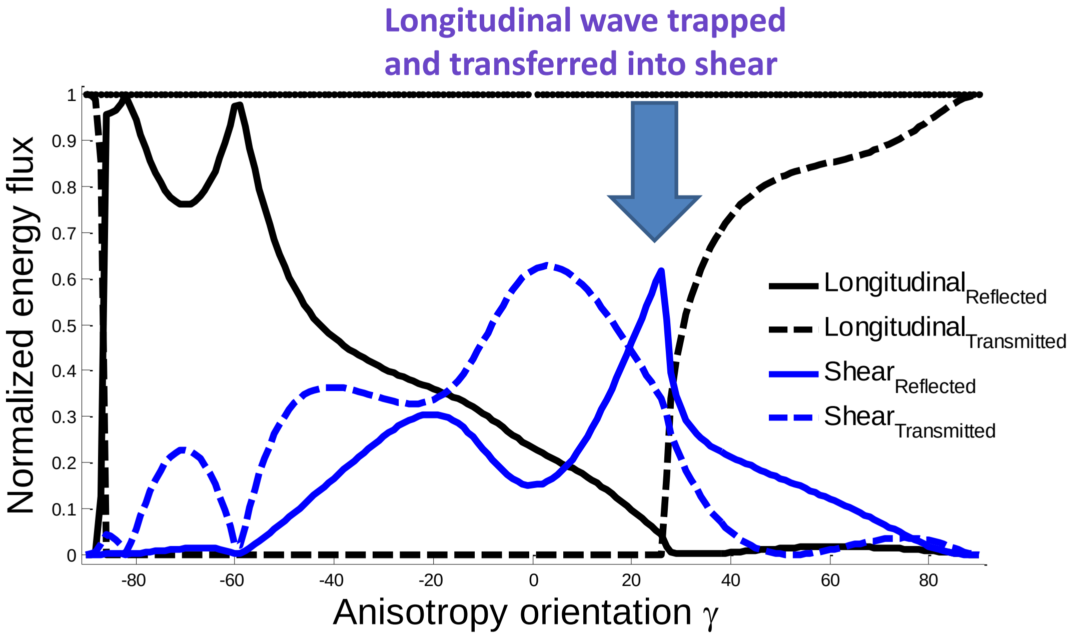

Figure 3.7: The energy flux of reflected and transmitted wave for longitudinal and shear modes are plotted for two identical transversely isotropic materials as in Figure 3.1 with θ=60°, β =90°, and variable γ. The effect of anisotropy of originating medium **A** is studied. It is observed that the transmitted longitudinal wave becomes evanescent and carries no energy where 0<γ<25° or 94°<γ<180°. Remarkably, at γ=26° the transmitted longitudinal mode is evanescent and the reflected longitudinal mode carries minimal amount of energy, while the scattered shear modes carry almost all of the energy. Therefore, longitudinal waves are trapped in the interface and the incident longitudinal wave energy is transferred into shear wave energy.

Figure 3.7 illustrates an example of stress-wave management by taking advantage of the total reflection of the longitudinal waves. The design of anisotropy orientation of interfacing materials is optimized to also minimize the reflected longitudinal wave; thus, transferring the energy of incident wave into scattered shear waves. This is of special interest, since the shear waves are prone to dissipation by viscoelasticity mechanism.

We have studied the sensitivity of the design suggested above, with respect to the incidence angle θ of the longitudinal plane wave. Figure 3.8 shows that the incidence angle is a governing factor while managing the energy of stress-waves. Given a fixed angle of incidence, we are able to design the anisotropy of interfacing layers in order to transfer almost all of the energy of longitudinal waves into shear waves, yet, the range of variation of angle of incidence is rather limited for the provided design.

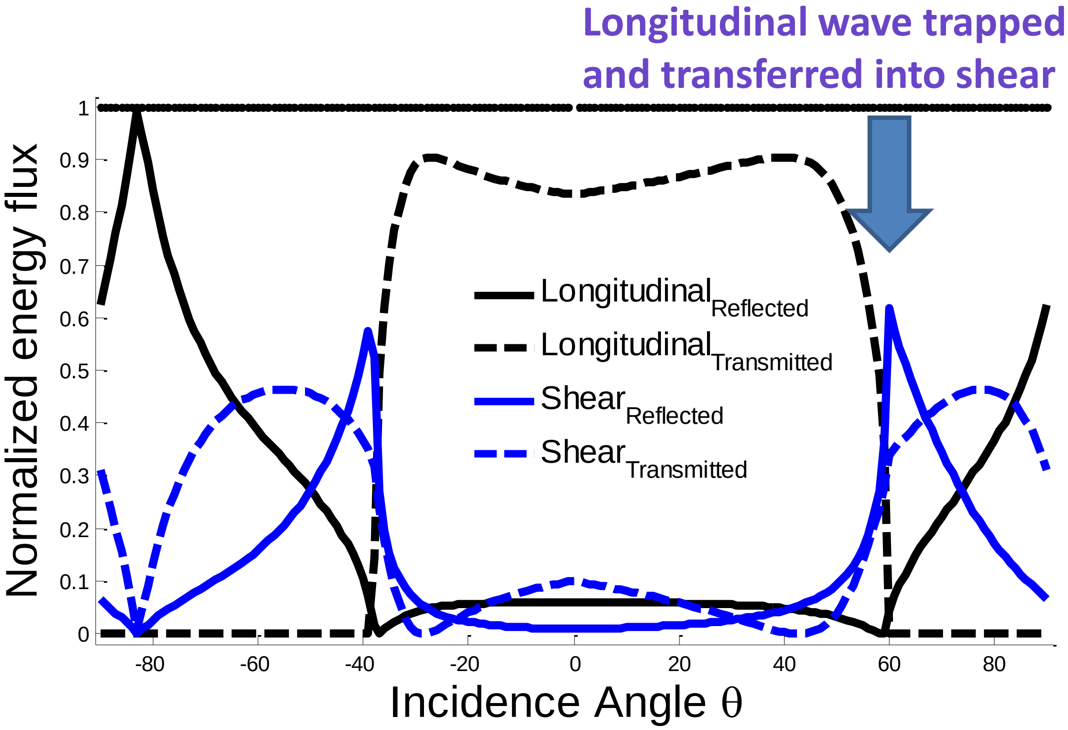
Longitudinal wave trapped and transferred into shear

Figure 3.8: The energy flux of scattered waves for two identical transversely isotropic materials as in Figure 3.1 with γ=26°, β =90°, and variable angle of incidence θ. The sensitivity of the highlighted design in Figure 3.7 is analyzed with respect to the incidence angle. It is observed that for 60°<θ<70° or 130°<θ<140°, the dominant energy carrying modes are scattered shear waves. The transmitted longitudinal mode is significant for the wide range of -40°<θ<60°; and for 70°<θ<130°, most of the impinging waves gets reflected at the interface. This analysis highlights the significance of incidence angle for stress-wave management at the interface of anisotropic media.

3.4. Wave scattering at Fluid-Solid interface

The wave reflection and transmission for plane waves, originated from the fluid onto the fluid-solid interface are studied. The fluids only support pressure wave propagation, while the general anisotropic solid supports propagation of quasi-longitudinal, quasi-shear and pure shear waves. The formulation is based on Nayfeh [10] notation and programmed in a MATLAB code. One of the applications of this study is to design a material that minimizes the reflection of an incident acoustic wave by providing an impedance matched properties with water. We would like to study the effect of incidence angle on the reflection of pressure wave off of the fluid-solid interface.

The displacement and stress in the fluid may be written as follows for the incident wave (and similarly for reflected wave) in the fluid:

$$(u_1,u_3,\sigma_{33})^I=(1,-\alpha_f,\mathbf{i}\xi\rho_f c^2)U^I e^{-i\xi\alpha_f x_3} \tag{3-13}$$

The continuity of normal displacement and stresses impose 4 equations for boundary conditions:

Normal displacement continuity at the interface: $u_3{}^{(I)}+u_3{}^{(R)}=u_3{}^{(T)}$

Traction continuity at the interface: $\sigma_{i3}{}^{(I)}+\sigma_{i3}{}^{(R)}=\sigma_{i3}{}^{(T)}$ for i=1, 2, 3 (3-14)

The linear system could then be solved to compute for the amplitude of the reflected pressure wave and 3 modes of transmitted wave:

$$\begin{bmatrix} \alpha_f & -\bar{P}_{32}{}^{T} & -\bar{P}_{34}{}^{T} & -\bar{P}_{36}{}^{T} \\ \rho_f c^2 & -\bar{D}_{12}{}^{T} & -\bar{D}_{14}{}^{T} & -\bar{D}_{16}{}^{T} \\ 0 & -\bar{D}_{22}{}^{T} & -\bar{D}_{24}{}^{T} & -\bar{D}_{26}{}^{T} \\ 0 & -\bar{D}_{32}{}^{T} & -\bar{D}_{34}{}^{T} & -\bar{D}_{36}{}^{T} \end{bmatrix} \begin{pmatrix} U^R \\ \bar{U}_2{}^{T} \\ \bar{U}_4{}^{T} \\ \bar{U}_6{}^{T} \end{pmatrix} = \begin{bmatrix} \alpha_f \\ -\rho_f c^2 \\ 0 \\ 0 \end{bmatrix} (U^I) \tag{3-15}$$

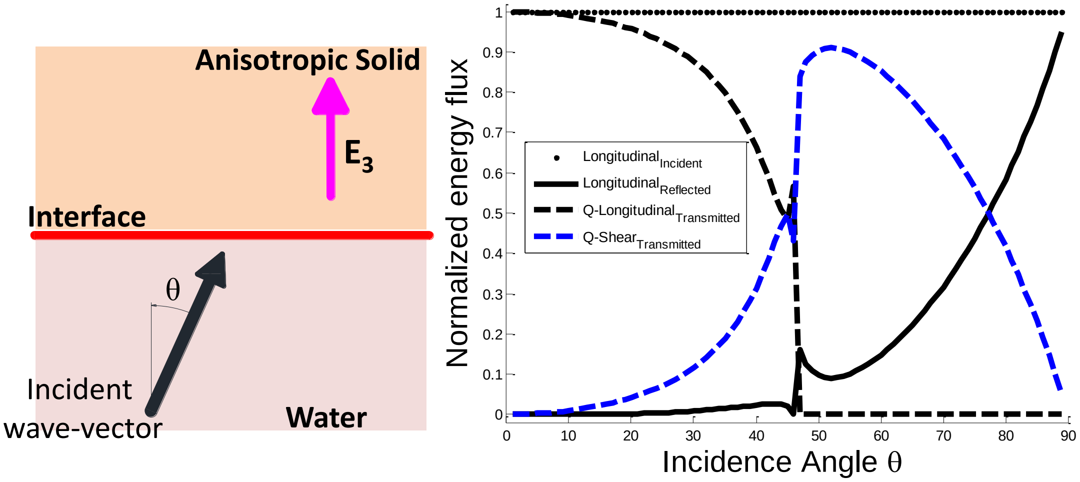

Figure 3.9: An incident pressure wave propagates with an angle of incidence θ with respect to the interface of a transversely isotropic material with a fluid (water). The energy fluxes of scattered wave (transmitted and reflected) in pressure and shear modes are plotted as functions of incidence angle (θ). It is observed that the energy of reflected longitudinal wave is minimized for a wide range of incidence angle (0°<θ<45°); however, for higher angles (45°<θ<90°), the transmitted quasi-longitudinal become evanescent, and gives rise to the energy of reflected longitudinal wave. The elastic moduli of the anisotropic solid is proportional to those of a glass fiber reinforced composite, and the density is adjusted so that the impedance of fluid and solid is matched at θ=0°.

Consider the fluid as water, where the longitudinal wave speed is $c_f=\sqrt{\frac{K_f}{\rho_f}}=1480\ \mathrm{m/s}$, interfacing with a transversely isotropic material which is impedance matched with water, when the incident wave travels normal to the interface (θ=0°); i.e. $\rho_f.c_f=\rho_s.c_s$. Figure 3.9 shows the energy of reflected and transmitted pressure and shear waves as functions of the angle of incidence θ. It is observed that the energy of reflected longitudinal wave is minimized for a wide range of incidence angle (0°<θ<45°);

however, for higher angles (45°<θ<90°), the transmitted quasi-longitudinal become evanescent, and gives rise to the energy of reflected longitudinal wave.

We also studied the wave scattering at the interface of an isotropic material with a fluid in order to seek a configuration that minimizes the reflected longitudinal wave for a wide range of incidence angle. The same formulation and computational platform stated for anisotropic materials is used and simplified for isotropic materials. Figure 3.10 shows an example that has successfully minimized the reflected longitudinal wave for a broad band of incidence angle.

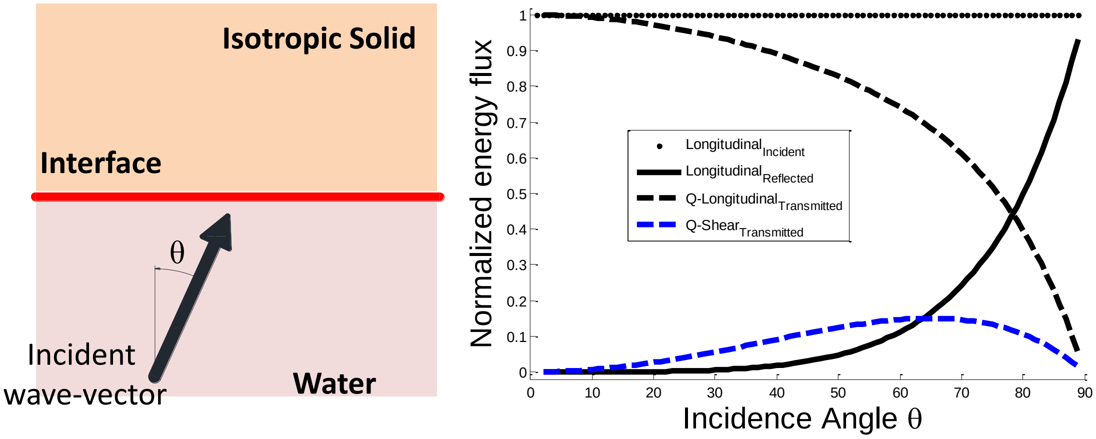

Figure 3.10: An incident pressure wave propagates with an angle of incidence θ with respect to the interface of water and an isotropic material (E=1 GPa, ν=0.3, ρ=1630 kg/m^3). The energy fluxes of scattered wave (transmitted and reflected) in pressure and shear modes are plotted as functions of incidence angle (θ). It is observed that the energy of reflected longitudinal wave is minimized for a wide range of incidence angle (0°<θ<50°); however, for higher angles (45°<θ<90°), the energy of reflected longitudinal wave becomes significant.

3.5. Summary

The scattering of an incident plane wave at the interface of two transversely isotropic materials is studied. Plane wave propagation in transversely isotropic media is decomposed to three supported modes: quasi-longitudinal, quasi-shear, and pure shear. The direction of propagation, amplitudes, phase velocity, group velocity, and energy flux of reflected and transmitted waves are computed by formulating the theoretical approach in a MATLAB based computational platform. It is shown that the direction of propagation of the energy in solids can be easily controlled by designing the orientation of anisotropy of interfacing materials, which may be used to redirect and guide the energy of stress-waves either away or toward a region within the material, depending on whether one wishes to avoid or harvest the corresponding stress waves.

The interface of anisotropic materials can be tailored in order to efficiently transfer the energy of pressure waves into shear wave energy, which is susceptible to dissipation. It is also established that a bi-layered structure can be designed to trap the pressure component of the reflected and refracted stress-waves and transfer it into shear components. We show that, while the transmitted and reflected shear waves are still present, the transmitted quasi-longitudinal wave can be rendered to be evanescent (non-propagating) and travel as a surface wave along the interface (not carrying any energy). The optimal choice of anisotropic properties of the interfacing layers can be selected in order to minimize reflected quasi-longitudinal wave energy. This traps the energy of the longitudinal component of the transmitted and reflected plane wave in the two-layer anisotropic material and transfer the energy of impinging longitudinal wave into shear wave energy.

3.6. Acknowledgements

Chapter 3 is prepared for publication by A. Tehranian, A. Amirkhizi, and S.Nemat-Nasser. This work has been supported by an ONR grant N00014-09-1-0547 to the University of California, San Diego. The dissertation author was the primary investigator of this paper.

3.7. References

[1] A.V. Amirkhizi, A. Tehranian, S. Nemat-Nasser, Stress-wave energy management through material anisotropy, Wave Motion (2010).

[2] A. Tehranian, A.V. Amirkhizi, J. Irion, J. Isaacs, S. Nemat-Nasser, Controlling acoustic-wave propagation through material anisotropy, Proceedings of SPIE, vol.7295, SPIE, 2009 San Diego, CA.

[3] W.M. Ewing, W.S. Jardetsky, F. Press, Elastic waves in layered media, McGraw Hill, New York, 1957.

[4] L.M. Brekhovskikh, Waves in layered media, Academic, New York, 1966.

[5] W.T. Thomson, Transmission of elastic waves through a stratified solid medium, J. Appl. Phys, 21, 89 (1950).

[6] N.A. Haskell, The dispersion of surface waves in multilayered media, Bull.Seosmol. Soc. Am., 43, 17 (1953).

[7] F. Gilbert, G.E. Backus, Propagator matrices in elastic wave and vibration problems, Geophysics 31 (1966) 326-332.

[8] M. Yamada, S. Nemat-Nasser, Harmonic waves with arbitrary propagation direction in layered orthotropic elastic composites, J. Composite Mater, 15 (1981) 531-542.

[9] A.H. Nayfeh, The general problem of elastic wave propagation in multilayered anisotropic media, J. Acoust. Soc. Am. 89 (1990) 1521-1531.

[10] A.H. Nayfeh, Wave propagation in layered anisotropic media, North Holland, 1995.

[11] S. Nemat-Nasser, M. Hori, Micromechanics: overall properties of heterogeneous materials, Elsevier, The Netherlands, 1999.

[12] J.D. Achenbach, Wave propagation in elastic solids, North Holland, New York, 1973.

[13] B.A. Auld, Acoustic fields and waves in solids, John Wiley & Sons, New York, 1973.

[14] H. Kolsky, Stress Waves in Solids, Dover Publications, New York, 1963.

Chapter 4

Controlling Stress Waves through multilayered anisotropic structure

Multilayered structures consisting of strongly anisotropic layers can be exploited to efficiently manage the stress wave propagation in solids by providing multiple interfaces that play key roles in transmission and reflection of pressure and shear waves. Anisotropic layers introduce various design parameters which can be optimized to control the impinging stress waves as desired. The configuration of layers may include inclination to add an extra design parameter of great potential, since it provides a deviation angle between the wave vector and the vector normal to the interface. We have developed a computational platform to efficiently evaluate the transmitted and reflected stress-waves in pressure and shear modes based on the anisotropy orientation of layers and the incident wave vector direction. We demonstrate that a multilayered structure can be tailored to effectively transform the energy of incident pressure wave into shear wave

energy. Furthermore, by integrating a layer of shear-dissipative material, the resulting shear-wave energy can be dissipated within the viscoelastic layer.

Keywords: Multilayered structure, anisotropy, stress wave, reflection, transmission.

4.1. Introduction

Wave propagation has been thoroughly studied in elastic media by Achenbach [1], Auld [2] and Musgrave [3] and also in layered structure by Ewing et al [4], Brekhovskikh [5], and Nayfeh [6-7] who formulated the wave scattering at the interface of general anisotropic materials. Recently, there have been efforts to control and redirect the stress-wave energy by smoothly changing the elastic anisotropy of the solid [8-9].

In the present study, we utilize wave propagation in layered media consisting of anisotropic elastic materials in order to manage the transmission and reflection of stress-wave energy in pressure and shear modes. The direction of propagation and the mode of stress-wave energy can be controlled at the interface of anisotropic layers. Particularly, it is extremely beneficial to transfer the energy of pressure wave into shear waves, since viscoelastic materials may be employed with the purpose of dissipating the shear waves as desired.

4.2. Numerical computation

We consider a representative three-layered anisotropic structure in order to illustrate the immense control of stress-wave scattering in pressure and shear modes. First, we present a 3-layered structure consisting of elastic anisotropic layers with no dissipation; and discuss how the energy of impinging pressure-waves can be redistributed among scattered quasi-longitudinal and quasi-shear modes. Next, we introduce a shear-dissipative layer into the multilayered structure and discuss its effectiveness in dissipating the energy of an initially pressure wave.

4.2.1. Elastic layered structure

In this subsection, we present a three-layered elastic structure consisting of identical anisotropic materials, which are strongly directional. (Figure 4.1) The orientation of material axes for layers A and C are fixed, while the orientation of the axis of highest stiffness in the middle layer B is selected as a design variable (angle α). We aim to investigate the effect of anisotropy of one layer on the reflection and transmission of an incident longitudinal wave impinging on the surface of the multilayered structure (side PQ, centered at point R). It is important to note that an inclined interface between the layers is chosen to provide the capacity for scattering of a longitudinal wave in both longitudinal and shear modes. This is possible due to the angle β between the wave vector and the vector normal to the interface. However it is chosen to be relatively small to reduce the thickness of the multilayered structure. (β=15°)

The strong directionality of constituent layers plays a key role in managing wave propagation in the proposed layered structure. Among industrial composites, unidirectional Carbon fiber reinforced plastic (CFRP) offers the strongest directionality of elastic stiffness. Therefore, the elastic moduli used in the numerical computation mimics samples of unidirectional CFRP, fabricated to verify the predictions experimentally. The 5 independent elastic moduli of the transversely isotropic material are as follows: E_3=72.4GPa, E_1= E_2=5.8GPa, G_{13}=6.0GPa, G_{12}=2.1GPa, and ν_{12}=0.3875. The material preparation and experiments are further discussed in section 4.4.

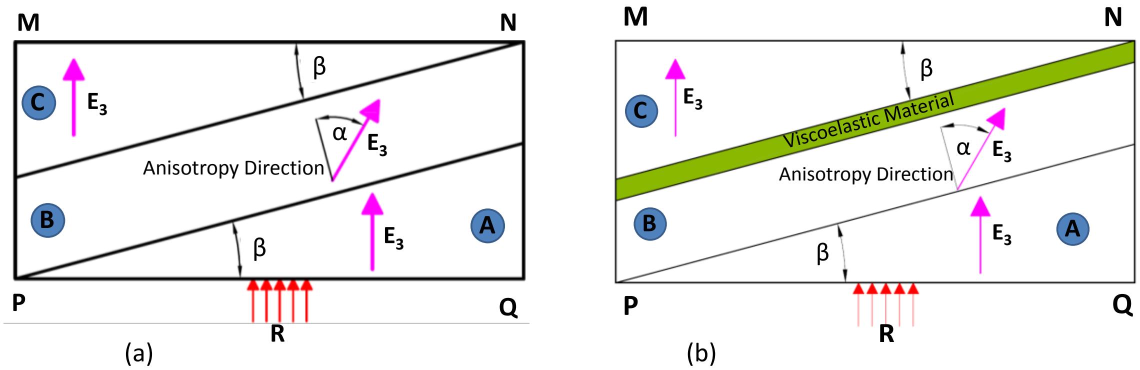

(a)

(b)

Figure 4.1: (a) Elastic 3-layered structure composed of transversely isotropic materials with preferred axis E_3, (b) integrated multilayered anisotropic structure with a layer of viscoelastic material to dissipate shear wave energy. While the axis of highest stiffness (E_3) is fixed for layer A and C, the orientation of anisotropy of middle layer B is defined by variable angle α. We show that by changing α, we can control the wave-scattering in the multilayered structure as desired. We have chosen wedge angle β=15° to introduce a small deviation between the wave-vector and the vector normal to the layers' interfaces. Dimensions are as follows MN=100mm; NP=46.6mm, and the depth of the model is 12mm out of the plane shown.

A series of numerical simulation has been carried out using LS-DYNA to find the effect of anisotropy orientation of the middle layer (α) on the quasi-longitudinal and quasi-shear waves that are transmitted to the opposite face (MN) or reflected back to the originating face (PQ). For any $\alpha \in \{0, \pm 15, \pm 30, \pm 45, \pm 60, \pm 75, 90\}$, an input file is generated reflecting the elastic moduli of the middle layer B, and the solution using finite element analysis is derived, and the results are post-processed individually using LS-PrePost. A MATLAB code was developed to automate the complete process and compare the results.

The boundary condition on the surfaces of the block in Figure 4.1 is stress-free, except for the excited area around R, where a single sinusoidal pulse of load is applied with 1μsec period. The amplitude of the pulse is 10N. The interfaces between the layers are considered rigid, which results in continuity of displacement and stress.

Each numerical simulation for a given α provides the data for the displacement in X and Y directions for the elements located on the top and bottom of the block in Figure 4.1. As an example, for $\alpha=0$, the histogram of the displacement in Y-direction for an element located in the middle of the top surface MN is shown in Figure 4.2. Likewise, the histogram of all other elements located on the surface MN is considered and the signal peak is recorded. We now plot these peaks versus the location of each element in the top surface in Figure 4.3.

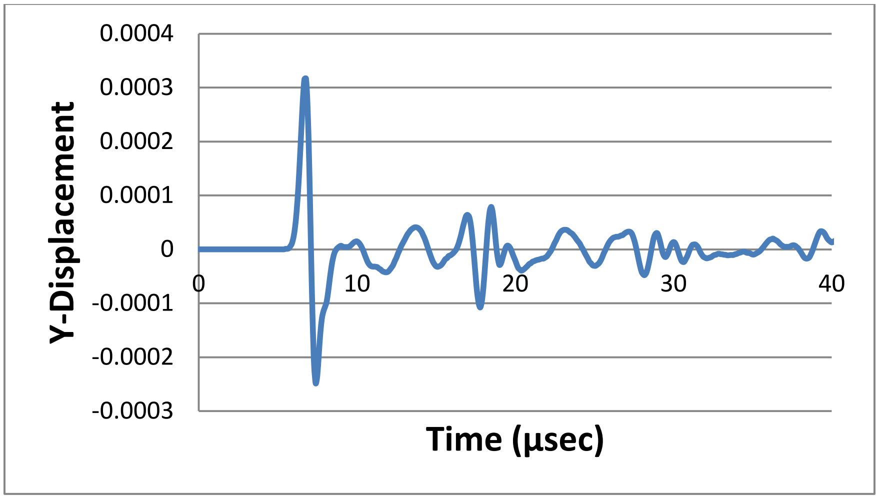

Figure 4.2: Histogram of the signal received in an element located in the middle of top surface MN.

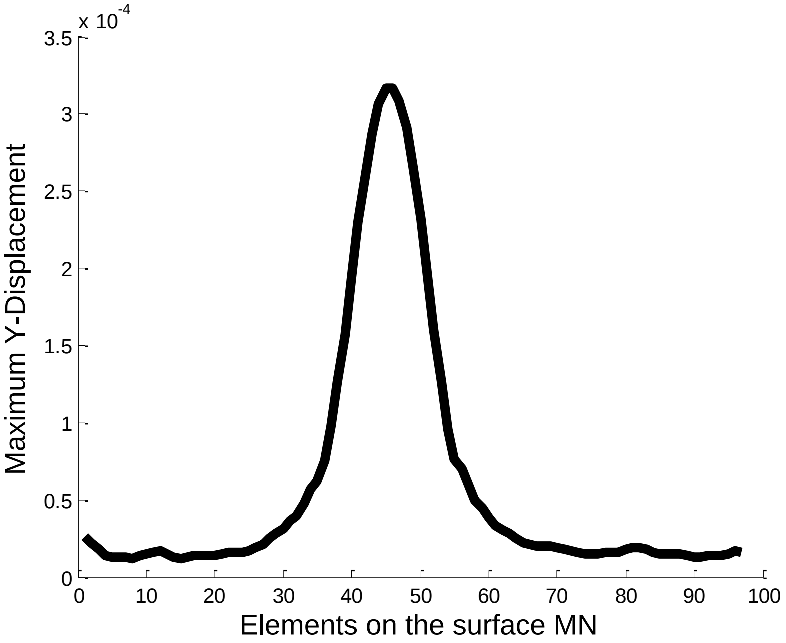

Figure 4.3: The histogram of the signals received at any elements located on the top surface MN is considered and then, the signal peaks are computed. The peaks are plotted versus the element number, where element 1 corresponds to the leftmost element at M, and element 97 corresponds to the rightmost element at N.

The final outcome of the numerical simulation results for α =0 is the maximum peak observed in Figure 4.3, since we are interested in the highest peak of the received signal transmitted through the block (shown in Figure 4.1a). We use this data as an indicator of the transmission of an incident pulse for a given anisotropy angle α. A MATLAB program has been developed to process the simulation results to find the indicators of transmitted and reflected signal for all 12 choice of α ∈{0, ±15, ±30, ±45, ±60, ±75, 90}. The effect of the anisotropy of the middle layer B on the transmission of the incident wave is shown in Figure 4.4.

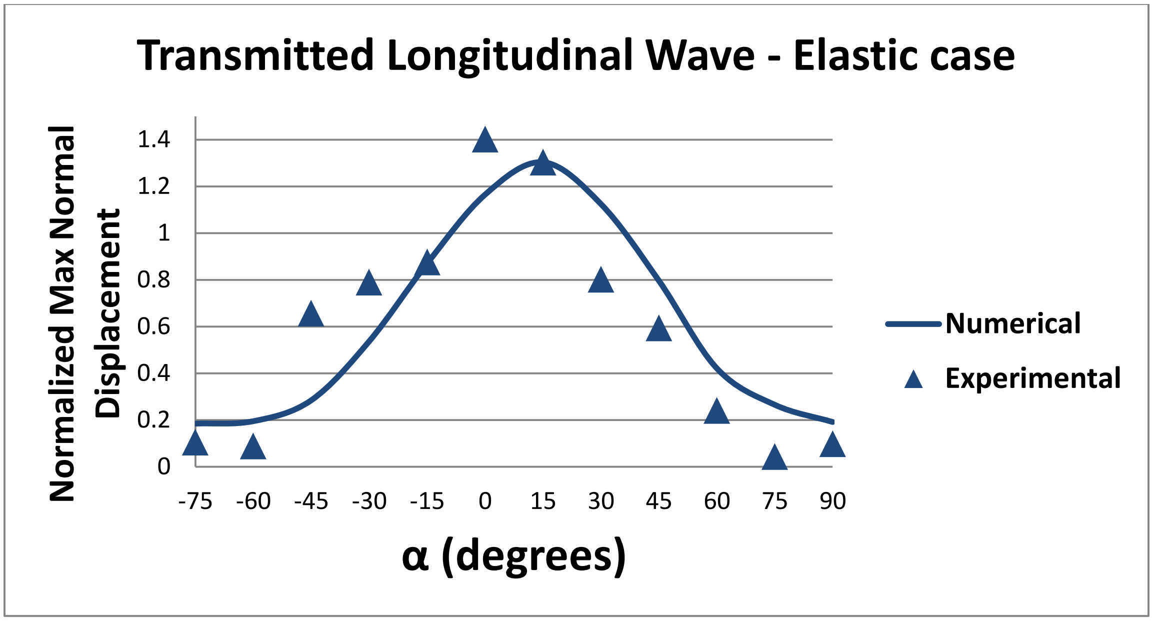

Figure 4.4: Transmission of longitudinal wave through the block of elastic multilayered structure shown in Figure 4.1a as received in MN.

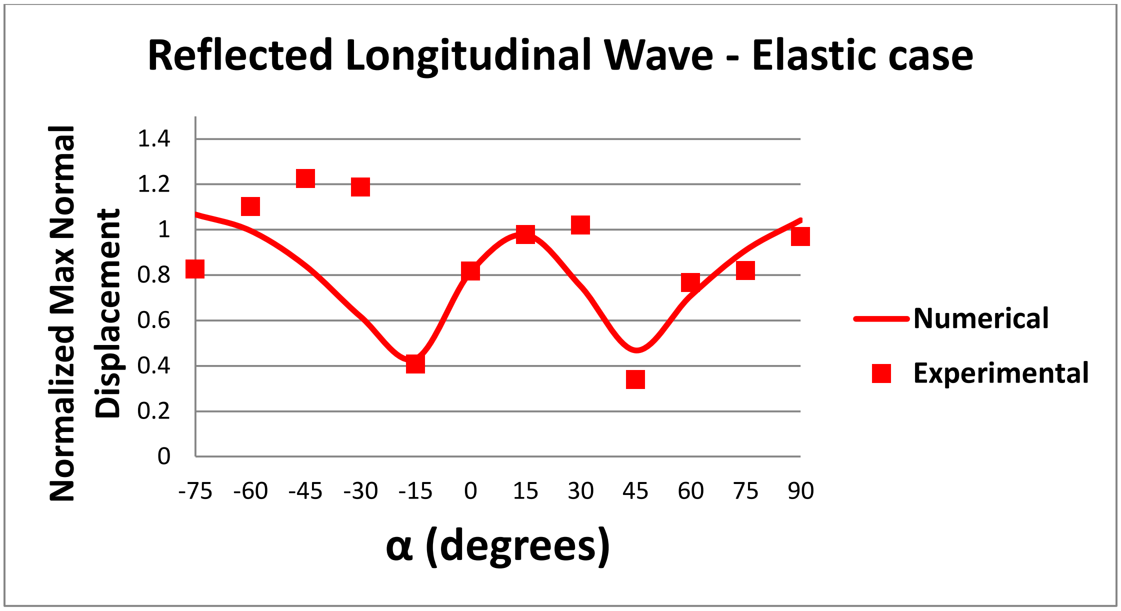

Figure 4.5: Longitudinal wave reflected back from the block of elastic multilayered structure shown in Figure 4.1a as received in PQ.

In order to examine the propagation of an incident pressure wave in the multilayered structure, we have studied the stress-waves reflected back to the originating side PQ of Figure 4.1 in addition to the transmitted wave through the layers at the opposite side MN. The protocol to compute the indicators of reflection wave for any configuration of middle layer's anisotropy is similar to that of transmitted wave. We consider the peaks of signals received at any element located on PQ and find their maximum. The indicators of reflected waves are plotted for any given angle of anisotropy α in Figure 4.5.

The objective of designing a multilayered anisotropic structure with inclined interfaces, as discussed in the introduction section, is to redistribute the energy of incident pressure wave among scattered longitudinal and shear waves. Therefore, we need to account for the transmitted and reflected shear waves. While we have studied the displacement in the Y-direction (normal displacement) as an indicator of longitudinal waves, we consider the transverse displacement in the X-direction as an indicator of shear waves. Similar to the computation of longitudinal waves, the maximum peaks of transverse displacement are plotted for transmitted waves in Figure 4.6 and reflected waves in Figure 4.7.

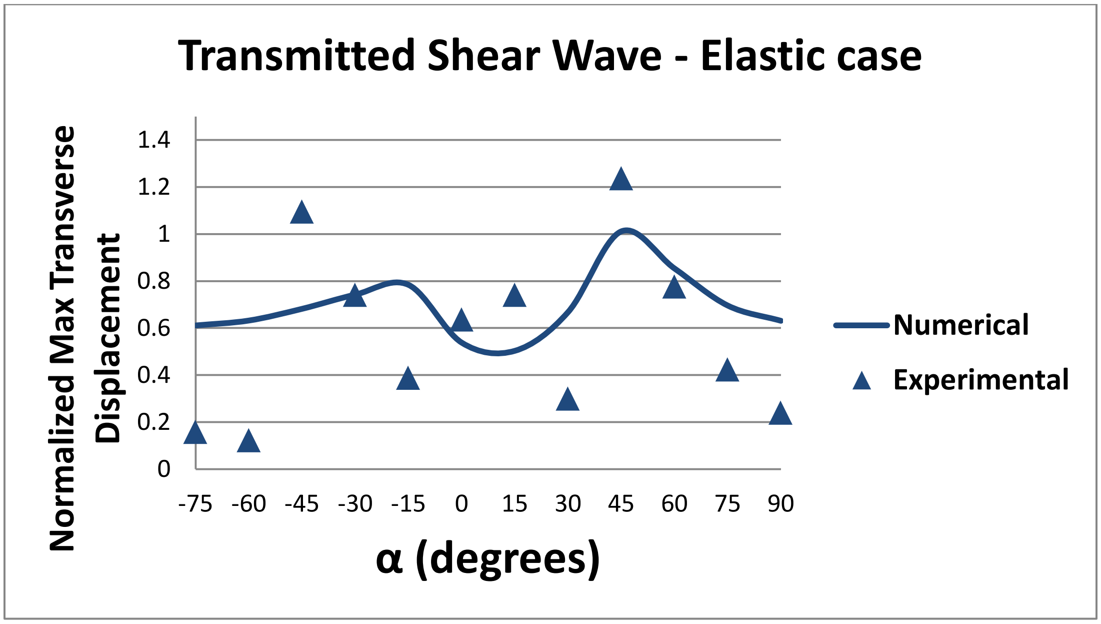

Figure 4.6: Transmission of shear wave through the block of elastic multilayered structure shown in Figure 4.1a as received in MN.

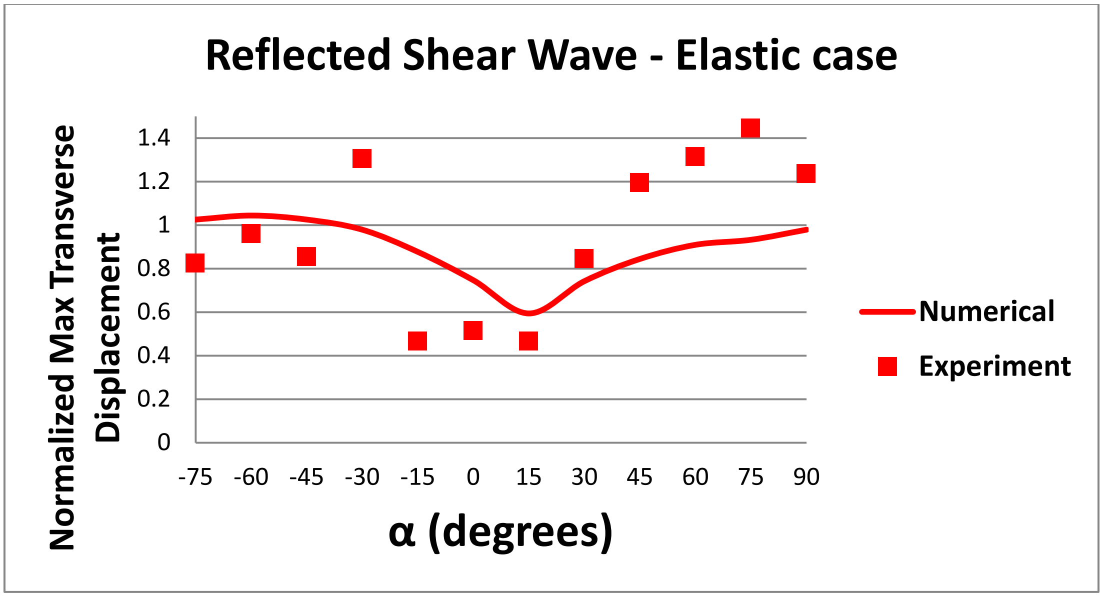

Figure 4.7: Shear wave reflected back from the block of elastic multilayered structure shown in Figure 4.1a as received in PQ.

4.2.2. Dissipative layered structure

In this subsection, we introduce a shear dissipative material into the multilayered structure discussed in section 4.2.1, in order to study the attenuation of scattered longitudinal and shear waves. The purpose is to transfer a portion of the energy of incident pressure wave into scattered shear waves, which will then be attenuated in a shear dissipative layer. The viscoelastic properties of this layer are as following: density: ρ=1.1 g/cm^3, bulk modulus: K=5GPa, short time shear modulus: G_0=0.2GPa, long time (infinite) shear modulus: G_∞=0.4GPa, and decay constant β=0.4µsec. The dashed line in Figure 4.8 shows the transmitted longitudinal wave; Figure 4.9 shows the reflected longitudinal wave; Figure 4.10 shows the transmitted shear wave, and finally, Figure 4.11

shows the reflected shear wave for the multilayered structure integrated with a dissipative layer.

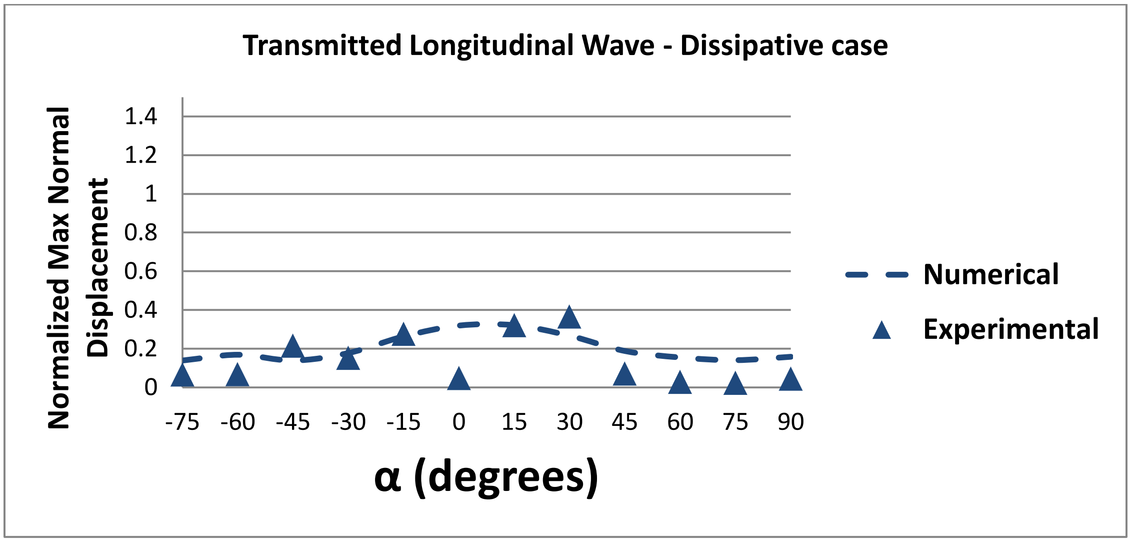

Figure 4.8: Transmission of longitudinal wave through the block of dissipative multilayered structure showed in Figure 4.1b as received in MN.

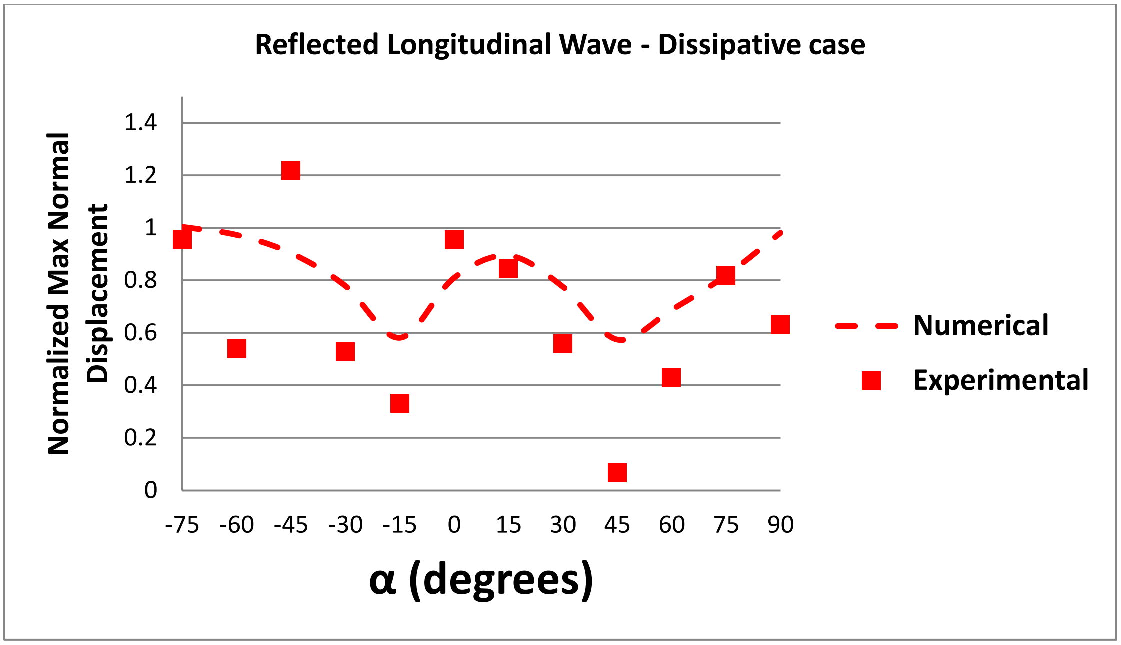

Figure 4.9: Longitudinal wave reflected back from the block of dissipative multilayered structure shown in Figure 4.1b as received in PQ.

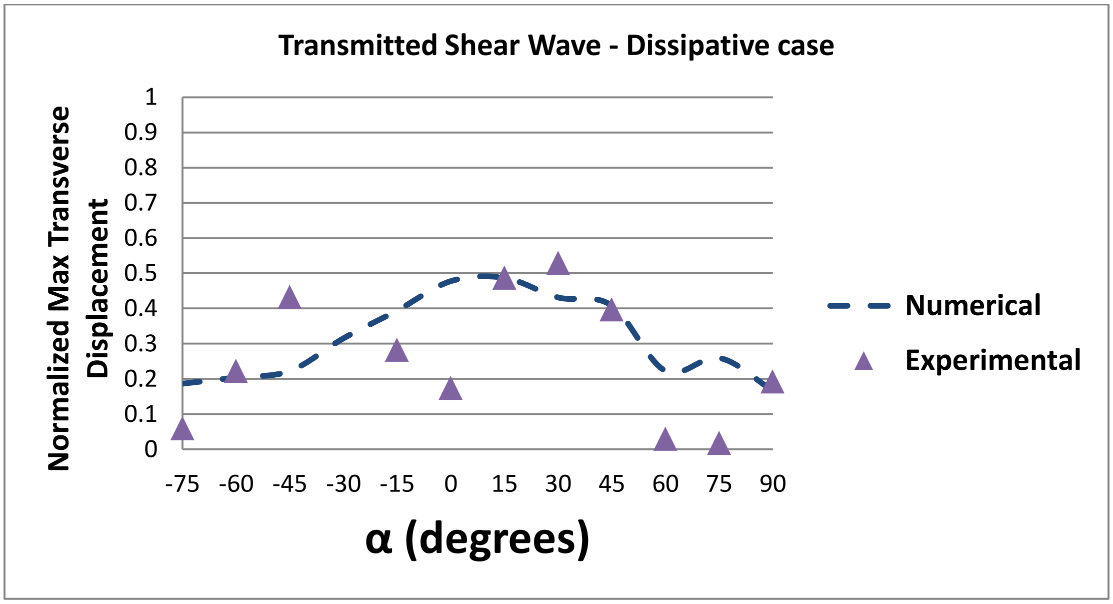

Figure 4.10: Transmission of shear wave through the block of dissipative multilayered structure showed in Figure 4.1b as received in MN.

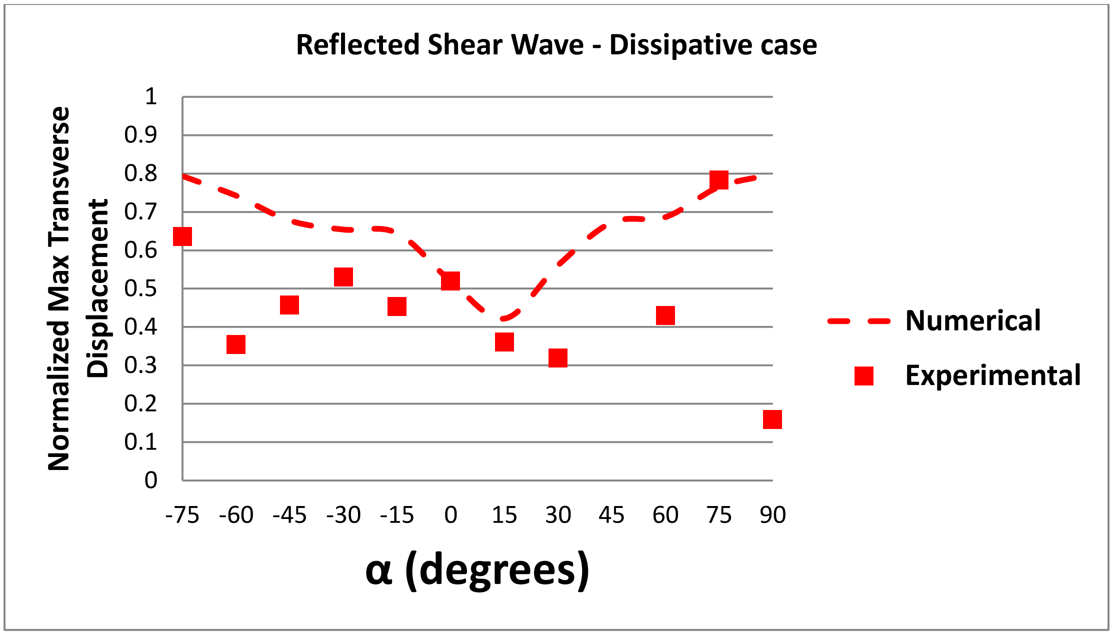

Figure 4.11: Shear wave reflected back from the block of dissipative multilayered structure shown in Figure 4.1b as received in PQ.

4.3. Material preparation

In order to experimentally verify the numerical computation results, strongly anisotropic materials are required with desirable anisotropy orientation. We have chosen unidirectional Carbon fiber reinforced polymers for their high ratio of the elastic anisotropy in the fiber direction with respect to the transverse direction. Subsequently, the quasi-longitudinal wave speed is significantly faster in the preferred axis of material stiffness.

Figure 4.12: Pieces of customized Carbon Fiber reinforced composites are stacked and bonded together using Scotch-Weld epoxy under 2 MPa pressure at 66°C.

Unidirectional CFRP plates were fabricated by DragonPlate, a manufacturing firm specializing in design and custom fabrication of Carbon fiber components. The thickness of CFRP sheets is an important design parameter, since we intend to perform in-plane ultrasonic experiments using piezoelectric transducers with 12mm diameter. Due to the manufacturing limitations on customized composites, the synthesized CFRP plates were 3mm thick. Therefore, we stacked 4 manufactured plates of unidirectional composites and used Scotch-Weld gray epoxy adhesive in order to achieve a final thickness of 12mm (Figure 4.12). The epoxy was applied evenly to the surfaces in contact, which were then put under 2MPa pressure. The epoxy was fully cured after 2 hours at 66°C, based on the manufacturer’s recommendation.

We aim to produce samples that possess specific orientations of anisotropy in order to investigate the effect of elastic anisotropy of the constituents of a multilayered structure. As shown in Figure 4.13, a rectangular cuboid can be cut out of a unidirectional CFRP at a specific angle ψ in order to achieve the desired orientation of anisotropy. Furthermore, wedges with desirable angles are cut out of the same plate, which will provide the capability of sending an incident plane-wave at a given angle of incidence. The cutting process involves water jetting the CFRP plate and then machining the parts to the final dimensions with smooth surfaces, which is handled in collaboration with the Campus Research Machine Shop at UCSD. Figure 4.14 shows a picture of the machined parts resulting in the samples with α=±45°.

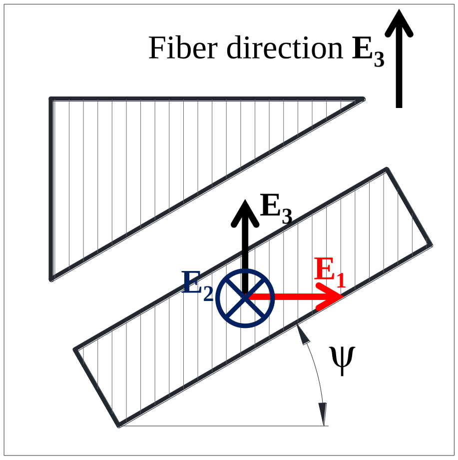

Figure 4.13: Water jetting rectangular cuboids and triangular wedges out of a unidirectional CFRP plate in order to develop customized orientation of anisotropy depending on the angle ψ.

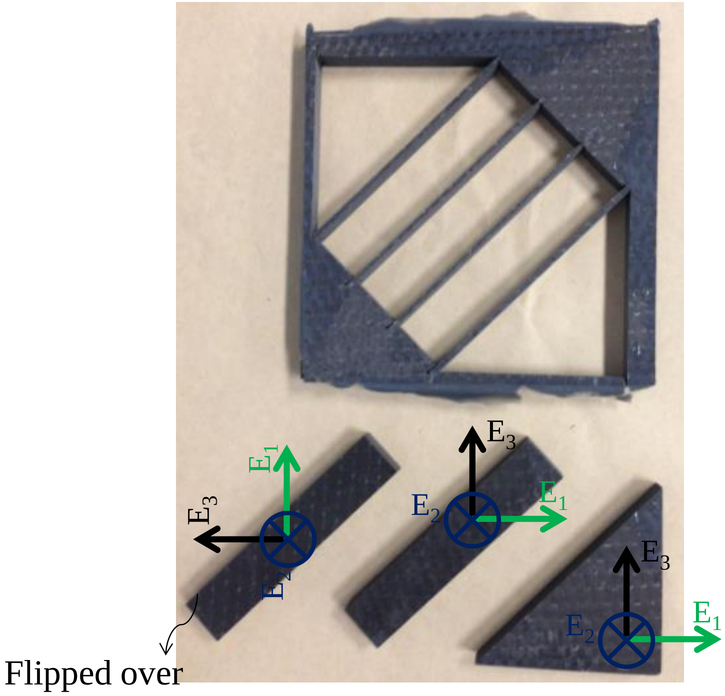

Figure 4.14: CFRP samples with the desired orientation of anisotropy are cut using water-jet and machined to attain the final size and geometry. This figure corresponds to α=±45°.

4.4. Experiments

In subsection 4.4.1, we explain the experimental setup for the measurements of ultrasonic wave propagation in the anisotropic multilayered structures. We present the elastic moduli in subsection 4.4.2 by measuring time of travel of longitudinal and shear waves. In subsection 4.4.3 we show that the incident pulse duration is short enough compared to the sample size to make meaningful measurements. Finally in subsection 4.4.4 we present the experimental results of transmitted and reflected pressure and shear waves.

4.4.1. Experimental setup

The experimental setup, as shown in Figure 4.15 is comprised of piezoelectric transducers, signal generators, an RF amplifier, and an oscilloscope. A customized electrical signal is generated with most of its energy concentrated at 1MHz frequency, which is then amplified to excite the piezoelectric transducer. The contact transducer induces mechanical perturbation to the samples. In order to facilitate such transfer, proper ultrasonic couplants are applied at the interface of samples with pressure or shear transducers. An ultrasonic transceiver can then be placed on designated locations on the outer surfaces of the multilayered structure in order to detect the transmitted or reflected signal in pressure or shear mode.

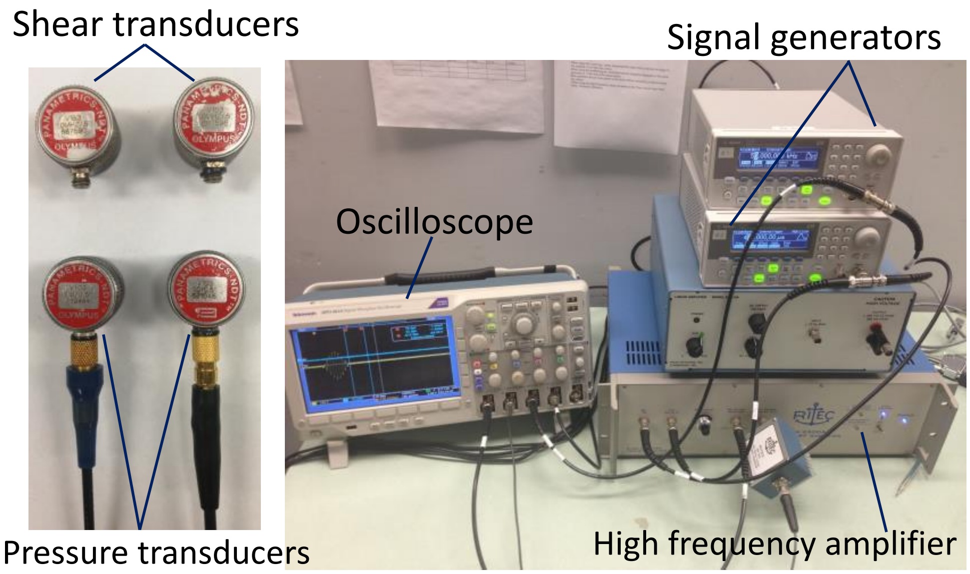

Figure 4.15: Experimental setup for evaluating pressure and shear wave propagation in around 1MHz frequency.

We characterized the behavior of ultrasonic transducers before making any measurement on the actual model. We measured the electrical signal generated by a high frequency RF amplifier and recorded it through the oscilloscope (solid blue line in Figure 4.16). The piezoelectric transducer (PZT) takes this signal as an input and generates a mechanical perturbation that we measure. We use another identical transducer and place the two PZT tightly together. The transceiver measures the mechanical signal and transfers it to an electrical signal recorded through the oscilloscope (solid red line in Figure 4.16). The two shown signals are not physically comparable, yet this exercise allows us to understand the actual signal travelling through the samples of interest.

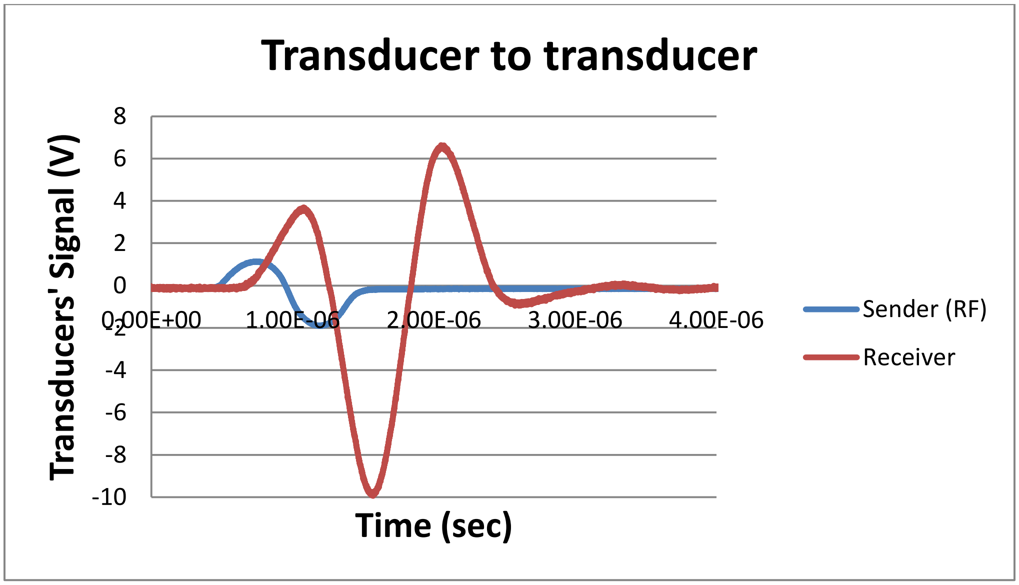

Figure 4.16: Measuring the transmission of a signal between two identical pressure transducers. The measurement of the electrical signal generated by an RF amplifier is shown for the sender. This signal is then transferred to a mechanical perturbation of the sender and transmitted to a transceiver. The measurement from the receiver is recorder using the oscilloscope and plotted here.

4.4.2. Elastic moduli Measurements

The elastic moduli of the unidirectional CFRP were calculated by measuring the longitudinal and shear wave speed in the samples. The unidirectional fiber reinforced composite behaves as a transversely isotropic material with 5 independent elastic moduli.

We used two identical rectangular cuboid samples of CFRP with the fibers making 0° or 90° angle with the surfaces. The time of travel of quasi-longitudinal waves along the fiber direction, and also normal to the fibers were measured. The quasi-longitudinal wave speed was measured as 8850 m/s in the stiffest direction and 2590 m/s normal to the fibers. The quasi-shear wave speed along the fiber direction was measured as 2116 m/s and the speed of a pure shear wave in the plane of isotropy was measured as 1250 m/s. We can compute four of the five elastic moduli using the measured wave speed. In order to find the fifth independent elastic modulus, a sample of unidirectional CFRP with fibers oriented at 45° angle with respect to the rectangular cuboid sample was tested. The quasi-longitudinal wave speed for the 45° angle was measured as 6560 m/s.

The wave speed measurements yielded the following elastic moduli: E_3=72.4GPa, E_1= E_2=5.8GPa, G_{13}=6.0GPa, G_{12}=2.1GPa, and ν_{12}=0.3875. This confirms the strong anisotropy we require to manage the stress-wave propagation at the interface of the layered structure.

4.4.3. Time of travel and pulse duration

Since we intend to propagate a pulse of finite duration and measure reflection and transmission, it is necessary to ensure that the pulse duration is smaller than its time of travel from a transducer to a transceiver. This guarantees that the incident and scattered waves do not interfere. The sinusoidal pulse that we intend to use as an incident wave has 1μsec duration. However, we observed that in piezoelectric transducers for our setup, the intended signal duration extends to 2μsec when the RF signal is transferred to a mechanical signal. The wave speed along the fiber direction in the CFRP is measured as 8850m/s. The minimum distance in any of the performed ultrasonic measurement is 26mm, which translates to a time of travel of 2.9μsec. Therefore, we conclude that the considered pulse duration is short enough to make meaningful measurements.

4.4.4. Measuring transmitted and reflected signals

The purpose of the experiments using ultrasound equipment is to verify the numerical prediction of the behavior of multilayered structure as a whole. We consider the 3-layered structure as a black box, and we are interested in characterizing the transmission and reflection of an incident wave generated through a piezoelectric transducer. The transmission and reflection waves are measured at the outer boundary of the multilayered structure shown in Figure 4.1.

Here, we present the procedure for collecting the individual measurements and build up the platform for presenting the processed data. We consider the numerical model discussed in section 4.2 with a wedge angle of 15°; and produce its experimental counterpart as shown in Figure 4.17. We have used two industrial C-clamps to hold the pieces of unidirectional carbon fiber reinforced composite tightly together. Ultrasonic couplant was applied at the interface of pieces to facilitate the wave propagation through the layers. The setup including the layers A and C are fixed throughout all the experiments, except for the middle layer B which is the subject of our study.

We performed one set of experiment for each 12 choices of $\alpha \in \{0, \pm 15, \pm 30, \pm 45, \pm 60, \pm 75, 90\}$ in order to study the effect of the orientation of anisotropy of layer B. Here we present the data collection for a representative case of $\alpha=0°$. A Panametrics ultrasonic transducer (V103) with a diameter of 12 mm is used to propagate a sinusoidal pulse of 1MHz dominant frequency. The piezoelectric transducer is placed on the boundary surface of layer A between the two clamps, simulating the excitation at point R in the numerical model (Figure 4.1). An identical transducer to the mentioned PZT is placed on the outer boundary of layer C facing the transmitter, which is used to receive the signal transmitted through the multilayered structure. The received signal at the middle of PQ in layer C is shown in Figure 4.18. We take the average of positive and negative peak as the recorded amplitude of the transmission wave for this single measurement.

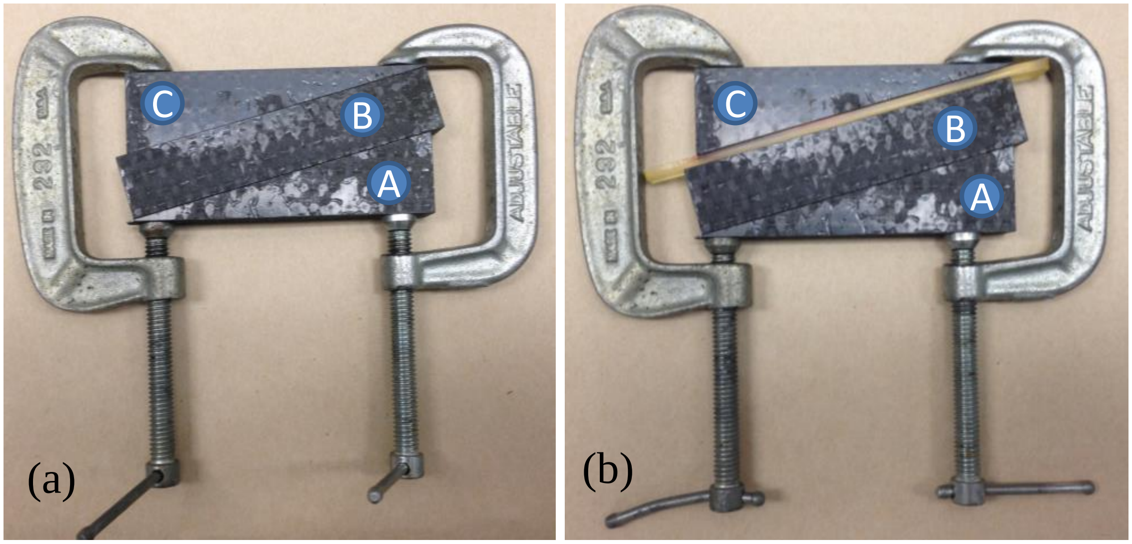

Figure 4.17: (a) Three-layered elastic structure and (b) integrated multilayered structure with a dissipative layer assembled using clamps. This figure shows the experimental counterpart of the numerical models shown in Figure 4.1.

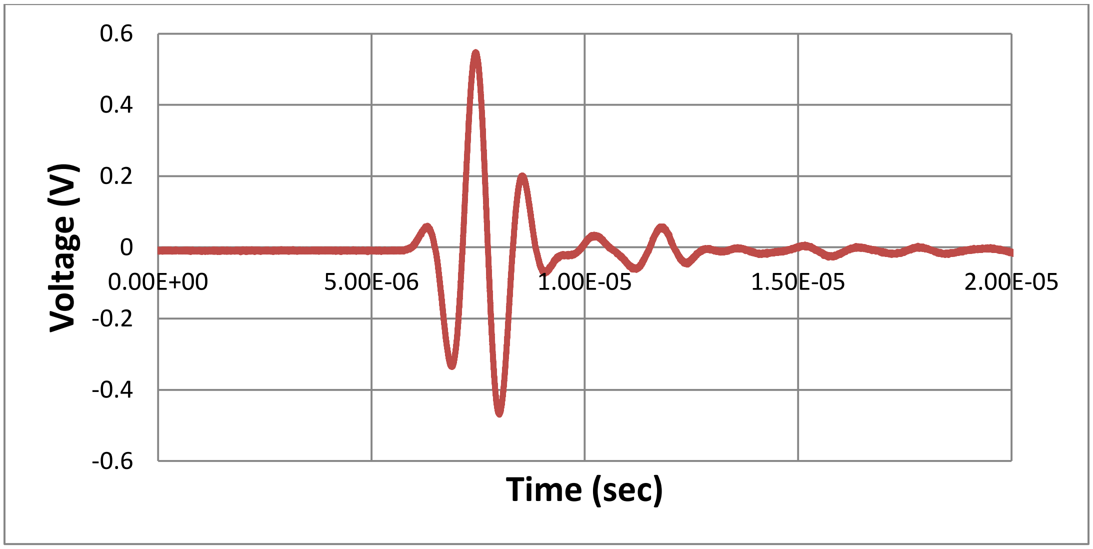

Figure 4.18: An example of a transmitted signal at the middle of MN in Figure 4.1 for the case α=0°.

We now repeat a similar measurement by keeping all the setup including the position of signal generating transducer constant and changing the position of transceiver on a grid of points on the outer boundary of layer C in order to scan the transmission wave on PQ in in Figure 4.1. The amplitude of all the recorded measurements are computed as explained in the last paragraph. Then the maximum of these amplitudes is considered as the data point for the transmitted wave at α=0°. In order to compare the experimental results and numerical simulations, we normalize this data point (voltage) to attain displacement.

We performed the explained experiment with all other considered orientations of anisotropy for the layer B, and plot the normalized measurements in Figure 4.4 with solid triangles. The normalization factor is chosen such that the numerical and experimental value matches each other for α=0°. It is observed that the trend of experimental measurements and numerical predictions strongly agree with each other.

The reflection measurements follow a very similar procedure as the data collection for transmission. A transducer is placed on the layer A close to the signal generating transmitter to measure the signal reflected off of the multilayered structure as a whole. Although we are not able to measure the reflection exactly at point R of Figure 4.1, due to the interference with the transducer generating incident wave, we can scan the rest of the outer boundary of layer A. These measurements are normalized with respect to the normal displacement predicted by the numerical predictions at the corresponding elements. The result is shown in Figure 4.5 with square dots.

The measurement of scattered shear waves is a crucial component of our ultrasonic experiments. While the signal generating transducer (V103) produces longitudinal waves, the transceiver is a Panametrics shear transducer (V153). We are replicating the conditions in the numerical model, where the incident longitudinal wave is scattered as partly longitudinal and partly shear waves. The procedure for processing the individual measurements is exactly the same as that of longitudinal waves. Figure 4.6 and Figure 4.7 show the transmitted and reflected shear waves respectively.

In the second set of experiments, we introduced a thin layer of dissipative polymer (Polyurea) in between the layers B and C, as shown in Figure 4.17b. The experimental procedure is exactly the same as that of elastic case. The triangles in Figure 4.8 show the normalized maximum transmitted longitudinal wave; the square dots in Figure 4.9 show the normalized maximum reflected longitudinal wave; the triangles in Figure 4.10 show the normalized maximum transmitted shear wave; and finally the square dots in Figure 4.11 show the normalized maximum reflected shear wave.

4.5. Discussion and summary

We have shown that the orientation of anisotropy of a layer in a multilayered structure has an immense impact on the wave scattering in longitudinal and shear modes. We have performed numerical computations using the Finite Element Method and experiments using ultrasound equipment to verify the possibility of designing a layered structure that enables us to manage the stress wave propagation in solids.

We are particularly interested in a design that can transfer a significant portion of longitudinal stress-wave energy of the impinging perturbation into shear wave energy. The comparison of the amplitude of scattered longitudinal wave for the elastic case and dissipative case is shown in Figure 4.19, while Figure 4.20 shows similar comparison for shear waves. It is observed that by selecting α around 45°, we have the most transfer of longitudinal wave energy into shear wave energy. The amplitudes of transmitted and reflected longitudinal waves are simultaneously minimized in the elastic multilayered structure. The transmitted shear wave, on the other hand, is maximized in order to satisfy energy conservation.

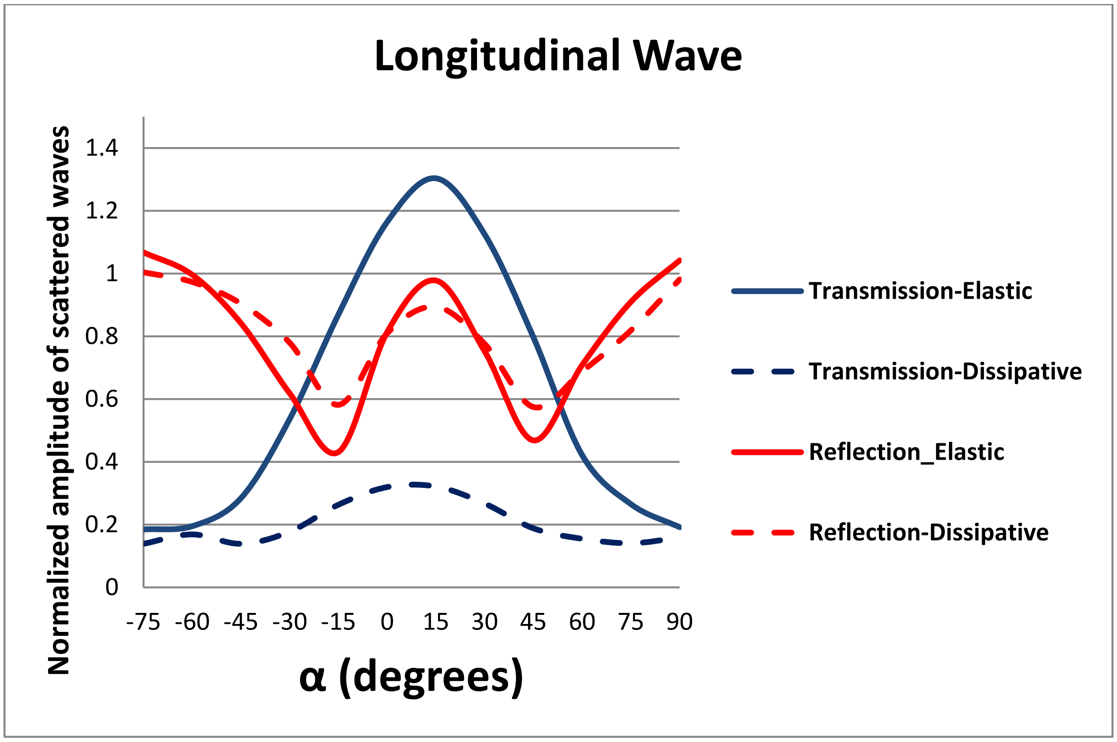

Figure 4.19: Comparison of the scattered longitudinal waves in elastic (solid lines) and dissipative cases (dashed lines). While the reflected longitudinal waves are remained almost the same, the transmitted longitudinal waves are diminished by a significant factor. Thus, combination of stress-wave management via layering of anisotropic materials and viscoelastic shear dissipation resulted in significantly reduced transmitted longitudinal wave amplitude.

The initial intent for introducing a shear dissipative material in a multilayered structure was to dissipate the energy of scattered shear waves. We have shown that a specific design results in the maximum transfer of stress-wave energy from longitudinal modes into shear modes. The comparison of the amplitudes of the scattered shear waves between the elastic and dissipative case (Figure 4.20) proves that the shear-dissipative layer performs a good job in terms of diminishing the transmitted shear wave at α=50°.

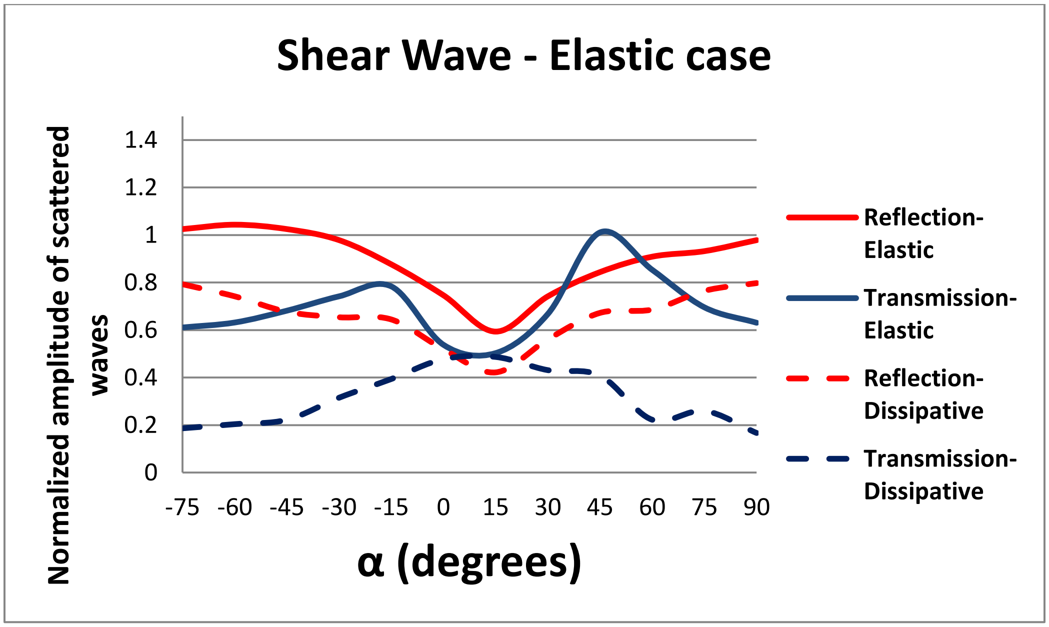

Figure 4.20: Comparison of the scattered shear waves in elastic (solid lines) and dissipative cases (dashed lines). The amplitude of the transmitted shear wave in the dissipative case is diminished by a significant factor relative to the elastic multilayered structure.

We proved that the combination of stress-wave management via layering of anisotropic materials and viscoelastic shear dissipation resulted in immense control on impinging stress-waves. The energy of incident longitudinal wave is transferred into shear waves, which are then dissipated by integrating a shear-dissipative material.

4.6. References

[1] Achenbach, J.D., 1973. Wave propagation in elastic solids, North Holland, New York.

[2] Auld, B.A., 1973. Acoustic fields and waves in solids, John Wiley & Sons, New York.

[3] M.J.P. Musgrave, Crystal Acoustics, Holden-Day, San Francisco, CA, 1970.

[4] Ewing, W.M., Jardetsky, W.S. and Press, F., 1957. Elastic waves in layered media, McGraw Hill, New York.

[5] Brekhovskikh, L.M., 1966. Waves in layered media, Academic, New York.

[6] Nayfeh, A.H., 1990. The general problem of elastic wave propagation in multilayered anisotropic media, J. Acoust. Soc. Am. 89, 1521-1531.

[7] Nayfeh, A.H., 1995. Wave propagation in layered anisotropic media, North Holland, Amsterdam.

[8] Tehranian, A., Amirkhizi, A.V., Irion, J., Isaacs, J. and Nemat-Nasser, S., 2009. Controlling acoustic-wave propagation through material anisotropy, Proceedings of SPIE. 7295, 72950V1-4.

[9] Alireza V. Amirkhizi, Aref Tehranian, Sia Nemat-Nasser, Stress-wave energy management through material anisotropy, Wave Motion, Volume 47, Issue 8, December 2010, Pages 519-536.

Chapter 5

Polyurea Foam

Recently, there have been extensive studies on mechanical properties and microstructure of Polyurea, a copolymer of hard segments slightly cross-linked and embedded in a soft matrix. The shear stiffness of materials of this kind can change by at least two orders of magnitude under large pressure encountered under shock wave. In the current study, we are introducing non-uniform distributed voids in polyurea to create a lighter and softer material that has the potential to improve shock mitigation. The new microstructure is achieved through a chemical process by introducing CO_2 bubbles as a result of the chemical reaction of constituents of Polyurea (Versalink and Isonate) and water molecules. The size and the volume fraction of the voids are measured for different stoichiometry of the reaction.

Storage modulus and loss modulus of the new materials are measured using Dynamic Mechanical Analysis (DMA); and the elastic properties were measured under compression at temperatures higher and lower than the glass transition temperature of the material. The fabricated material is generally softer than pure Polyurea and has lower storage and loss modulus. The size and the spacing of the voids are measured using the micrograph of the material. These are incorporated in a micromechanics model to achieve the bulk properties of the copolymer with distributed voids, which will then be compared with the experimental measurements.

5.1. Introduction

In the recent years, there has been an interest in understanding mild Traumatic Brain Injury (TBI) caused by blast explosions [1] and consequently in developing materials or structures to reinforce helmets in order to mitigate the shock waves [2]. Schimizzea et al. [3] notes the importance of density and impedance of a material for helmet padding in mitigating an air shock wave. It is crucial to incorporate a low density and porous material in order to attenuate the impinging wave by absorptive and dissipative mechanism. Polyurea has been proven effective in mitigating blast-induced shock wave. Therefore, a porous structure with Polyurea as its matrix is an excellent candidate for research.

The motivation for synthesizing Polyurea based foam consists of several factors including high energy absorption, light weight, higher elastic modulus to density ratio (compared with Polyurea), and collapsible voids under extreme loading. Pure Polyurea offers unique properties such as increased shear stiffness under large pressure, which is beneficial in controlling elastic stress-waves and shock waves. A porous structure with

Polyurea matrix can be integrated into a layered structure to enhance management of stress-waves.

5.2. Material synthesis

Polyurea is a copolymer of hard segments slightly cross-linked and embedded in a soft matrix. Fragiadakis et al. [4] studied the effect of stoichiometry of hard and soft segments in the mechanical properties of Polyurea chain. The reaction is shown in Figure 5.1. In the current study, we intend to modify the chemical reactions by introducing a substance that would result in a product in gaseous phase that can play the role of a blowing agent in order to create foam.

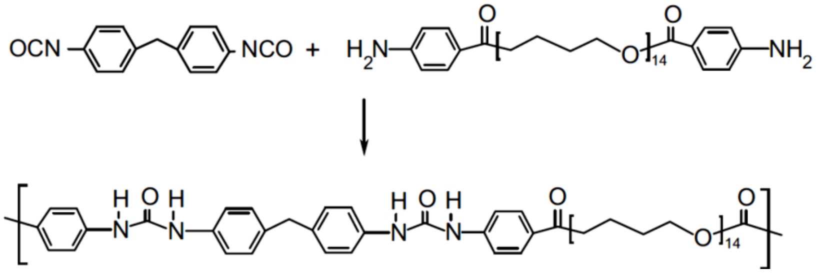

Figure 5.1: The reaction of isocyanate and Versalink resulting in Polyurea.

5.2.1. Synthesis procedure

The most accessible substance that can react with isocyanate is H_2O molecules. We found that the reaction of water and isocyanate is very favorable and releases CO_2. Each mole of isocyanate reacts with 2 moles of H_2O, which results in the release of 2 moles of CO_2 as a product. In order to have a uniform distribution of Carbon dioxide in the final product, it is important to have water molecules dispersed in the mixture as much as possible. Since Versalink P-1000 oligomeric diamine does not react with water, we have chosen to mix calculated amount of water with Versalink in our synthesis procedure.

We developed the following procedure for synthesizing polyuria foam:

1. Degas Versalink and Isonate components separately for 1 hour under 1 Torr vacuum.
2. Remove vacuum from Versalink, add water to Versalink, and stir using a magnetic stir bar while physically rotating bottom portion of reaction flask in order to mechanically integrate water into Versalink – mix for 5 minutes
3. Add Isonate to Versalink/Water mixture and mix for 1.5 minutes – in open air (not under vacuum)
4. Pour the products into Teflon molds in order to obtain desired sample geometries
5. Place the molds in the environmental chamber for curing

Since the Versalink and H_2O molecules both compete for the isocyanate molecules during the synthesis procedure, it is required to account for the excess Isonate 143L enough to form Polyurea matrix as well as CO_2 bubbles. In order to calculate the amount of reactants, we start with the stoichiometry of synthesizing pure polyurea as a baseline. The amount of excess Isonate is assumed as a weight percentage of the baseline polyurea. Then the weight of required water is computed based on the molecular weight of water and Isonate 143L. The equivalent weight of Isonate 143L is 144.5 g/mol, while that of water is 18 g/mol. The stoichiometry of synthesized samples is discussed in section 5.2.2.

5.2.2. Synthesized samples

We incorporated the synthesis procedure discussed in section 5.2.1 to synthesize polyurea foam consisting of 50% excess Isonate in material B, and 100% excess Isonate in material C as noted in Figure 5.2. The weight percentage of water added to react with excess Isonate is calculated as 1.1% and 2% respectively. Table 5.1 shows the mass of each component used in synthesizing the samples. We considered synthesis of pure polyurea samples as a baseline for comparison purposes (material A). Finally, we synthesized material D with no excess Isonate, where the water molecules and Versalink compete for isocyanate molecules. The expectation is that the insufficient amount of Isonate results in limited cross-linking and a weak matrix surrounding the voids created by CO_2 gas.

We used two types of Teflon molds to achieve samples for both uniaxial compression test, and dynamic mechanical analysis. We used a cylindrical mold with a clamped bottom piece and open-top to fabricate samples with 2.54cm diameter and 2.54cm in height (Figure 5.3). The materials are poured into the molds while the reactions and foaming process is in progress. Additionally we fabricated rectangular cuboid with cross section of 10mm x 3mm and 140mm long.

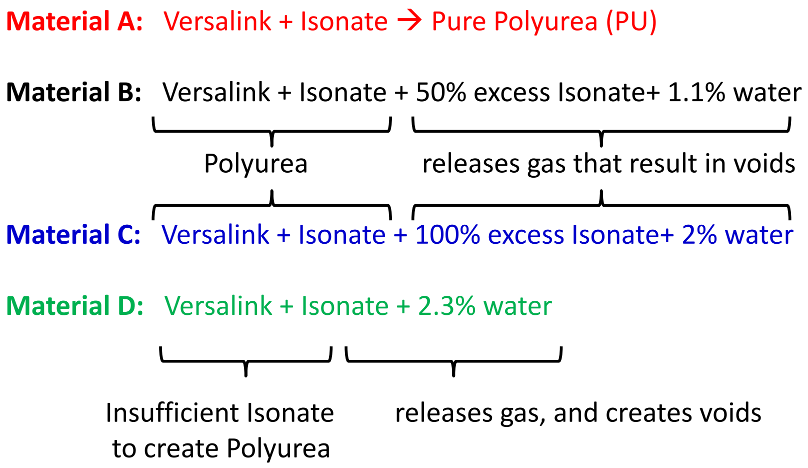

Figure 5.2: Diagram of the building blocks of synthesized materials, including the matrix, and the blowing agent (CO_2 gas).

Table 5.1: The mass of each component involved in synthesizing the samples.

Material	Versalink (g)	Isonate (g)	Water (g)	Total mass (g)
A	46	11.6	0	57.6
B	40.3	14.56	0.606	55.47
C	40.3	20.5	1.228	62.03
D	40.3	10.2	1.212	51.7

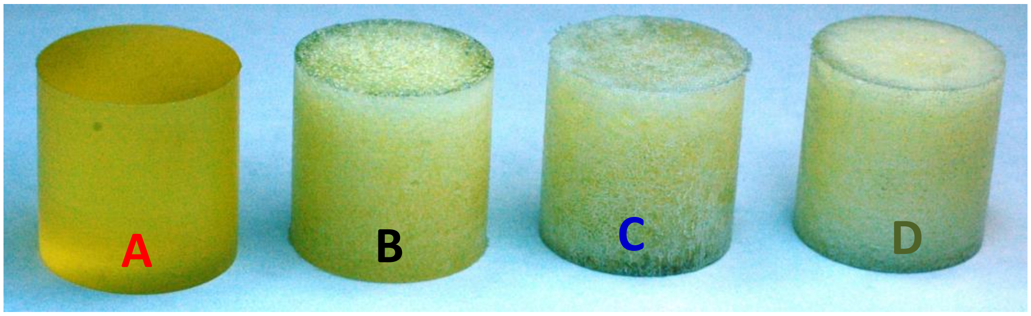

Figure 5.3: Synthesized cylindrical samples with a diameter of 2.54cm, and height of 2.54cm.

5.2.3. Non-uniformity of the distributed voids

The synthesized foam samples were observed to have non-uniform distribution of pores. There are several factors contributing to this phenomenon. The most important contributing factor is that the Teflon molds used in synthesizing the samples have an open top surface exposing the reactant to atmospheric pressure. Therefore, the CO_2 bubbles prefer to travel vertically (upward) in order to balance the air pressure in the reactants until the matrix builds up its structural integrity. The material pushed upward forms a mushroom-like geometry at the open top surface of the mold. We cut this part with a razor in order to achieve a cylindrical sample. It is important to note that the synthesized foam samples have a gradient in density and voids volume fraction in vertical direction.

Another important factor resulting in the non-uniformity of pores distribution in the samples is the boundary layer of the materials close to Teflon mold surfaces. While the reactants flow in the molds until the products reach structural stability, their boundary layer facing the mold is constrained. This results in different pore size shown in Figure 5.4.

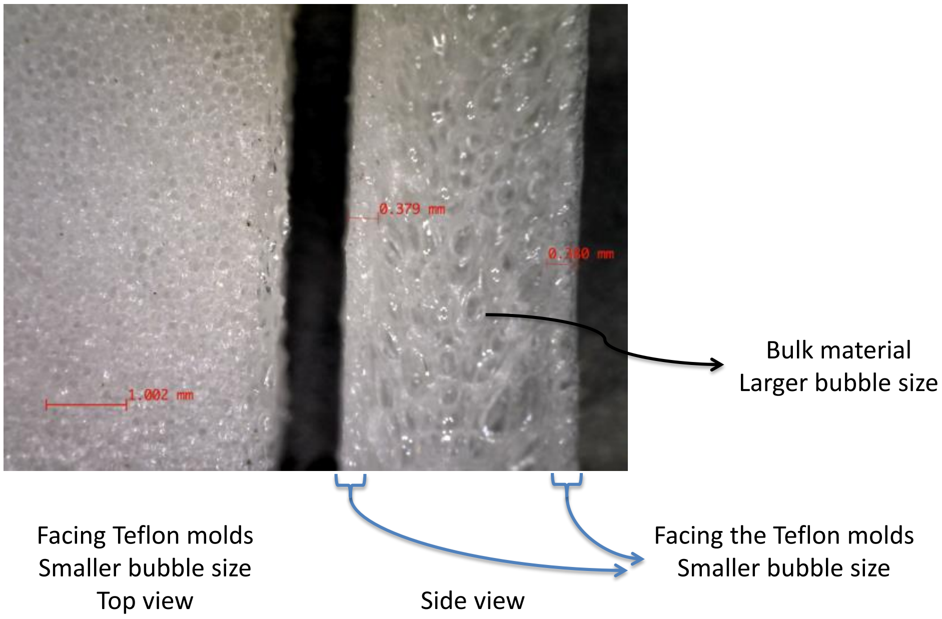

Figure 5.4: Non-uniform distribution of pores facing the Teflon molds and pores in the bulk material.

5.2.4. Containment of blowing agent

We discussed in section 5.2.3 that the blowing agent (CO_2) was not contained in the samples per the configuration of open-top molds. Therefore, only a small portion of produced carbon dioxide contributes to the volume fraction of voids in the final samples. Here, we present an ideal case where all the produced gas is contained in the sample, and back calculate what weight percentage of water and Isonate would have created a similar volume fraction of voids if the carbon dioxide was completely contained in a pressurized and bounded molds.

We consider a synthesized cylindrical sample with a diameter of D=2.54 cm and height of H=2.54 cm with a given volume fraction of voids (V_f). We then calculate the volume of the CO_2 voids: $V_{CO_2}=V_f.\pi D^2H/4$. We use the equation of state for ideal gas (PV=nRT) to calculate the number of moles of CO_2 assuming 1 atm pressure and 300°K temperature. According to the discussion in section 5.2.1, the number of moles of water required to produce CO_2 is found: $n_w=n_{CO_2}=0.0015\ V_f$. The volume fraction of voids in materials A through D in Table 5.1 are measured 0, 27%, 44%, and 45% respectively; the amount of water that is calculated using the above calculations give: 0, 7.5mg, 12.3 mg, and 12.5 mg respectively.

5.3. Material characterization

The synthesized samples of polyuria foam were characterized to find mechanical properties of interest such as density, microstructure, storage and loss modulus, and stress-strain behavior under compression. We considered 3 different stoichiometry for synthesizing polyuria samples with distributed voids (described in section 5.2); and compared the results with pure polyurea. In the following sections, we describe these properties in detail:

5.3.1. Microstructure

The microstructure of the synthesized materials was studied using Dino Lite digital microscope. The porous structures of the materials are shown in Figure 5.5. The void sizes are measured about 100μm for materials B and D, and 250μm for material C.

The density of cylindrical samples with dimensions D=H=2.54cm were measured as shown in Figure 5.5. Assuming the matrix of porous structure has the same density as pure polyurea, we calculated the volume fraction of voids in each sample.

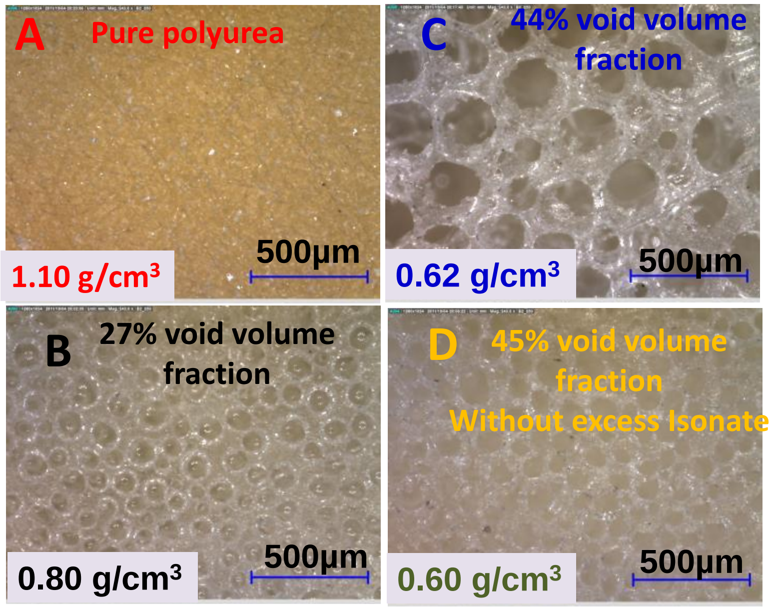

Figure 5.5: Micrograph of fabricated polyurea and polyurea based foam. The stoichiometry of synthesizing Polyurea is modified to calculate the required weight percentage of Versalink, Isonate, and added water to produce CO_2 bubbles which results in a porous microstructure.

5.3.2. Storage and loss modulus

Dynamic Mechanical Analysis (DMA) is used to characterize the storage and loss modulus of the material. The tests were done with single cantilever method at 10Hz frequency of the clamp oscillation. The loss modulus, storage modulus, and tan (δ) are shown in Figure 5.6 for a range of temperature from -80°C all the way to 50°C. Both moduli are smaller in foam samples than those in pure polyurea. However, the modulus to density ratio is higher for material B with closed-cell microstructure than pure polyurea.

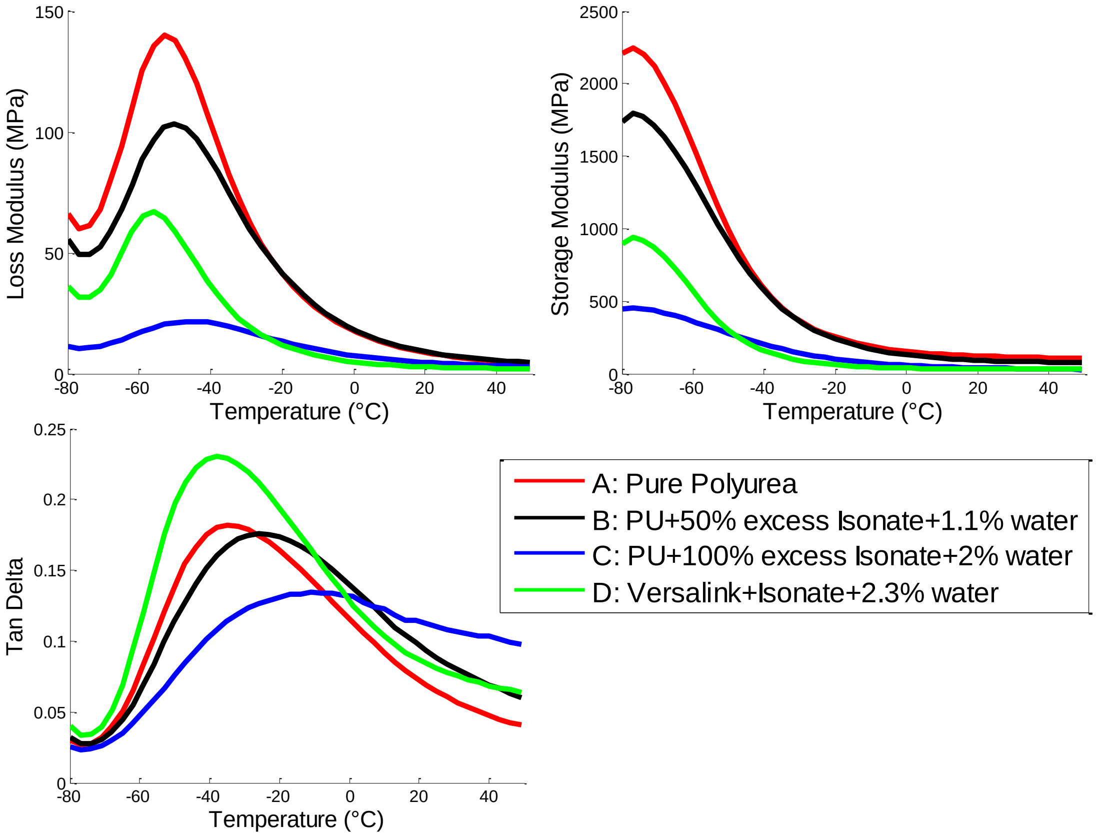

Figure 5.6: Loss Modulus, Storage modulus, and Tan (δ) versus temperature for samples shown in Figure 5.5. In porous samples, both moduli are lower than those in pure Polyurea.

We used a micromechanics model for a matrix with periodic distribution of voids and computed the storage and loss modulus of a porous polyurea. The solid lines in Figure 5.7 show the numerical model prediction for a range of void volume fraction. The square dots show the experimental results from the synthesized samples. It is observed that the actual matrix of material B is stiffer than pure polyurea, while materials C and D show close agreement with numerical predictions.

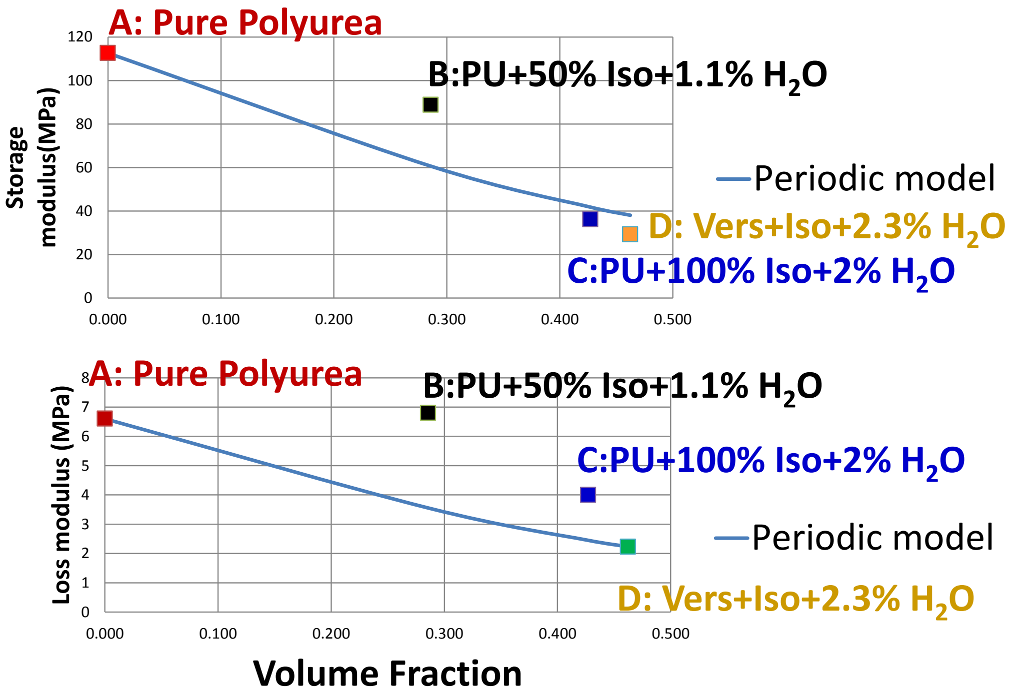

Figure 5.7: Micromechanics periodic model to estimate moduli of porous materials and comparison with measured value (square dots).

5.3.3. Stress strain relationship

The stress-strain relationships for the synthesized materials were studied at -50°C, 18°C, and 50°C temperatures. The cylindrical samples of dimensions D=H=2.54cm were placed under compression with load-controlled clamps. The samples were loaded to 0.35MPa compressive stress and then unloaded in a chamber equipped with temperature controller using liquid nitrogen and heater. The uniaxial stress and strain were measured and plotted in Figure 5.8.

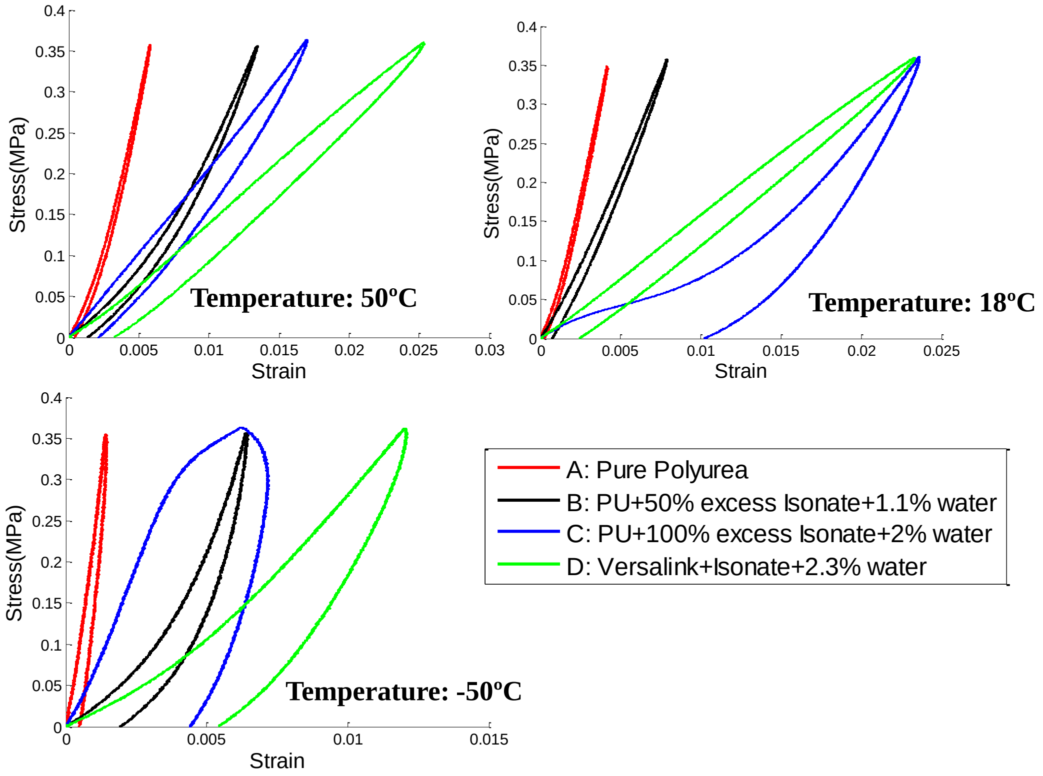

Figure 5.8: Stress-strain behavior under uniaxial compression at 50°C, 18°C, and -50°C.

5.4. Experiments to study critical parameters affecting void size

One of the most important characteristics of the porous polyurea foam is the size of the voids in the microstructure. Depending on the volume fraction of voids and their sizes, we may have an open-cell foam or closed-cell foam. Smaller void sizes are favorable to enhance the structural integrity of the material.

There are several parameters in the synthesis process affecting the void size of polyurea foam. First, the emulsion of water and Versalink determines the size of water droplets that will react with isocyanates later in the process. According to Taylor’s formula [5], the water droplet can be broken to smaller size in a shear flow. The viscosity of Versalink and the interfacial surface tension between the two components of emulsion are the deciding factors in addition to the shear rate enforced by a mixer. We conducted experiments to study both critical parameters, which are furthere discussed in sections 5.4.1 and 5.4.2.

Another critical parameter affecting the foaming process is the amount of time it takes to cure the polyurea matrix in order to maintain its structural integrity, which will lock out the bubbles in the porous structure. We studied the initial stage of curing Polyurea using a rotational viscometer. The experiment is further discussed in section 5.4.3.

5.4.1. Viscosity of Versalink P-1000 vs. temperature

We measured the viscosity of Versalink P-1000 using a falling sphere viscometer. The velocity of a sphere was measured while falling through a 25 mL graduated cylinder filled with Versalink. We performed a total of 6 tests using 2 sphere sizes (0.79 mm, 1.59mm ball bearing) at 3 given temperatures (13.3°C, 22.8°C, 42.0°C). A snapshot of the test setup was taken every 4.0 sec. The series of pictures taken for 1.59mm sphere at 22.8°C is shown in Figure 5.9.

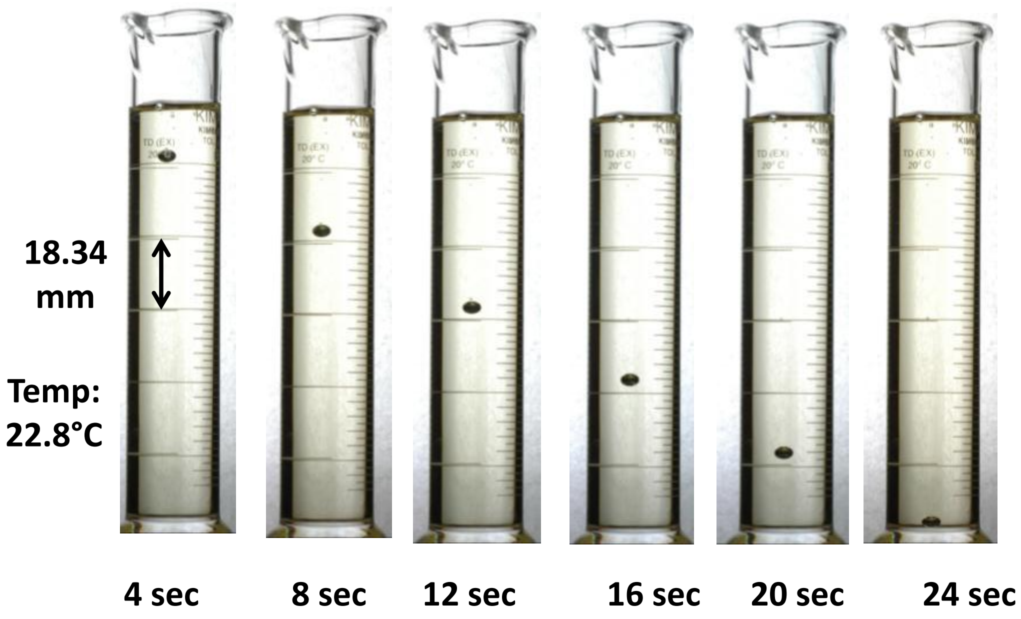

Figure 5.9: Measuring the viscosity of Versalink P-1000 in a 25 mL graduated cylinder using a falling 1.59mm sphere at 22.8°C. Snapshots of the cylinder are shown with 4 sec intervals.

The viscosity is calculated using the following equation: $\eta = K\frac{2gr^2(\rho_s-\rho_v)}{9v}$, where η is viscosity, g is gravity constant (9.81 m/s^2), r is the sphere radius (0.79 mm, 1.59mm), ρ_s is the sphere mass density (7.9 g/cm^3, 7.6 g/cm^3 respectively), ρ_v is the mass density of Versalink (1.04 g/cm^3), v is the measured speed of spheres in m/s, $K = 1 - 2.104\left(\frac{2r}{D}\right) + 2.09\left(\frac{2r}{D}\right)^3$ is the corrective factor for the finite size of sphere relative to the cylinder, given by ASTM D 1343-95, and D is the inner diameter of the cylinder (18.90 mm). The results of the measurements are averaged for the two sphere sizes and are shown in Figure 5.10.

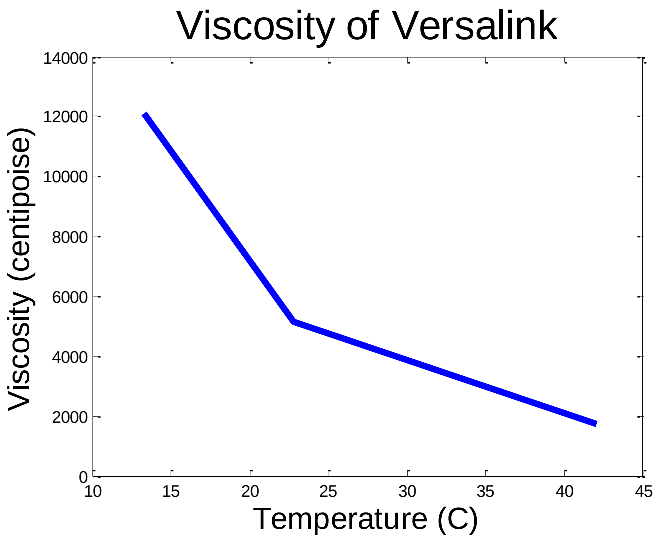

Figure 5.10: Viscosity of Versalink P-1000 oligomeric diamine as a function of temperature.

5.4.2. Surface tension between water and Versalink P-1000

The interfacial surface tension between a droplet of water and Versalink was measured. A thin layer of Versalink was retained on a lab slide in contact with air, and a water droplet was placed on top of Versalink (Figure 5.11). The interfacial surface tension was calculated using the following equation: $\gamma=\Delta\rho.g.\ Z_e^2/2=1.4$ mN/m = 1.4 dyne/cm, where Z_e was measured 538μm as shown in Figure 5.11.

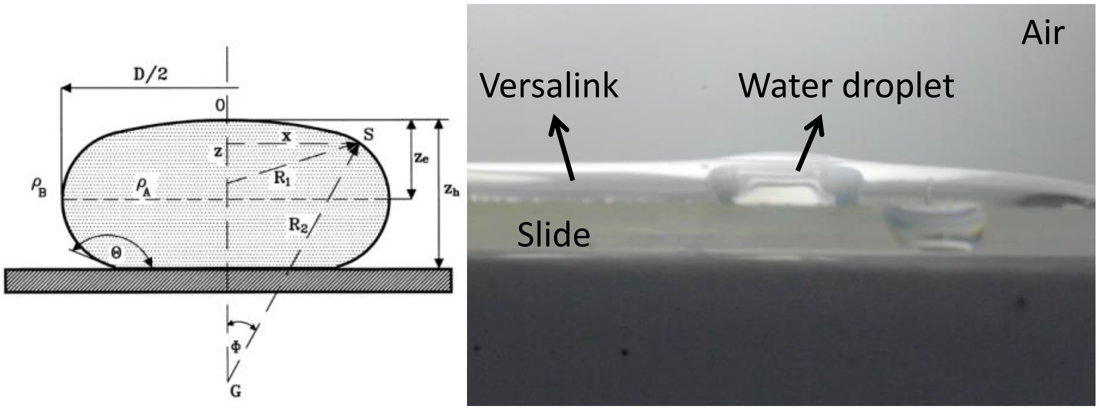

Figure 5.11: Measurement of the interfacial surface tension between water and Versalink P-1000 oligomeric diamine: Z_e =538μm, and γ=1.4 dyne/cm.

5.4.3. Rate of reaction of Versalink P-1000 and Isonate 143L

The rate of reaction of Versalink P-1000 oligomeric diamine and Isonate 143L was measured using a rotational viscometer shown in Figure 5.12. It is important to note that we considered the initial stage (45 min) of curing the Polyurea up until the mixture reaches high viscosity measurable by our setup.

We started the experiment procedure by degasing Versalink and Isonate for 1 hour. Then the degassed components were mixed for 1 minute using a magnetic stirrer under vacuum. A syringe was used to intake 0.4 gr of the mixture and then injected to the bottom of a vial. The viscometer's spindle was placed slowly into the vial to avoid trapping of air bubbles. The viscosity of the mixture was measured by recording the rotational speed and the applied torque (Figure 5.12). As the viscosity of the mixture increases in curing process, the rotational speed of the viscometer should be adjusted to keep the applied torque below the machine capacity. The rotational speed starts at 10RPM and is decreased to 5, 1, and 0.1 RPM as time passes. The viscosity of Polyurea mixture versus time is plotted in Logarithmic scale in Figure 5.13.

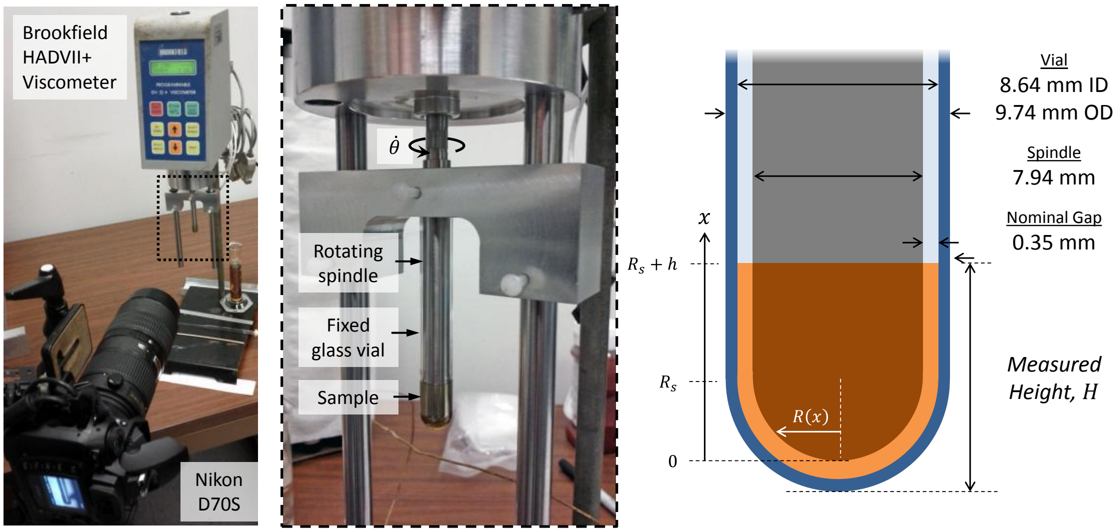

Figure 5.12: Rotational viscometer consisting of a rotating spindle, and a fixed glass vial. The rotational speed can be adjusted to measure a wide range of viscosity.

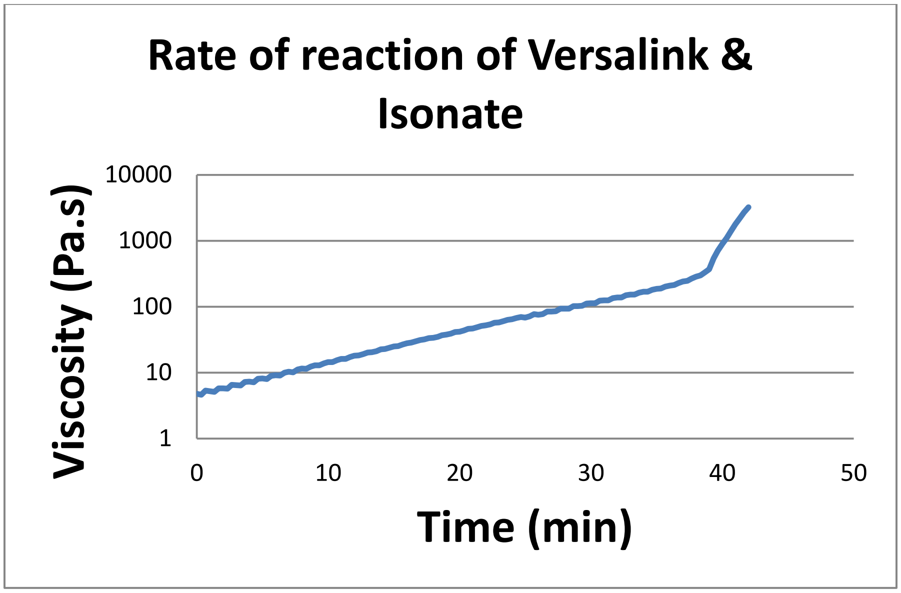

Figure 5.13: Rate of reaction of Versalink P-1000 oligomeric diamine and Isonate 143L in the initial curing process of Polyurea. The viscosity of the sample is measured versus time.

5.5. Summary

We studied the chemistry, synthesis, and characterization of polyurea based foam. We modified the chemistry reactions incorporated to synthesize pure polyurea, in order to create a porous structure with 100-250μm voids. The broken water droplets in the emulsion of water and Versalink react with isocyanate molecules to form CO_2 that acts as a blowing agent to create foam. The developed synthesis procedure has an inherent issue that leads to non-uniform distribution of voids, and therefore non-uniform mass density in the whole sample.

The samples were characterized for the developed microstructure as well as mechanical properties in macro scale. The porous microstructure was studied to find the void size due to each stoichiometry implemented in the material synthesis. Stress-strain behavior under uniaxial compression was studied for loading and unloading cycles. Storage and loss moduli were measured using DMA; and compared to the numerical predictions using micromechanics model for periodic distribution of voids. Additionally, a number of experiments were performed to study the critical parameters affecting the size of water droplets in the emulsion with Versalink, which has a direct impact in the size of pores in the foam.

5.6. References

[1] C.W. Hoge, D. McGurk, J.L. Thomas, A.L. Cox, C.C. Engel, and C.A. Castro, Mild Traumatic Brain Injury in U.S. Soldiers Returning from Iraq, The New England Journal of Medicine (2008).

[2] M. Grujicic, W.C. Bell, B. Pandurangan, T. He, Blast-wave impact-mitigation capability of polyurea when used as helmet suspension-pad material, Materials & Design, Volume 31, Issue 9, October 2010, Pages 4050-4065.

[3] B. Schimizze, S.F. Son, R. Goel, A.P. Vechart, L. Young, An experimental and numerical study of blast induced shock wave mitigation in sandwich structures, Applied Acoustics, Volume 74, Issue 1 (2013)

[4] D. Fragiadakis, R. Gamache, R.B. Bogoslovov, C.M. Roland, Segmental dynamics of polyurea: Effect of stoichiometry, Polymer, Volume 51, Issue 1 (2010).

[5] G.I. Taylor, The Formation of Emulsions in Definable Fields of Flow, Proc R. Soc. Lond A, Volume 146 (1934)